Doctoral Dissertation
Doctoral Program in Mechanical Engineering (35th Cycle)

Re-Use of the carbon fiber woven prepreg cut-outs: a multidisciplinary study

Process analysis, mechanical characterization, and numerical simulation of the chopped randomly oriented structure

By

Dario Fiumarella

******

Supervisor(s):
Prof. G. Belingardi
Prof. A. Scattina

Doctoral Examination Committee:
Prof. Andrea Bernasconi, Politecnico di Milano
Guan Gong, PhD, Research Institutes of Sweden (RISE)

Politecnico di Torino
2023

Declaration

I hereby declare that the contents and organization of this dissertation constitute my own original work and does not compromise in any way the rights of third parties, including those relating to the security of personal data.

Dario Fiumarella

2023

* This dissertation is presented in partial fulfillment of the requirements for **Ph.D. degree** in the Graduate School of Politecnico di Torino (ScuDo).

Abstract

Over the past few decades, there has been a continuous increase in the global demand for carbon fiber reinforced thermosetting polymers (TS-CFRP). This growth can be attributed to the expanding range of applications of TS-CFRP, which includes not only the primary markets of aerospace, aeronautics, and defense, but also the mass consumer goods industries, particularly in the sports, biomechanics, and automotive sectors. However, mass production involves the use of more standardized, cost-effective, and green production techniques to increase the efficiency of the manufacturing value chain and comply with the circular-economy concerns. Recyclability and reusability are the two main concepts to implement in order to properly apply the waste-management policies. The first imply the reclamation of the composite's main constituents from the end-of-life products; the second instead deals with the in-process cut-offs reuse, generated during the ply cutting operations. In this last case, the prepreg side streams are in an uncured condition, and thus can be used to produce new components without any intermediate reclamation stage.

This thesis work presents a multidisciplinary and applicative approach to accomplish the reuse strategies of the prepreg side streams coming from the ply cut operations. The manufacturing conditions, the structure quality, the mechanical characteristics, and the design requirements are correlated to validate and optimize the performance of the final part produced with the proposed technology. The prepreg cut-outs (called also chops, chips or strands) coming from the ply cut operations are used as raw charge to produce new components with the compression molding process. Each chop keeps the properties and the orthotropic structure of the original prepreg fabric from which it is cut, but the final component presents a discontinuous randomly oriented structure. As the charge is highly inhomogeneous in terms of local density and fiber orientation, the prediction of the final properties of the material results a tricky task. Consequently, a processability study was carried out, in order to analyze the material flow evolution during the compression stages. Furthermore, the mechanical properties of the final structure are strongly affected by the initial charge condition (i.e., the shape of the charge and the size of the chops). Accordingly, an extensive mechanical characterization was conducted to create a relationship between the performance output of the structure and the initial molding conditions. The results evidenced a high scatter as the material exhibits a variability of the local properties, that are mainly dictated by the presence of voids, rich matrix areas, interface regions between the chops and the local fiber rearrangement that occurs during the viscous flow stages of the manufacturing process.

Compared to the viscoelastic properties of a continuous fiber prepreg, pressing a charge composed of fabric cut-outs induces several phenomena, such as the sliding of a chop over another, the reorientation of the chops and the swirl rearrangement that cause the chops to fold up. These phenomena greatly influence the overall viscoelastic response of the charge, which is not only influenced by the rheological properties of the resin, but also by the interaction between the chops. Consequently, squeeze tests were performed for the characterization of the rheological properties of the material at different temperatures, and rheokinetc analytical models were fitted to predict the viscous behaviour of the material and build up numerical simulations.

The numerical model of the manufacturing process was built with the Moldex3D flow-based simulation software. As the initial charge presents randomly oriented chops, but each chops presents locally orthotropic oriented fibers, a Matlab code was written to generate the initial fiber orientation within the charge. The process results were then mapped with the Digimat multiscale software, and structural simulation were launched, and results compared with the experimental ones.

Finally, a case study was proposed: a Formula SAE accelerator pedal featuring ribs and narrow sections was manufactured to test the applicability of the proposed technology even to complex geometry. The pedal was then mechanically tested, and its production process simulated.

The performance of the produced components not only resulted to be comparable with the once of the most common low-density structural metals (i.e. Aluminum 6061), but can be also enhanced by properly tune the process conditions and the chop shape factors. The result of the investigation confirmed that the reuse of the in-line prepreg cut-outs is an efficient and cheap strategy to re-introduce in the value chain the side streams produced during the ply cutting operations.

Contents

List of Figures

List of Tables

1 Introduction

1.1 The composite market

The global demand of carbon fiber reinforced polymers (CFRP) has been continuously increasing in the last decades. Although up to the early 2000s the use of CFRPs was mainly directed towards low-volume production (aerospace, aeronautics, defense industry, high performance cars, turbines), starting from the last decade, world demand has grown from about 70 thousand tons per year in 2010 to more than 160 thousand tons per year in 2020, i.e an increase of more of the 120% [1,2]. This exponential increase can be attributed to the application of CFRP for not only for the aforementioned industries, but also in the mass consumer goods, especially in the sport, biomechanics, and automotive sectors. Additionally, the reduction in the cost of the carbon fiber due to research into more affordable precursors has also contributed to this increase. Considering this latter field, the CFRP application has been steadily growing not only in the high performance low-volume vehicles, but also in the mass-oriented market segments, driven by the demand for lightweight and high-performance materials. The aerospace and automotive industries, in particular, have embraced CFRPs due to their ability to replace metallic materials while maintaining or improving the performance of the end product. However, the use of CFRPs in mass production has posed some challenges. One of the main challenges is the high cost of production, which is due to the expensive nature of carbon fibers and the complex manufacturing processes involved. Another challenge is represented by the complex microstructures of CFRPs can make them difficult to predict and model, which can hinder the optimization of their performance.

Furthermore, mass production involves the use of more standardized, cost-effective and green production techniques to increase productivity and comply with the circular-economy concerns [3]. Indeed, the rapid increase in the demand will speed up also the CFRP wastes and side-streams both generated during the manufacturing stages and coming from the end-of-life components. The generation of these wastes poses challenges in terms of compliance with the circular-economy concerns. By just considering the CFRPs, it is foreseen that the wastes of this market could reach up 20ktons per year by 2025 [4]. Approximately the 40% of the wastes is generated during the manufacturing phase, and the 60% of these are side-streams coming from the woven trimmings and ply cut operations [5,6]. Indeed, the buy to fly ratio of a composite produced with CFRP prepreg can range from 1.2: 1 to 3.5: 1 [7]. In addition to the material waste, it is also important to consider the high energy consumption involved in the production of CFRP components. The production of a component with a CFRP prepreg requires the expenditure of about 40 MJ / kg, to which 285 MJ / kg to produce the fiber and 76 MJ / kg to produce the matrix [8]. It is thus crucial to reduce the reliance on landfills by implementing recycling techniques and finding ways to reuse the residues generated during the production process to decrease waste and give new value to the scrap materials.

1.2 Environmental impact

Recycling composite materials, including CFRPs, can be challenging because of their thermoset matrix composition, which forms a stable cross-linking structure after curing and becomes resistant to reshaping, heat processing, and decomposition under mild conditions. Indeed, the most common recycling routes are the mechanical recycling [9–11], the thermal recycling [12–14] and the chemical dissolution [15–17] of the matrix. However, it can be difficult to fully recover the full-length fibers or the matrix from these processes, due to the cross-linked nature of the thermosetting resins. To overcome these challenges and support the circular economy in the production and use of composite materials, it is important to minimize manufacturing side-streams and reuse any manufacturing cut-offs of prepreg, to reduce the overall amount of waste generated. Bianchi et al [18] conducted a life cycle assessment analysis (LCA) to evaluate the environmental impact of producing CFRP sample by using raw prepreg material coming from the production scraps. They evaluated three different scenarios: production by compression molding with virgin prepreg, compression molding with reused prepreg and autoclave pressing with virgin prepreg. They demonstrated that re-introducing the prepreg scraps within the production process has the best environmental performance, and there is a saving of 601MJ per kg of reused CFRP if compared to the more energy-intensive autoclave processing of virgin prepreg.

The energy demand of the production process should be also considered when assessing the global environmental impact of a process. Indeed, the forming processes often used for low production volumes (i.e. hand layup with autoclave pressing, VARI, RTM) turn out to be highly energy-intensive (10 to 19.2 MJ / kg). The production through closed mold forming (or compression molding) instead turns out to be more efficient from the energy point of view (3.5 MJ / kg), and it is for this reason that in recent years we are witnessing a wide diffusion of the production of structural components by means of technologies that involves the molding of the carbon fiber compounds, such as the Sheet Molding Compounds (SMC) [3,8,19]. For example, the exterior body panels of the 2020 Chevrolet Corvette, or the roof of the Toyota Yaris GR were made using SMCs [20,21]. The compression molding process, in particular, can be used to produce complex parts not feasible with continuous fiber composites, with a shorter cycle time and higher consolidation pressures suitable for high-load structural applications. Lamborghini's Forged Composite technology, which was used to manufacture the inner monocoque and suspension control arm of the Sesto Elemento vehicle, aimed for a 30% weight reduction and a reduction in cycle time compared to the traditional aluminum construction [22,23].

1.3 Reuse strategies

In this study, the compression molding process is used to reprocess the prepreg cut-outs generated during the ply cutting operations. This approach is motivated by the benefits of using the forming process for producing composite components, including the ability to create complex geometries and reduce production cycle time. The work presented here was conducted in collaboration with the Research Institutes of Sweden (RISE), the University of Camerino and the company HP Composites, which is a partner of the CIRCE project [24]. This project, funded by the LIFE program of the European Union, and aims to establish a circular economy model for uncured and cured CFRP materials. The focus of the project is on the reuse of uncured prepreg material rather than the recycling, which mainly reclaims the fibers of the composite. However, there can be some confusion surrounding the terms "recycle," "recover," and "reuse." In the author's opinion, the most appropriate term to describe the proposed methodology is "reuse". Indeed, the methodology aims to repurpose excess prepreg generated during the ply cutting operations, which is still in good condition with the resin in B-stage. This material has not been previously used and is not in an out-of-date condition, making "reuse" the most fitting term to describe the process.

Considering the recycling strategies, while some state-of-the-art methods, such as pyrolysis and solvolysis, can reclaim fibers, chemicals, monomers, and even polymers from the composite, it is still intricate to fully recover the polymer matrix in its original form and thus close the loop of the circular economy by allowing for the reuse of the resin. Additionally, matrix pyrolysis is an energy-intensive process that is not economically viable for quantities of material below 1000 t/year and has a not-negligible level of noxious gas emissions. Therefore, the project aims to create a circular economy model for the reuse of the prepreg CFRP side-streams.

The compression molding technology allows to produce parts with a good processability and mechanical performances, making the produced components suitable for structural applications. However, the properties of the final product depend heavily on the type of material used as the charge [25]. Using prepreg scraps (also called chops, strands, cut-offs) as the charge instead of SMCs requires a significant reevaluation of the production process parameters and an investigation of the mechanical performance of the final component. These types of structures, known as Randomly Oriented Strands (ROS) structures [26], or Prepreg Platelet Molded Composites (PPMC) structures [27,28], differ from traditional SMCs [29,30] because the initial structure is not composed of a single and compact bulk, but rather a collection of strands used as the initial charge.

The use of composite strands in the production of ROS components has been explored in several studies. De Souza et al. [31] used randomly oriented chops of Hexply prepreg to create a laminate via vacuum bag curing and found that, although there was a general trend of decreased mechanical properties respect to the virgin material, the final structure was still suitable for use in applications that do not requires high mechanical performance. Blanco et al. [32] developed a process for reusing aerospace prepreg scraps through compression molding, also resulting in products with properties suitable for components not subjected to high load conditions. Howell and Fukumoto [33] used compression molding of thermoplastic prepreg scraps to produce finished products with complex shapes and mechanical properties comparable to metal alloys. Jin et al. [34] used scrap cuts from UD thermoset prepreg to create composite panels through random chop deposition or a "mat-stacking lay-up" process, finding improved mechanical properties and surface finish, but higher void content compared to traditional layup. Wu et al. [35] examined the effect of chop size, resin state, and cure cycle on composite components produced through compression molding of recycled prepreg strands, finding that increasing pressing load and using shorter chops or low temperature cure cycles reduced void content and improved mechanical properties.

In [36,37] the authors investigated the effect of processing conditions on the quality of a complex ROS-T-shaped part. Results showed that low pressure and larger strand size required higher temperatures to fully consolidate a 25 mm deep rib cavity. However, the lowest void content was obtained for parts processed at lower temperatures. Initial strand placement within the mold was also found to significantly affect mechanical performance. A 40% reduction of the mechanical properties was observed at the component level due to merging flow fronts. Porosity was found to not have a detrimental effect on mechanical performance in the tested conditions.

Visweswaraiah et al [38] stated that there are several challenges that must be addressed in order to implement the use of ROS on a production scale, including difficulties in mechanical characterization (the strong dependence of material strength on strand size raises questions about the accuracy of strength measurements) and modelling, and the need for cost-effectiveness analysis. Additionally, those authors pointed out that there are issues with variability in manufacturing and dispersion methods, the suitability of traditional testing methods for ROS materials, and the need for more reliable and low-cost quality inspection methods. Finally, there are challenges in predicting and controlling warpage and residual stresses, as well as the effect of strand waviness on properties.

1.4 The problem to face

Although both the SMCs and the PPMCs present similarities in the production process and in the random nature of the fiber orientation, there are several differences that should be accounted. SMCs are commonly found in pre-mixed and pre-formed state material, while ROS architectures require additional time for strand cutting and placement in the mold. In terms of material properties, SMCs have more consistent and uniform properties due to the lack of strand-to-strand interface. ROS architectures, on the other hand, have variable properties due to the presence of chop-to-chop interfaces and the variability in the initial chop placement and orientation. ROS architectures also tend to have higher porosity and lower strength compared to SMCs.

To optimize the use of this material, it is necessary to consider factors such as the initial arrangement of the charge and its formability, the effect of chop size on properties, the influence of process properties on fracture mode, and the optimal thickness of prepreg for formability and mechanical properties. It is clear that the study and optimization of composite materials made up of prepreg scraps requires a comprehensive approach, starting with the properties of the base constituents (i.e. the chops) and how they respond to different processing conditions in order to define the performance of the final component. This requires a characterization process that begins with the study of the virgin material to understand its formability characteristics and how they impact the quality of the final product.

The aim of this thesis is to investigate the innovative aspects of the chopped structure created by reprocessing plain-structured (i.e. orthotropic) thermoset prepreg cut-offs generated during the ply-cut operations. The prepreg scraps coming from the same roll batch are cut into predetermined shapes and sizes to form the charge. The prepreg cuts are considered free of contamination and have not exceeded their expiration date, and the resin is in an uncured condition. These cuts are used as a charge to be placed in a mold for the production of components through the compression molding process.

The literature review shows that while there is a wide investigation on the process properties, formability, and mechanical properties of SMC and PPMC composites, there is a lack of research on the creation of discontinuous composites using plain-structured fiber chops and thermosetting resin. In fact, most of the published studies concern structures made of UD scraps and thermoplastic resins. This thesis aims to fill this gap in knowledge by:

1. *Exploring the forming capabilities of the charge made up of chops with bidirectional fibers and thermosetting matrix, and the extent in which they differ from traditional compounds;*

2. *Analyzing the mechanical properties of these composites and the extent in which they can be controlled;*

3. *Studying a strategy to predict the structure properties starting from the process conditions.*

Accordingly, a holistic approach has been undertaken to address the issue, starting with the characterization of the chopped raw material that makes up the charge to be pressed. Then, a systematic and thorough examination is conducted using appropriate experimental methodologies to study the mechanical properties and modes of fracture of this discontinuous material, paying particular attention to relate the material performance to the process parameters. Furthermore, a numerical model that predict the most important process features is proposed. This model is then used to infer the structural properties of the component through finite element simulations. The development of such models can greatly aid in the optimization of the processing parameters and the design of the component, as well as in the understanding of the influence of the process conditions on the final component properties.

1.5 Thesis organization

The formability of chopped carbon fiber composite differs from that of continuous fiber virgin material due to the pronounced flow-induced phenomena, such as fiber rearrangement. Moreover, during the pressing of the chopped charge, the viscoelastic response of the composite is not only affected by the resin properties but also by the inter-chop interaction, friction, and other mechanical effects that are less pronounced in the virgin material. Therefore, studying the overall rheological response of the chopped charge is essential to predict the evolution of the global viscous response as a function of the processing parameters. Accordingly, it is necessary to study the global rheological response of the chop charge in order to predict the evolution of the global viscous response as a function of the processing parameters. Viscosity plays a fundamental role in the quality of the final product, especially in reactive resin systems such as thermosets. In the Chapter 2, the rheological behavior of a chop charge is studied by performing the Squeeze test, which involves squeezing the charge between two open plates. In addition, the cure kinetics of the prepreg are studied in order to fit the Cross-Castro-Makosco analytical model, which allows for the prediction of the viscosity evolution of the material as a function of temperature, shear rate, and degree of material cure. Furthermore, the parameters of this model will be used to predict the rheological-kinetic behavior during the process simulation.

Once the flow behavior of the charge and its characteristics have been defined, the Chapter 3 investigates the compression molding process. The effect of the position and shape of the charge on the final microstructure of the manufactured product is studied. The porosity of the material is analyzed in relation to the processing parameters, and the most critical regions of the structure are identified, such as the interface regions between the chops and matrix-rich areas.

In the Chapter 4, the mechanical response of the material is studied through standard tensile and bending tests. The effect of different processing conditions, which induce the material to have a different structure, on the mechanical performance is analyzed. The most suitable prepreg system to be used is defined based on its density. In fact, specimens produced with prepreg of two different densities were tested and their mechanical response analyzed. The anisotropy of the material properties based on the initial placement of the charge in the mold, and the effect of the size and aspect ratio of the chops on the mechanical response were studied too. The evaluations were carried out with a critical approach, using characterization and analysis tools such as Digital Image Correlation or optical microscopy, for the evaluation of the local properties and the identification of the crack initiation and propagation modes.

The importance of the process simulation for chopped composite structures is discussed in the chapter 5, including a proposed methodology for simulating the process of a chopped composite charge using the commercial software Moldex3D. Since this software does not allow for the input of a chopped composite charge, a MATLAB code was written to generate the initial fiber orientation and the chopped structure. Rectangular plates with various initial charge conditions were simulated, reproducing the experimental results from the Chapter 3. The final fiber orientation in the plates was then mapped and linear field structural simulations were run using the software LS-Dyna and DIGIMAT in an integrated environment. The results of these simulations were compared to the experimental results to validate the proposed simulation methodology.

To demonstrate the practical application of this technology, a case study is presented in the last chapter, in which the concepts and the results obtained in the previous chapters are applied. The structure of an accelerator pedal, which features ribs, thickness variation and sharp edges, is fabricated to evaluate the forming ability of this kind of chopped charge. The pedal is then mechanically tested under the load case it is expected to encounter in its working condition, and a simulation of the production process is carried out to validate the methodology described in the chapter 5 on more complex geometries.

The research for this thesis was carried out as part of a collaborative effort between HP Composites, the Research Institutes of Sweden (RISE), the University of Camerino, and the Politecnico di Torino, where the author is affiliated. The author personally conducted the experimental tests utilizing the equipment and resources provided by the project partners. Furthermore, the author personally constructed the strategy for the process and structural simulations.

HP Composites supplied: a press; molds for pedal production; a testing machine for the pedal mechanical characterization.

The RISE provided access to: an INSTRON universal testing machine; a Digital Image Correlation system; a DSC machine; an optical microscope; a press.

The Politecnico di Torino made accessible: an INSTRON universal testing machine; a DIC digital image correlation system; a micro-CT scan (owned by the J-Tech interdepartmental center); software licenses and computers for the process and structural simulations.

2 Prepreg Characterization

The manufacturing of the thermosetting composite materials by means of the thermoforming process implies the use of continuous fiber prepreg sheets in B-Stage, i.e. whose resin is not yet in a crosslinked condition, in order to guarantee the proper formability and shape the charge within the mold. In the present study, the charge has a discontinuous long fiber structure, and it is made up of prepreg scraps (also called chops, platelet, cut-offs), cut from the continuous fiber fabric during the ply-cutting operations, finalized to get the final product shape.

In order to analyze and understand the flow properties and the formability characteristics of a chopped charge, all the chops were cut from the same prepreg sheet, rather than a mixture of chops from multiple prepreg systems. All the chops had the same dimension, of 20x20 mm. The properties of the virgin prepreg are listed in the table 1.

The curing cycle recommended by the prepreg manufacturer requires a pressure application for 90 minutes at a temperature of 135°C. Although the rheological properties of the considered epoxy resin have already been characterized by the manufacturer and are available in the datasheets, it must be pointed out that in the present study, the charge is made up of discontinuous chopped prepreg scraps.

The interactions between the chops during the compression molding process, including movements, rotations, and reorientation, can significantly impact the overall rheological response. These interactions, particularly during the viscous flow stages, present challenges for accurately predicting and designing the manufacturing process. The complexity of these reactive-viscous phenomena makes it difficult to rely solely on trial-and-error methods for efficient design and prediction.

To better understand the behavior of the chopped charge during the molding process and create predictive models, a characterization of its rheological and kinetic properties was conducted. This testing took place at the RISE facility in Piteå, Sweden.

Squeeze tests (see section 2.1) were carried out at different temperatures to evaluate the rheological properties evolution during the compression molding process. Furthermore, the cure kinetic was characterized by performing dynamic differential scanning calorimetry (DSC, see section 2.2). The experimental data from the squeeze and the DSC tests were then used to fit a phenomenological-analytical model that describes the viscosity evolution as a function of the curing degree, of the temperature and of the shear rate. This model is useful for the formability prediction of the raw chopped material, as well as for the set-up of a material card for the numerical process simulations.

Prepreg Properties	
Cured Resin Density (g/cm^3)	1.2
Carbon Fiber Density (g/cm^3)	1.8
Resin Gel Time @110°C (min)	20 to 25
Prepreg Areal Density (g/m^2)	204
Prepreg Average Thickness (mm)	0.27
Prepreg Fiber Volume Fraction (%)	58

Table 1. Considered Prepreg Properties – carbon fiber fabric and epoxy matrix

2.1 Resin rheology

Polymers are commonly divided into two macro categories: thermoplastic polymers and thermosetting polymers. The formers are composed of linear or lightly branched polymer chains, which create weak intermolecular bonds (such as hydrogen bonds or van der Waals force bonds). When subjected to high temperatures, the chains can move and slide one over the other. Due to this freedom of movement between the chains, the thermoplastic polymers soften at high temperature, and can be remelted or re-formed [39,40].

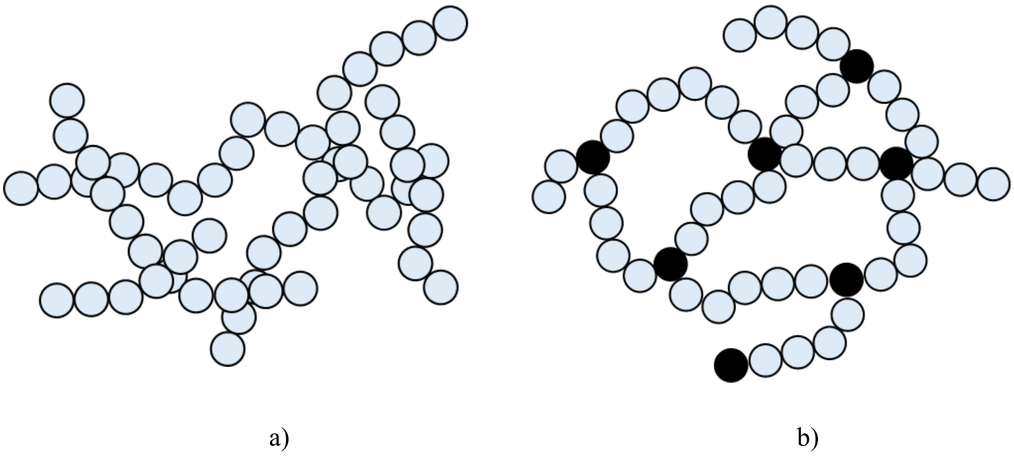

a) b)

Figure 2.1. Polymers chain scheme: a) thermoplastic polymer; b) thermosetting polymer.

In contrast, thermosetting polymers, such as the epoxy resins, are composed of cross-linked chains. Crosslinks are strong bonds (ionic or covalent bonds) that hinder the mobility between the polymer chains. These strong bonds between the chains lead the thermosetting polymers to behave in a fragile and brittle way, and they cannot be broken when high temperatures are applied.

The state of cure of a thermosetting resin indicates the degree of progress of the crosslinking reaction. This is usually divided into two phases: 1) formation and growth of the polymeric chains and 2) cross-link generation. A reaction catalyst (also called hardener) is usually added to the resin to let the polymerization and cross-linking reaction start. During the exothermic cross-linking reaction, the viscosity of the resin changes as a function of the curing state. The viscosity increases due to the cross-links bond formation, that hold the polymer chain avoiding them to freely move [41–43]. However, the evolution of the viscosity of a thermosetting polymer is a complex process, which depends not only on the curing degree, but also on factors such as the temperature, the applied pressure, the reaction time, and the deformation rate of the fluid subjected to a stress. Accordingly, the rheological behaviour of the reactive systems represents an important issue in relation to the processing conditions and needs to be clearly understood to predict and optimize the manufacturing outcome [44].

2.1.1 Viscosity Models

The viscosity of the reactive polymers in the B-stage depends on several chemical-physical parameters and on the interaction between them. The main classification of the polymer behaviour is based on the viscosity evolution as a function of the applied pressure:

1) Shear thickening fluid: the viscosity increases as a function of the applied load;
2) Shear thinning fluid: the viscosity decreases as a function of the applied load;
3) Newtonian fluid: the viscosity does not change as a function of the applied load.

A Newtonian fluid is characterized by a linear relationship between shear stress and fluid velocity. When placed between two horizontal parallel walls, with one moving and one stationary, the velocity profile of a Newtonian fluid exhibits a linear trend. The velocity at the moving wall is equal to the wall velocity, while the velocity at the stationary wall is zero, indicating the absence of slippage. Accordingly, the shear rate is defined as follow:

$$\dot{\gamma} = \frac{V}{H} \tag{2.1}$$

where V is the fluid velocity, H is the thickness of the fluid layer and $\dot{\gamma}$ is the shear rate. The shear stress is defined as the shear force divided by the surface on which it is applied:

$$\tau = \frac{F}{A} \tag{2.2}$$

where F is the applied force, A the considered area and τ the shear stress. Accordingly, the viscosity is defined as the ratio between the shear stress and the shear rate:

$$\eta = \frac{\tau}{\dot{\gamma}} \tag{2.3}$$

For a Newtonian fluid, the viscosity is constant and independent on temperature and shear-rate [45]. As the viscosity of a resin depends on several chemical-physical factors, phenomenological-analytical models are commonly used to describe the viscosity evolution [42].

Power-law models have been extensively and successfully used for the viscosity prediction of thermoplastic polymers [8, 9]. These models are based on the power-law equation, which states that the shear stress is proportional to the power of the shear rate, and is usually expressed as follow:

$$\eta = \eta_0(T)\dot{\gamma}^{n-1} \tag{2.4}$$

with

$$\eta_0(T) = Be^{\frac{T_b}{T}} \tag{2.5}$$

where η_0 is the zero-shear viscosity (i.e. the viscosity in quasi-static condition), n is the power law index and $\dot{\gamma}$ is the shear rate, B is the consistency index, T is the actual polymer temperature and T_b is the temperature sensibility parameter. This model allows to consider viscosity non-linearities and the temperature-dependency of the viscosity. The power law model well describes the behaviour of the thermoplastic polymers, where the viscosity in the shear thinning region decreases as a function of the temperature, as the polymer chains become more linear, can easily move and slide one over the other. However, for reactive systems such as thermosetting polymers, the degree of cross-linking influences the viscosity, and the effects are two-fold. In a first stage the viscosity decreases due to the increased thermal effects; however, as soon as the conversion degree starts to increase, the cross-linked network hides the chain movements, and the viscosity eventually increases. Accordingly, the viscosity curve of the thermoset polymers presents a parabolic shape, and it depends not only on the temperature and on the shear rate, but also on the degree of cure. By combining the effects of the cure, the shear rate and of the temperature, a complete descriptive model for the viscosity evolution can be built. These are called reactive viscosity models and are used to describe the rheological behavior of materials that undergo chemical reactions during processing, such as thermosetting polymers. These models take into account the effect of the chemical reaction on the viscosity of the material, as the reaction progresses and the material cures or crosslinks. One of the most used, in the literature but also in the commercial codes such as Moldex3D, is the Cross-Castro-Macosko model for reactive polymers [48,49]

$$\eta(T,\dot{\gamma},\alpha) = \frac{\eta_0(T)}{1+\left(\frac{\eta_0(T)\cdot\dot{\gamma}}{\tau^*}\right)^{n-1}}\left(\frac{\alpha_g}{\alpha_g-\alpha}\right)^{(c_1+c_2\alpha)} \tag{2.6}$$

where η is the viscosity at a certain temperature, shear rate and conversion degree α, $\eta_0(T)$ is the zero-shear viscosity (see eq. 2.5), n is the power law index, α_g is the cross-linking degree at the gel point, c_1 & c_2 are the exponential constants that must be calibrated by the experimental results, and τ^* is the shear stress at transition from Newtonian to the non-Newtonian region. As the model in the equation 2.6 depends also on the degree of cure, the fitting process requires to implement other analytical models (such as the Sourour and Kamal equation, see section 2.2.1) to account for the curing degree influence on the viscosity evolution, to optimize the model parameters and build an effective and reliable prediction. The rheological-kinetic characterization and the model fitting process will be explained in detail in the next sections.

2.1.2 Viscosity characterization methodologies

The effect of the shear rate on the viscosity of the thermoset resins is usually measured on uncatalyzed resins, as the effect of the shear rate is most significant in the early stages of the manufacturing process. The rheometers are the most diffused instrument to trace the viscosity evolution of a polymer as a function of the shear rate. The rotary rheometers have been widely diffused in the past years and are made up of two plates that applies shear stresses to a viscous fluid. In the oscillating disk rheometer, an oscillating biconical rotor generates inside a cavity the shear stress necessary to test the fluid under examination. The cavity can be properly heated at constant temperature or using different heating rates to evaluate the viscosity evolution at different temperatures [50].

However, the application of the conventional rotary rheometers for the rheological characterization of the fiber reinforced composites (such as the Sheet Molding Compound) has been widely criticized as this methodology does not capture the typical biaxial extension usually induced by the compression molding process [47,51,52]. Furthermore, the maximum shear rate explored by the rotary rheometers lies around 10 s^{-1} [53], while the common shear rates encountered in the manufacturing process windows can range from 1 s^{-1} to 10,000 s^{-1} [44].

An alternative to the rotary rheometers for the evaluation of the fiber reinforced polymers viscosity is represented by the squeeze rheometers. This test induces a squeeze flow on the sample polymer that is loaded in a normal direction (Figure 2.2). The test is performed by placing a disc-shape of molten material between two flat axisymmetric plates. One of the two plates compresses the charge at constant force or constant motion rate. As the distance h (gap) between the two plates decreases, the charge is biaxially extruded, and the value of the force normal to the charge is acquired. For the constant area squeeze flow, the molten material has the same radius of the loading plates. Accordingly, during all the compression process, the loaded area is kept constant even if some material is extruded outside.

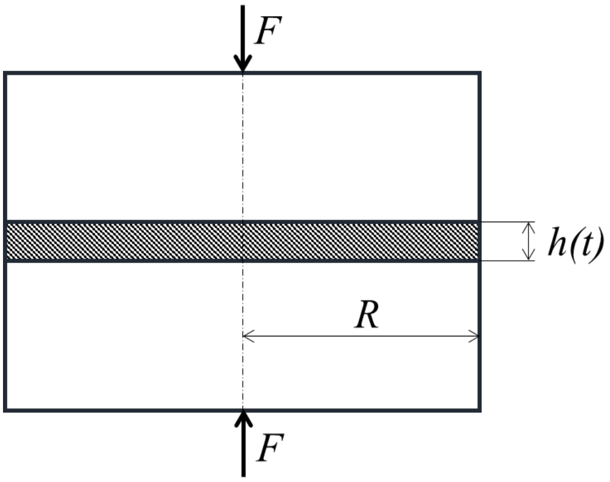

Figure 2.2. Constant Area Squeeze test scheme.

The global material viscosity as a function of the shear rate, can be estimated starting from the information of the applied normal force and of the gap h. Many authors successfully implemented the Stefan equation [53–58] which relates the material viscosity to the applied force and to the gap:

$$\eta = \frac{2Fh^3}{3\pi R^4 \dot{h}} \tag{2.7}$$

where η is the material viscosity, F is the normal force applied to the material, R is the plate radius, $\dot{h}$ is the plate closing velocity.

The shear rate $\dot{\gamma}$, taking into account the parabolic velocity profile that is generated assuming a non-slip condition at the wall interface, is given by:

$$\dot{\gamma} = \frac{3\dot{h}R}{h^2} \tag{2.8}$$

The estimation of the viscosity by means of the Stefan’s equations is however limited by the following assumptions:

1) The tested material is considered incompressible;
2) The flow is symmetric;
3) No slip at the wall interface;
4) Temperature uniformity within the charge;
5) The material behaves as a Newtonian fluid.

The assumption of Newtonian Fluid could lead to great result distortion especially if the fluid presents a power-law behaviour. However, at very low shear rate, the material behaviour can be approximated to a Newtonian fluid and the equation 2.7 can still be applied for the evaluation of the squeeze viscosity.

Although these approximations, the squeeze flow approach presents several advantages for the characterization of the rheological behaviors of the SMC and long fiber composites. First, the squeeze test allows to explore the behaviour of the viscosity in a wide shear rate range, and it is representative of the material flow during the manufacturing process such as the compression molding. Furthermore, the geometry and the set-up of the test is relatively simple and can be carried out by using common universal testing machines. In addition, the squeeze test allows to identify the main phenomena that influence the global viscosity response of the chopped charge, such as the chop interaction and rearrangement during the viscous flow stages.

2.1.3 Squeeze Test

The squeeze tests on the chopped material were executed in the Laboratory of the Research Institutes of Sweden (RISE) in the Piteå facility, using an Instron Servo-hydraulic universal testing machine equipped with a 100kN load cell. The fixture set-up is illustrated in the Figure 2.3. Two steel tools with a circular cross section of 100 mm of diameter and free edges were used to press the charge. The tools temperature was controlled by a resistance heating system connected to a thermal control unit. During the tests, the temperature was checked by two thermocouples placed on the side of the tool. As the thermocouples were checking the temperature just on the side of the tool before each test the temperature was also measured on the tool planar surface with an external temperature sensor. The tools were connected to the water cooling loops in order to preserve the load cell from the high temperature.

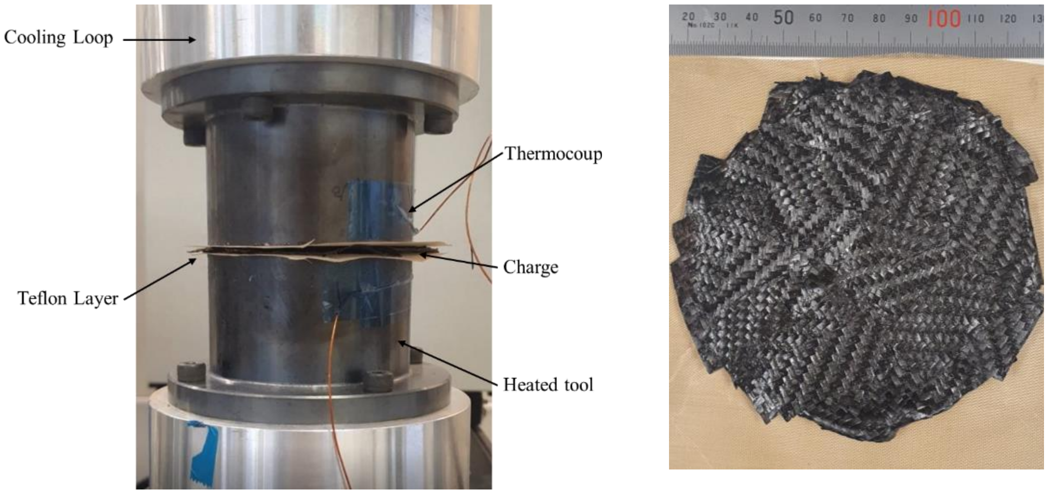

a

b

Figure 2.3. Squeeze Test set-up. a) detail of the fixture. The steel tools were anchored to the upper and lower steel fixture in which cooling loops are present. On the upper and lower tool face, a Teflon layer was placed. The thermocouples were placed on the upper and lower tool side surface; b) initial charge sample geometry.

On both the tool faces, a Teflon layer was inserted to avoid the material to get in contact and stick directly on the metal surfaces.

The charge was composed by chops cut with a size of 20x20mm. The samples had a circular shape with a diameter equal to the diameter of the testing tool (100mm), and the mass of the samples for all the test was approximately equal to 29 grams.

The Squeeze test was widely used for the rheological characterization of the SMC material. Although the SMC contains a certain quantity of voids, the thickness of the B-Stage uncompressed material can be considered homogeneous and free of macro discontinuities. Contrary to what occurs with SMC materials, the chopped charge initially contains a large amount of air between the chops, as the chops are not compacted, and exhibits significant thickness inhomogeneity due to the uneven overlap of the stacked chops. Accordingly, the specimen preparation required high attention to evenly distribute the chops and make the charge as homogeneous as possible in terms of thickness. Around 5 layers of chops were stacked across the thickness. A rubber hammer was used to uniformly distribute the material and let the air between the chops escape. An effort was made to achieve a uniform sample thickness of about 2.5 mm. However, it was impossible to obtain a perfectly constant sample thickness, and the local thickness inhomogeneity was the only parameter not well-controlled.

The tests were controlled by the WaveMatrix software provided by Bluehill. The test steps were set as follow (Figure 2.4):

- Step 1: crosshead moves at 10mm/s up to 1kN of load;
- Step 2: crosshead holds the position for a time *t*;
- Step 3: crosshead moves at 1 mm/s up to a gap between the plates of 0.1mm with a maximum limit load of 95kN.

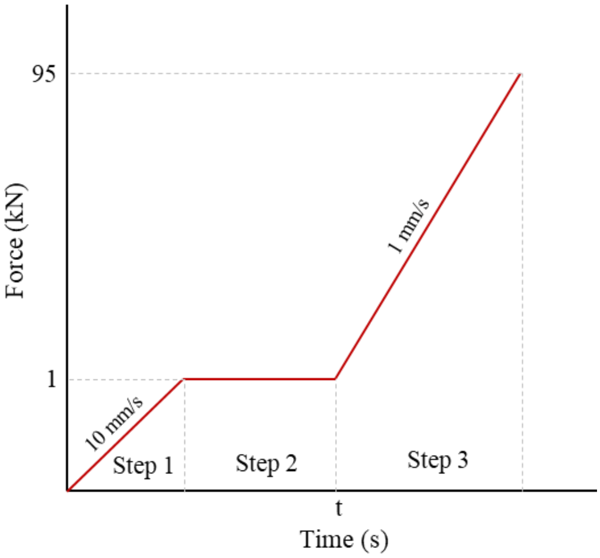

Figure 2.4. Squeeze test steps graph. Note that the Y axis is not in scale, but it gives a qualitative indication of the force stages.

The first step allows to further compact the sample, uniform the thickness, and let the trapped air escape. The 1kN force level was set after several trial-and-error attempts, and it was high enough to get a good compaction of the charge but low enough to avoid the resin and the chop to start moving and flowing. After the compaction stage (step 1), the holding stage (step 2) had the purpose to guarantee a homogeneous temperature distribution across the sample thickness and thus stick with the assumption of uniform distribution made in the section 2.1.2. The holding time was adjusted based on the testing temperature. For lower temperatures (50°C), a longer holding time was set to ensure uniform temperature distribution across the charge thickness. For higher temperatures (145°C), the holding time was reduced to prevent the resin conversion reaction to occur. The holding times were determined through trial and error. For instance, some trials were conducted at 145°C with a holding time of 120 seconds, but this resulted in a too high initial pressing force value and low chop flow. This indicated that the chop layers in contact with the mold had already started to cure and therefore the holding time had to be reduced. The Table 2 summarizes the temperature and holding times for the step 2 of the test.

Temperature [°C]	**Holding Time [s]**
50	120
80	90
100	50
120	30
145	15

Table 2: Test temperatures and holding times for stage 2

The holding times at each temperature were chosen after a trial-and-error process. Indeed, a holding time of 30 s with a temperature 145°C led the boundary layer chops (i.e. the layer that directly get in contact with the tool walls) to rapidly cure even before the compression started.

As stated before, during the third stage (step 3) the testing machines applied the required force to let the material squeeze, up to a gap between the tools of 0.1mm. In addition, a limit on the maximum force to 95kN was set to preserve the load cell and the fixture. The compression speed was set equal to 1mm/min in accordance with the compression velocity of the real molding process. The force was read with an acquisition frequency of 100Hz.

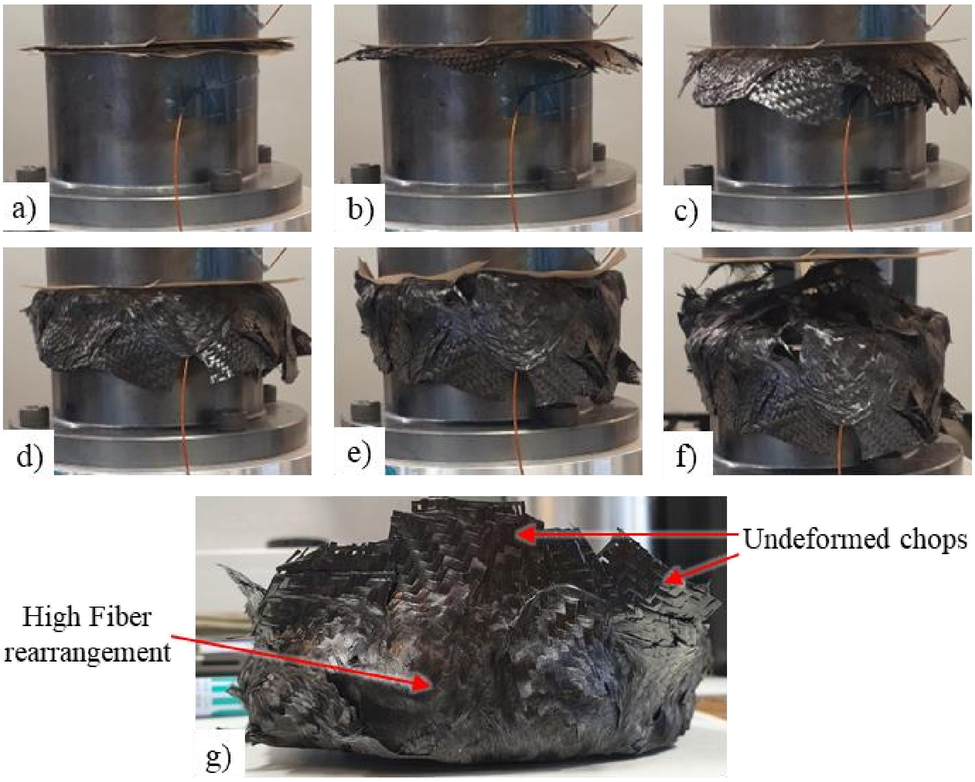

Figure 2.5. Squeeze tests results: a-f) step 3 of the squeeze test at different compression stages; g) sample after cure.

The Figure 2.5 shows the qualitative results of the squeeze flow test at different compression gaps. It is possible to notice that for the first steps (b-c) the chops seem to just squeeze out from the tool. They are rigidly transported outside of the edge of the tool, and they do not undergo to deformations or warpage. As the compression gap decreases (d-e), the outermost chops that compose the boundary layer deforms and tends to rearrange in the squeeze flow direction. The chops that are between the two boundary layers instead tend to remain undeformed and are rigidly transported. This behaviour is due to different reasons. The boundary layer chops stick with the Teflon and high shear is generated. The friction between the chop in the boundary layer and the Teflon is higher respect to the friction between the chops. Accordingly, the chops of the boundary layer push on the lower chops, but since the contact between the two chops is dominated by the low viscosity of the resin, low shear force are generated and the chop in the central layer are just rigidly squeezed out.

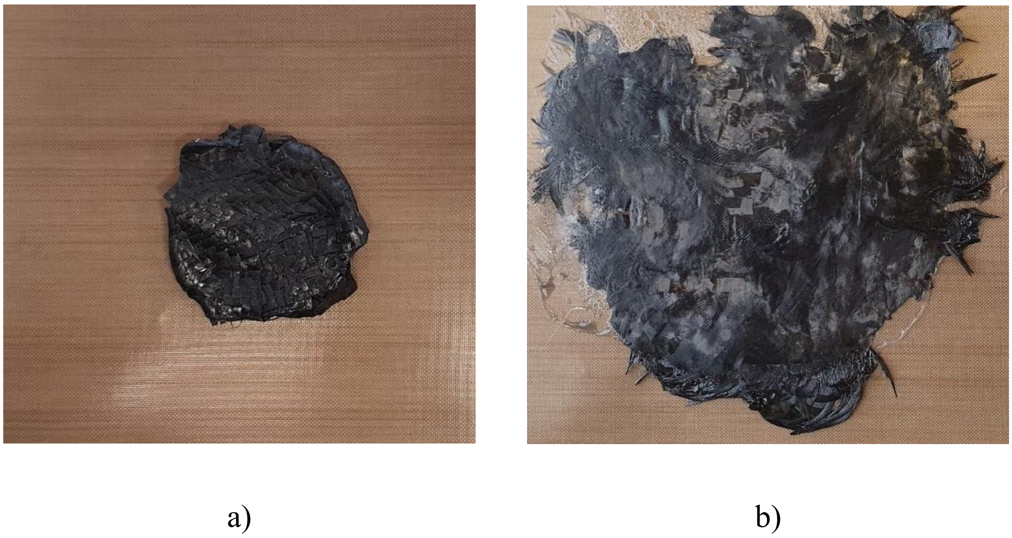

a) b)

Figure 2.6. Constant volume squeeze test: a) tested sample before compression; b) tested sample after compression.

In order to qualitatively assess the moving path of the flow front, evaluate its shape, and determine if it advances symmetrically or is influenced by the strong anisotropy of the material, the constant volume squeeze tests were also performed. The Figure 2.6 shows the test results of a constant volume squeeze test carried out to delved deeper the flow behaviour of the chopped material. In the constant volume squeeze test, the radius of the tool plate is much larger than the one of the samples. Furthermore, during the test the sample radius increases [53]. In this case, the charge did not cover the whole area of the tool, but just a part small enough to avoid the material to squeeze out from the edge of the tool at the end of the compression. The weight of the charge was 2.7 grams, the diameter of the sample was around 45mm, small enough to avoid the material to squeeze out from the tool’s edge. The tool radius was again 100mm. It is possible to notice in the Figure 2.6 that the flow front after the test does not have a regular circular shape, but the flow is inhomogeneous in all the directions, even if the fibers tend to radially rearrange. A constant volume squeeze test was performed on an SMC compound too, in order to compare the flow front advancement with the chopped charge. In this case, the SMC charge showed a more regular and symmetric advancement of the melt material, with just small discontinuities in the flow front circumference due to the initial random fiber orientation. The high flow discontinuity evidenced in the chopped material is mainly due to a non-uniform pressure distribution over the samples surfaces due the initial thickness unevenness of the samples. This unevenness is characterized by a crest and valleys profile of the sample. Accordingly, as the gap decreases, the tool gets in contact with the crests, leading this portion of material to start flowing before a uniform contact of the tool with the sample.

The Figure 2.7 shows the results of the squeeze tests at different temperatures in terms of force-displacement plot. It is worth to notice that the real testing temperatures measured by the thermocouples were not exactly equal to the nominal testing temperatures proposed in the Table 2 because of the uncertainty of the temperature control system and of the high thermal inertia of the two tools. However, the gap between the target and the testing temperature is limited to few degrees of difference, and thus it lies in an acceptable range. The force and the displacement values were the first output obtained directly from the testing machine load cell and displacement transducer.

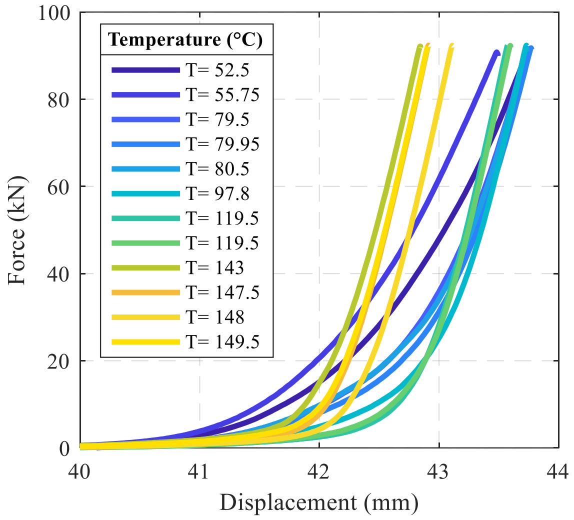

Figure 2.7. Force-Displacement plot of the squeeze test at different temperatures.

All the curves represent the force profile of the step 3. Indeed, they start from a force value of 1kN, that is the force level at which the crosshead presses the sample during the holding-heating phase. During the first millimeters of displacement (stage 1) the material compacts, starts flowing in the radial direction, and the force value remains almost unchanged. A further increase of the displacement leads the force to rapidly increase, due to the compaction of the charge and the development of high shear forces. This second stage (stage 2) is strongly dependent on the testing temperature. Between 50°C and 80°C all the curves present almost the same slope, even if as the temperature increases up to 80°C the maximum displacements (i.e. the maximum compaction level) tends to increase. This is because at 80°C the viscosity of the resin is lower due to the higher temperature; therefore the material can easily flow and less shear forces are generated. An increase in the test temperature between 100 and 110°C leads the stage 1 to last for greater displacement, even if the change of the slope between the stage 1 and the stage 2 is sharper. In the stage 2 the curve presents a higher slope, and the final displacement at 95kN of force are lower than the test executed at 80°C. The test executed at temperatures above 140°C presents instead lower compaction levels (the maximum displacements of the stage 1 is around 42 mm) and even lower maximum squeeze displacement at maximum force in the stage 2 (around 43 mm). The switch between the stage 1 and the stage 2 is more sudden and sharper and the slope of the stage 2 is the steepest. At temperature above 120°C the cross-linking reaction already begins, the conversion degree increases, and the viscosity of the resin increases as well, leading the shear force between the chops to be higher.

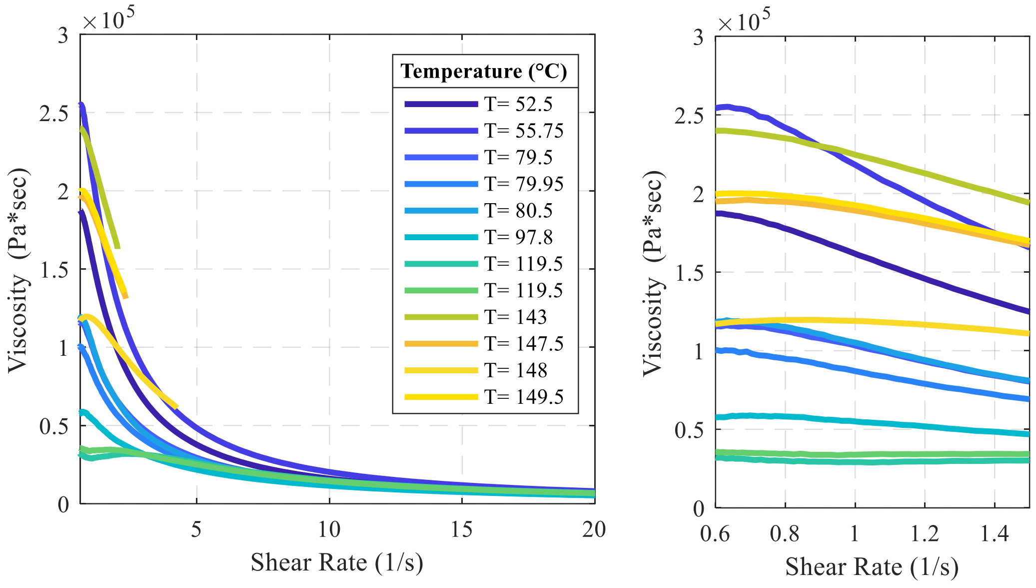

a) b)

Figure 2.8. Viscosity-Shear rate plot of the squeeze test at different temperatures.

The Figure 2.8 shows the trend of the sample squeeze viscosity against the shear rate. The viscosity and the shear rate values were obtained by means of the Stefan equations (equations 2.7 and 2.8). It should be noted that although the fluid may not strictly obey the definition of a Newtonian fluid, approximating it as such is useful for the purposes of this study, especially when considering very low shear rates. The assumption of Newtonian behavior is a common simplifying hypothesis in rheological tests and allows for easy interpretation of the results.

From the graph in the Figure 2.8a, it is possible to state that the sample behaves as a shear thinning fluid, as the viscosity decreases as a function of the shear rate. Looking at the region at very low shear rate (Figure 2.8b), the behaviour of the fluid can be approximated to a Newtonian fluid as the viscosity does not present high variations. However, it should be noted that for some tests at lower temperatures, the variation in viscosity at very low shear rates may be greater than 5% of the starting viscosity. Despite this small inaccuracy, approximating the fluid as a Newtonian fluid is still useful for the purposes of this study.

It is possible to notice that as the test temperature increases, the viscosity decreases up to 120°C. By further increasing the temperature, the viscosity starts to increase again due to the cross-linking reaction that forms rigid bonds between the polymer chains. At higher shear rate the curves at all the temperatures get closer and the viscosity tends to the zero value, except for the test executed above a temperature of 140°C. For these samples, the curves stop at shear rate lower than 5 s^{-1}. This is because the force gets the limit value (90kN) at higher gap, due to the initiation of the cure reaction that leads the viscosity to rapidly increase.

2.2 Cure kinetics

2.2.1 Theory background

The curing kinetic of a thermosetting resin is a process in which the polymer chains forms cross-link bonding under the action of temperature and of a curing agent [59]. This process requires time, and the required time depends on the temperature profile applied to the resin. During this time, the resin passes through the gelation and the vitrification stages. The cure kinetics tests allow to study the thermally induced reactions of a polymer when subjected to different temperature profiles and exposed for different times to a certain temperature. The most diffused test to characterize the cure kinetics of a polymer is the Differential Scanning Calorimetry (DSC). The DSC machine consists of one chamber where the sample is placed, and a reference control chamber usually filled with an inert medium. A heat flux is provided to increase the temperature of the sample of a certain ΔT while keeping the two chambers at the same temperature by a feedback mechanism. The difference of the heat flux between the two chambers is measured as a function of the sample temperature [60,61].

The heat flux, the temperature and the time are the output parameters of the DSC test. The DSC detects any change that alters the heat flow in the sample chamber, and these changes are due to the heat generated during the curing reaction. The curing degree can be defined as the ratio between the heat change generated at a certain time of the reaction (residual heat, H_{res}) and the total enthalpy of the reaction H_{tot}. Accordingly, the curing degree α(t) is defined as [62,63]:

$$\alpha(t) = \frac{H_{res}}{H_{tot}} = \frac{H_{res}(t)}{\int_0^{t_f} \left(\frac{dQ}{dt}\right) dt} \tag{2.9}$$

where t_f is the time at which the reaction is considered concluded (i.e. the point at which there is no more a variation in the heat flux), and $\left(\frac{dQ}{dt}\right)$ is the instantaneous rate of heat generated.

Several authors proposed isothermal and dynamic DSC scans to generate experimental data to fit phenomenological-analytical curing kinetic models [62,64–68]. In dynamic DSC test, a heating ramp is imposed, and in this case the samples are subjected to a superposition of chemical-structural modifications and temperature evolution. The cross-linking reaction of the epoxy resins involves the transformation of low molecular weight liquids to an amorphous network by means of an exothermic chemical reaction. These reactions are dominated by two contributions: the catalytic and the auto-catalytic reactions. The extent of these two contributions varies according to the temperature. The model most widely used for describing the cure kinetics of the epoxy resin systems is the Kamal-Sourour equation [69,70]:

$$\begin{gathered} \frac{d\alpha}{dt} = (K_1 + K_2\alpha^m)(1-\alpha)^n \\ K_1 = Ae^{\left(\frac{-E_a}{RT}\right)} \ ; \ K_2 = Be^{\left(\frac{-E_b}{RT}\right)} \end{gathered} \tag{2.10}$$

where α is the degree of cure, $\frac{d\alpha}{dt}$ is the conversion rate, m and n are the reaction orders, K_1 and K_2 are the temperature-dependent Arrhenius constants, E_a and E_b are the activation energies for the catalytic and auto-catalytic reactions, R is the universal gas law constant and T is the actual cure temperature.

2.2.2 Experimental DSC Tests

The DSC test were executed with a Mettler Toledo DSC 3 Star System under isothermal and non-isothermal conditions. The mass of all the samples was about

30mg and a closed aluminum pan was used to contain the material. The samples were cut directly from the prepreg fabric by means of a circular cutter.

The results of the dynamic DSC tests are shown in Figure 2.9. Five temperature ramps were adopted for the different tests, specifically heating ramps equal to 1, 2, 2.5, 5 and 10 Celsius degree per minute. The heat flux is expressed per unit of reactive mass. Indeed, the total heat flux was divided by the resin mass present in the prepreg sample, considering a resin content equal to the 46% of the prepreg mass. From the graph in Figure 2.9a, it is possible to notice that increasing the temperature ramp the activation of the reaction moves towards higher temperature, as well as the peak of the heat flux. The plot in Figure 2.9b shows the conversion degree evaluated with the equation 2.9 as a function of the temperature.

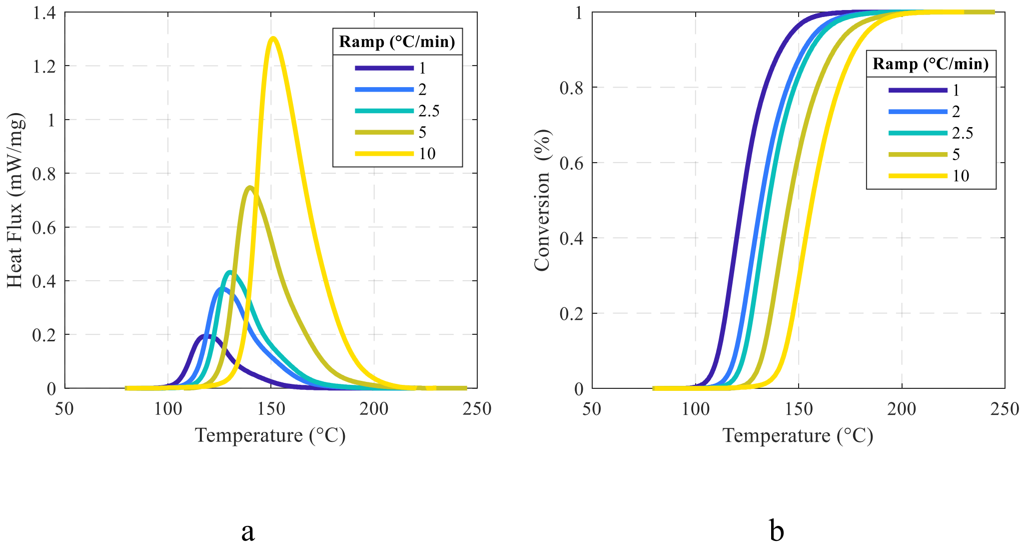

Figure 2.9. Dynamic DSC test results: a) Heat Flux vs Temperature; b) Conversion degree vs Temperature.

Also from this graph, as expected, it is possible to appreciate that the conversion initiation temperature increases as a function of the temperature ramp. Figure 2.10 shows the isothermal DSC tests. In this case, three temperatures were tested, namely 130, 140 and 150°C.

The software NETZSCH Kinetics NEO was used to fit the Kamal-Sourour equation and optimize the model parameters. The fitted parameters are reported in the Table 3, and the fitted curves are illustrated in the Figure 2.11. From this figure it is appreciable that the model and the fitted parameters are optimally capturing the experimental curves, even if there is a small shift for the curves at low heating ramp (1 deg/min). However, the error decreases as soon as the ramp increases.

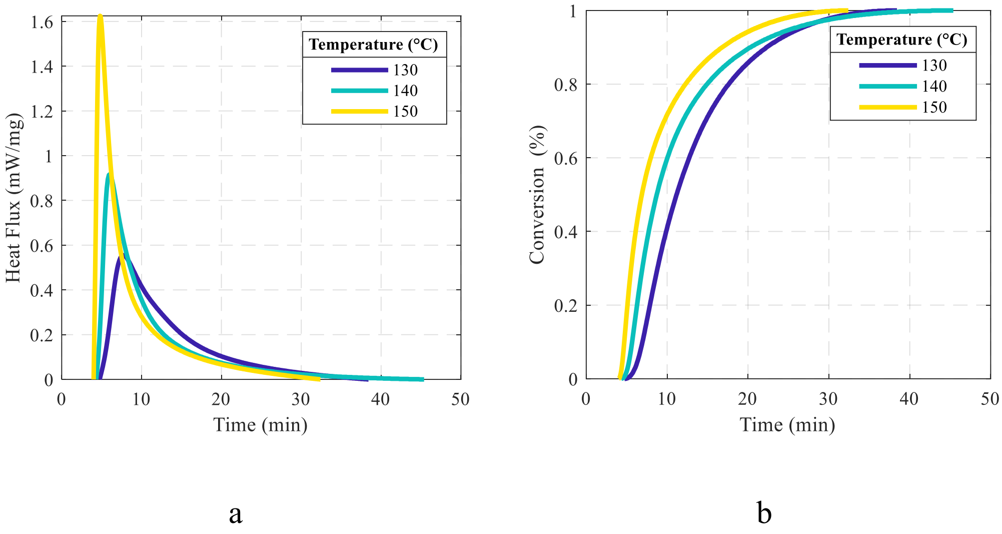

Figure 2.10. Isotherm DSC Test results: a) Heat Flux vs Temperature; b) Conversion degree vs Temperature.

E_a (kJ/mol)	E_b (kJ/mol)	Log(A) (s^{-1})	Log(B) (s^{-1})	n	m
112.2	96.1	10.29	0.024	2.081	0.664

Table 3. Kamal-Sourour model fitted parameters

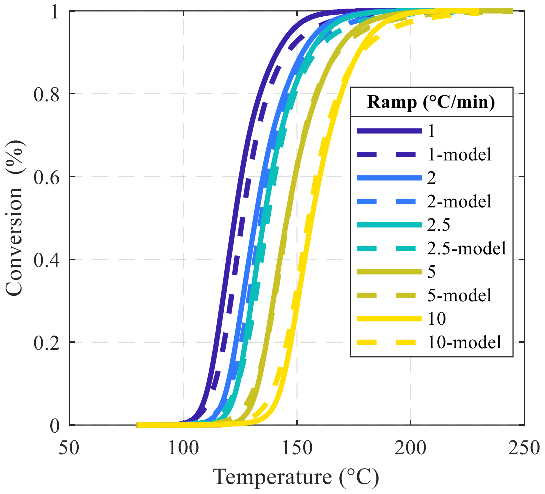

Figure 2.11. Conversion degree as a function of the temperature and fitted model.

2.2.3 Cross-Castro-Makosco fitting process

Once obtained the viscosity data and the curing kinetics model, the Cross-Castro Makosco model parameters were obtained through an optimization process. As stated in the previous sections, the Stephan's equations for the evaluation of the squeeze viscosity holds if the considered material behaves as a Newtonian Fluid. The assumption of a Newtonian fluid behavior can be made at very low shear rates with some degree of approximation, as discussed in the previous sections (Figure 2.8b). The Figure 2.12 shows the viscosities evolution at shear rate that tends to zero. It is possible to notice that as the temperature increases in the range 50-120°C the viscosity drops down, but above 130°C it rapidly increases due to the rapid onset of the cross-link reactions. Accordingly, during the manufacturing of the components, the processability window should be kept between 100 and 125°C during the charge flow stage, in order to avoid flow obstruction of the melt and residual stresses generation.

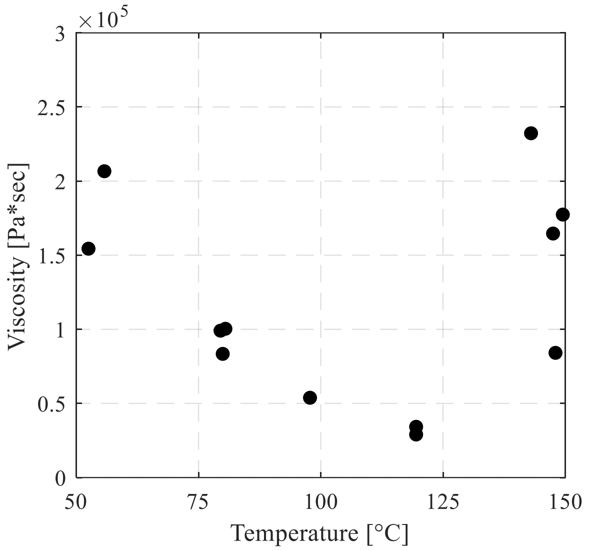

Figure 2.12. Viscosity at low shear rate against temperature.

It is worth to notice that for the Castro-Macosko fitting process, the experimental data should include the viscosity evolution as a function of the temperature, the shear rate and of the degree of cure. However, the degree of cure was not directly measured during the squeeze test, but it was evaluated by the DSC tests. The kinetic experimental data were used for fitting the parameters of the Kamal-Sourour kinetic model, and the output cure degree from the kinetic model then used for fitting the reactive viscosity model. The range of temperature at which the squeeze tests were carried out were substituted in the kinetic model. The degree of cure at a specific temperature and time was evaluated from the fitted kinetic model and then inputted in the reactive viscosity model according to the testing temperature.

For the optimization process of the parameters of the Castro-Macosko model, the shear rate was kept constant, which means that the viscosity depends only on two variables: the temperature and the degree of cure. Accordingly, the following parameters were considered as known:

- The α_g, i.e. the degree of cure at the gel point was set equal to 0.42;
- The shear rate $\dot{\gamma}$ was set equal to 1 s^{-1};
- The τ^* was set equal to 10;
- The degree of cure $\alpha(T,t)$ at a specific temperature and at a specific time was taken from the fitted Kamal-Sourour model.

The time at which the degree of cure α(T,t) was evaluated was different for each considered temperature. Indeed, during the squeeze test, the warm-up time to guarantee a homogeneous temperature distribution across the sample thickness was varied for each tested temperature.

The parameter optimization code was written in the Matlab environment, and a Bayesian optimization strategy was implemented. This optimization is an adaptive algorithm based on a gaussian process model, designed to achieve a near-optimal solution with a limited number of evaluations and a low computational effort. An initial response surface is fitted according to the training points, and, for all iterations, a new point (referred as infill point) is selected. This infill point is selected by means of an acquisition function that balances the exploitation (evaluating points with low mean) and the exploration (evaluating point with high uncertainty). Accordingly, the domain is explored not according to a static DoE scheme, instead avoiding the localization of the search in a region of the domain where a local minimum is present [71].

Before performing the optimization, a trial-and-error process was carried out to identify the most influent parameters on the model response. In order to set-up a bi-dimensional optimization problem, only two parameters where chosen. The parameters that mostly influence the model output were the exponent n and the T_b (see eq. 2.5). The optimization strategy was targeted at minimizing the mean squared residual error, i.e., the difference between the experimental viscosity evaluated at a shear rate equal to 1 s^{-1} and at a specific temperature, and the analytical model value. The optimization process was set as follow:

$$\begin{aligned} &min \qquad && MSE = \sum_{k=1}^{P} (f_k(T_b, n) - F_k)^2 \\ &subject\ to \qquad && 50000 < T_b < 70000 \\ & && 0.07 < n < 1 \end{aligned} \tag{2.11}$$

As the parameters c_1, c_2 (see eq. 2.6) and B had less influence on the model response, they were assumed after a simplified trial and error process and starting from standard values found in literature.

The algorithm evaluated a total of 30 points across the domain and found a minimum after 21 iterations with a total elapsed time of 19.58 seconds. The objective function surface is shown in Figure 2.13, and the final optimized parameters are reported in the Table 4

α_g (-)	c_1 (-)	c_2 (-)	B (Pa.s)	T_b (K)	n (-)	τ^* (Pa)
0.42	2.214	1.764	1.19e-29	62046	0.08228	10

Table 4. Cross Castro-Makosco model optimized parameters

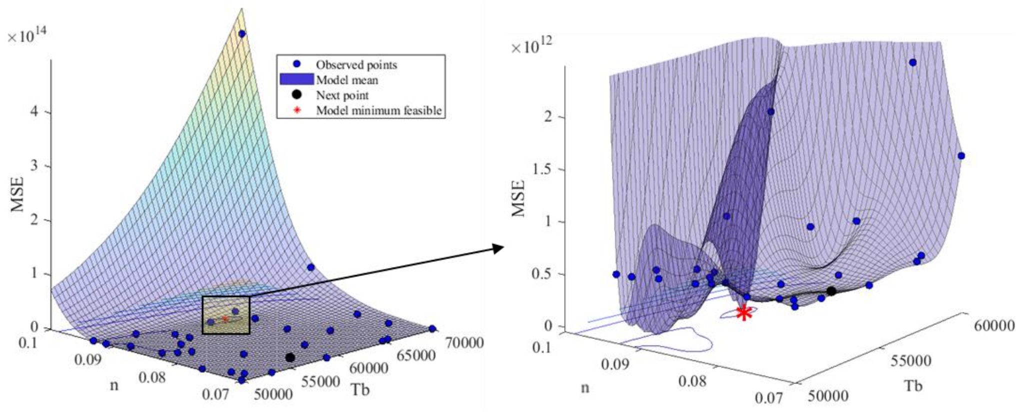

Figure 2.13. Bayesian optimization response surface with a detailed view of the area of interest where the model minimum is located.

The Figure 2.14 shows the experimental points of the viscosity as a function of the temperature and the prediction made with the fitted Castro-Makosco analytical model. It is possible to notice a good agreement of the values of the viscosity and its trend over temperature generated by the Cross-Castro-Macosko analytical model and the ones measured by the squeeze test. The R2 value calculated between the experimental data and the model is equal to 0.82. Thus, the model parameters can be used for the material card fitting during the process simulations.

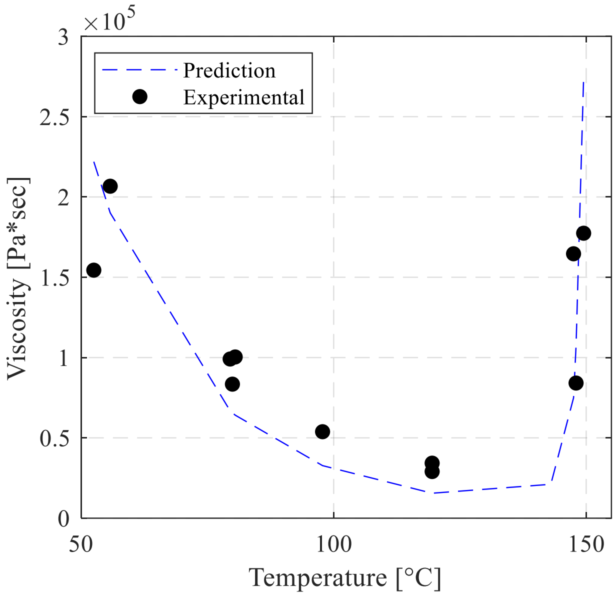

Figure 2.14. Fitting viscosity over the temperature

3 Process Analysis

One of most diffused and effective process for the manufacturing of components made up of thermoplastic and thermosetting polymers is the Compression Molding (CM) technique [72,73]. Considering the thermosetting composite materials, the CM technique is sometimes preferred for the manufacturing of fiber reinforced polymer parts over other process such as the hand lay-up or the infusion vacuum bag. This is mainly due to the high production rates obtainable, that makes it suited for a mass production. Complex shapes including ribs, curvatures, holes, can be obtained with a minimum labor cost. Furthermore, the excess scrap material is limited compared to the other before mentioned processes, where the wastes coming from the production can reach up to the 50% of the raw material [74]. Lastly, the compression molding process has the ability to produce parts with consistent fiber volume fraction, and good surface finish, as the high pressure helps to remove any surface defects. However, there are also some disadvantages to using compression molding. The process requires the use of specialized equipment and tooling, which can be expensive. Additionally, the process is not suitable for producing thin-walled parts, as the high pressure required for consolidation can lead to high fiber stresses and potential failure.

In the CM process, two matched metal molds (male and female) compress and give the intended shape to a raw material compound (charge or precharge) by applying a defined force. The mold closing pressure let the charge material flow, fill the whole tool cavity according to the mold geometry.

The CM process can be summarized in the following steps:

1) *Preheating of the mold* at a temperature lower than the gel point of the resin but high enough to reduce the viscosity of the material.
2) *Placement of the charge on the mold surface*. This step requires particular attention as the temperature, shape, mold covering and position of the charge influences the flow direction, the fiber orientation, the weld-lines formation and the quality of the final product. Furthermore, the raw material quantity must be carefully chosen, as it must be equal to or slightly higher

than the volume of the final component. If it is less, the final piece will have some cavities. The excess material creates some "flashing" that must be trimmed from the piece after it is removed from the mold.

3) *Closing of the mold and pressure application*. The male and the female tools are closed, and a pressure is applied on the material. The closing force is controlled and depends on the component surface and on the material properties. As the pressure inside the mold cavity builds up, the material starts flowing and fills all the mold cavities.
4) *Curing Cycle.* After the mold cavity is filled up, a temperature profile is applied and the material cures and consolidates. Dealing with prepreg materials, this step is usually the most time demanding, and the temperature ramp depends on the resin cure kinetics.

The molding compounds commercially used are the so-called Sheet Molding Compounds (SMC) and the Bulk Molding Compounds (BMC). Both are fiber reinforced thermoset compounds.

The SMCs are thin sheets made of randomly oriented fibers with a fiber length usually between 15mm and 50mm embedded in a B-stage resin. The typical thickness of the SMC sheets is in the order of 3mm [75]. Common polymers used are Polyesters, Vinylesters, Epoxies or Phenolic resins. The fibers are present in a form of bundles of individual filaments randomly oriented in the plane of the sheet. The stacking and the placement operation of SMC (Sheet Molding Compound) charges on the mold surface is a crucial step, as it greatly affects the flow properties and final product structure. The weld lines are formed when two or more material fronts meet, causing the fibers to re-orient in a direction parallel to the weld line and accumulating the resin and the trapped air. Weld lines are weak points in the final component and their presence dramatically impacts its performance. Therefore, when using multiple charges, special attention should be given to the weld lines position and orientation, in relation to the direction of the load that the component is expected to undergo during its operational life. [76].

The BMC compounds are similar to the SMC, with the difference that the charge does not have a thin sheet shape, but it is a bulky agglomerate. During the compression stage high flow is generated with higher fiber rearrangement compared to the SMCs.

Both BMC and SMC contain discontinuous or chopped rows of fibers that during the flow stages reorient themself according to the flow direction. In order to enhance the properties of the final composite part, the prepreg compression molding (PCM) technology is recently gaining more interest. In the PMC, a continuous long fiber prepreg charge is disposed on the press tool and covers all the mold surface. During the forming phase the prepreg is shaped, no fiber reorientation occurs and only the resin flow takes place [77]. This technology allows to obtain continuous long fibers structures with enhanced mechanical properties suitable for structural applications. However, it is important to note that the choice of material for compression molding will depend on the desired properties, as well as their processability for specific structures and cost. For instance, while PCM is effective for producing continuous long fiber structures with enhanced mechanical properties, it may not be suitable for molding deep and narrow ribs due to its limitations in flow. In contrast, SMC has better flow properties and may be a more suitable option for such applications.

Although the chopped charge considered in this study can be approximated to an SMC material, several morphological differences can be found. The SMC presents randomly oriented fiber tows embedded in a polymer paste. Instead, the chopped charge presents prepreg cuts with a woven structure. Each chop composing the charge individually contains both matrix and fiber, and it can move as a single unit, or get agglomerated and stack with other chops. Furthermore, the interface between two chops can be compared to a weld-line, as in that region the fibers reorient themself along the interface direction and the voids and air traps concentrates.

However, the formability and the flow characteristics of the chopped charge require deeper study. The aim of this chapter is to analyze the melt flow evolution during the compression molding stages and correlate the final part structure with the initial molding conditions.

The flow properties of the SMC material have been widely studied in literature. Several models and interpretation of the SMC flow pattern have been proposed [78–81]. The flow characteristics and the velocity profile strongly depend on the mold and component geometry, on the fiber content, on the resin viscosity and on the molding temperature. Commonly, the non-slip condition at the mold-charge interface is an accepted and reliable hypothesis. This flow condition generates through the thickness a shear-flow with a parabolic velocity profile. However, for thick charges (such as BMCs) the viscosity gradient across the compound thickness is enhanced by the temperature inhomogeneity between the skin and the core layer. Indeed, the boundary layers (skins) that get in contact with the hot mold face, softens respect to the core layer and acts as a thin lubricant layer facilitating the slip of the SMC charge over the surface [79,80]. However, in case of pre-charge with a high fiber volume fraction, the flow properties are less influenced by the boundary conditions at the mold wall interface [82]. The viscous properties present anisotropic behaviour more dependent on the interactions between the reinforcements, as the flow is dominated by the shear forces generated between adjacent fibers [82,83]. Accordingly, as the chopped charge presents high fiber volume fractions, the assumption of the shear flow condition for the characterization of the chopped charge response can be considered appropriate [82] and will be experimentally validated in the next sections.

3.1 Melt flow analysis

Compression molding tests were conducted to evaluate the evolution of morphology and flow during the mold filling stages using chopped charge as the material. The porosity, flow front advancement, and local fiber volume fraction were analyzed to understand how these properties changed during the flow phases. The tests used a simple planar steel tool with a 300 mm diameter to produce circular flat plates (Figure 3.1. Compression molding test set-up). The effect of the initial charge position and shape was investigated by testing two different configurations of the mold. In the first configuration (named CP25), the charge had a nearly circular shape and covered 25% of the tool. In the second configuration (named CP100), the chops were randomly placed on the tool and covered 100% of the mold surface. The tests were performed using a servo hydraulic press manufactured by AP&T, which can generate a maximum force of 1200 tons and has a maximum speed of 350 mm/s.

3.1.1 Partial initial mold filling

In the CP25 configuration, the charge flowed towards the edges of the mold and the morphological structure of the melt evolved during the pressing stage. To evaluate the advancement of the flow front and the evolution of porosity along the cross section of the component, partial compressions of the charge were performed by stopping the mold closing at different stages to obtain plates with different thicknesses and evaluate the evolution of the structure.

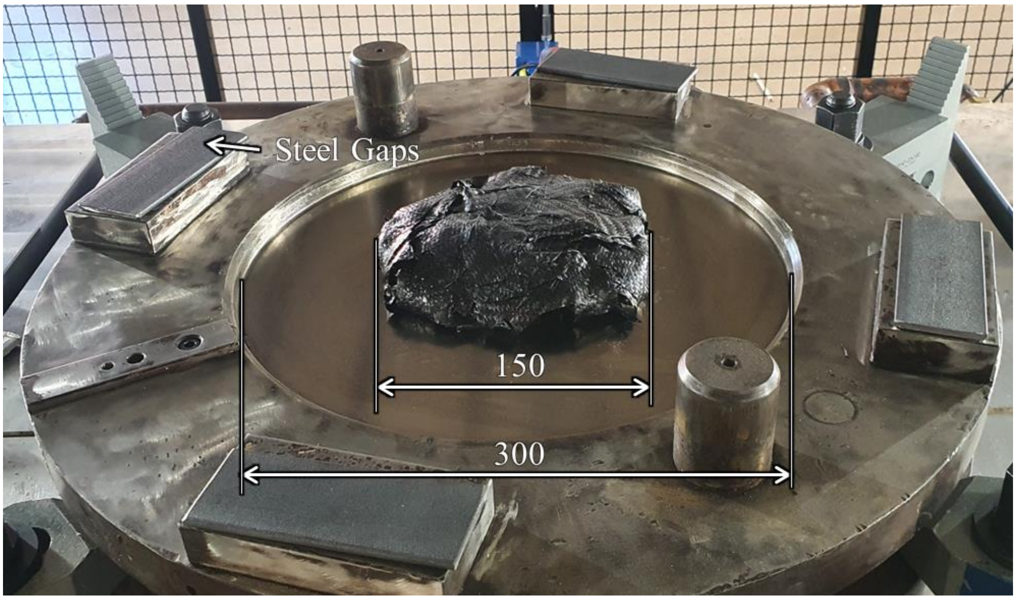

Figure 3.1. Compression molding test set-up

A circular charge composed of prepreg chops with a dimension of 20mm by 20mm was placed in the center of the circular tool (Figure 3.1. Compression molding test set-up). The mass of the charge was approximately 310gr and the initial surface filling was the 25% of the mold area. The minimum closure gap between the upper and lower tool surfaces was set to 2mm in order to avoid the male and female tool to get in contact and damage the mold surfaces. Four compressions (three partial compressions and one full compression) were executed. For all the tests the same charge weight and dimensions were used. In order to guarantee a partial closure of the mold and thus evaluate the flow at different stages, 8 steel gaps were placed on the centering edges of the tool. Accordingly, once the upper tool gets in contact with the steel gaps, the final thickness of the laminate is given by the sum of the steel gaps thickness plus the closure gap between the upper and lower tools. The maximum press force was changed according to the needed final thickness of the plate. As seen in the section 2.1.3, the force profile presents an exponential trend as a function of the closure gap. Indeed, for the high plate thicknesses (and thus high closure gap), low flow is induced, and lower force is needed to compact the material. Before each compression test, both the tool surfaces were cleaned and treated with three coats of a mold release agent that were applied 30 minutes apart.

Plate **[-]**	**Steel Gaps** **[mm]**	**Max Force** **[kN]**	**Final Thickness** **[mm]**
P1	8	100	9.96
P2	3.5	200	5.40
P3	2	200	3.86
P4	-	300	2.95

Table 5. Process parameters for the three partial CM plates (P1-P3) and for the full CM plate (P4)

The Figure 3.2 shows the press closing profile in terms of gap and force. Note that the graph qualitatively represents the press cycle, and the axes are not scaled. The left Y axis shows the closure gap, i.e. the distance between the upper tool surface and the lower tool surface. The closing cycle presents 6 steps in the evolution of closing stroke. The step 1 is the so called “free fall step”, in which the upper mold moves down from a gap of 400mm to a gap of 50mm at a speed of 300mm/s. During the step 2, the tool moves at a speed of 22mm/s from G5=50mm to G4=45mm of gap. Note that the gap of 45mm is approximately equal to the initial height of the charge. Therefore, at the end of the step 2 the upper tool gets in contact with the upper surface of the charge. The step 3 consists of a slight compaction of the charge: the tool moves from a gap of G3=45 mm to a gap of G2=40mm at a constant speed of 2mm/s, in order to compact the chop layers and let the excess air to escape. During this step, no relevant melt flow occurs. The subsequent step consists in the compression and flow stage. The press moves at a speed of 1mm/s from G2=40mm to G1. The gap G1 depends on the partial compression test and on the steel gaps used (Figure 3.2). At this stage, the force starts to rapidly increase, the melt flows and fills the mold cavity. The value of the maximum force F depends on the partial compression carried out, as illustrated in the Figure 3.2. During the last step, the force F is kept constant from the time t4 to the time t5, i.e. for approximately 90 minutes.

The temperature profile was consistent with the evaluation carried out in the squeeze-flow analysis. The mold was preheated at a temperature equal to 100°C and this temperature was maintained during the charge placement. According to the data sheet, the resin has a gel time of 6 minutes at a temperature of 125°C.

Therefore, the preheating temperature was chosen to prevent the start of the cross-linking reaction. At the time t4, i.e., after the compression was completed, the temperature of the mold was increased up to 140°C and this temperature kept until t5. After the time t5, the pressure was released, and the upper mold came back to the gap position G5. Note that, for the test 4, i.e., the full mold filling, the force of 300kN was chosen in order to have a molding pressure of around 4.2 MPa. This compaction pressure guarantees a full filling of the mold, good thickness homogeneity of the plate and was chosen according to some trial-and-error tests preliminary executed.

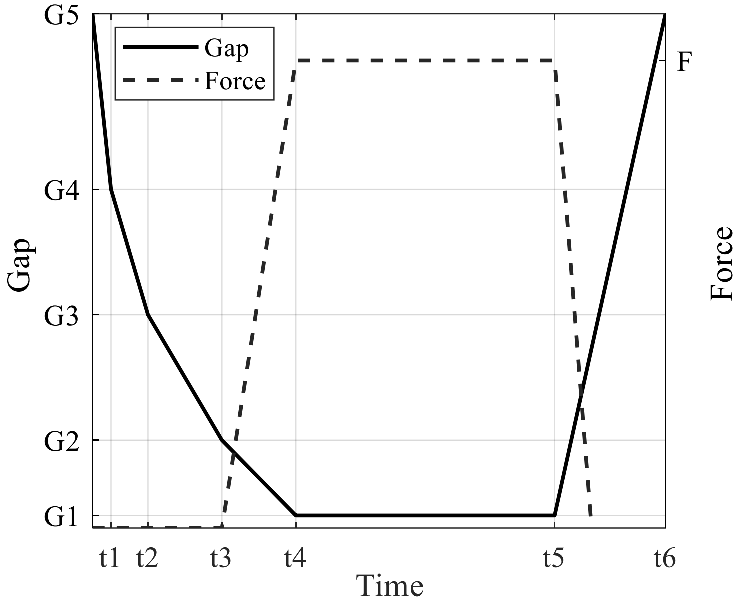

Figure 3.2. Compression molding steps in terms of closure gap (left axis) and applied force (right axis). The axis are not scaled.

3.1.2 Results and discussion

The results of the partial press tests are shown Figure 3.3. The pictures were taken after the extraction of the plate from the mold. No cleaning of the surface was needed as the surface finishing was good enough to appreciate the superficial fiber orientation. It can be observed that in plates P1, P2, and P3, the fibers tend to orient along the flow direction, i.e., radially. This orientation is more pronounced in plates P2 and P3, as the shorter press stroke in P1 resulted in less compression, leading to less radial orientation of the fibers. In the plate P4, radial orientation of the fibers is also evident, but near the edges, there is a tendency towards random orientation or circumferential alignment of the fibers. This behavior is likely due to collision of the fibers with the mold edges and resultant reorientation. The flow front in the plate P1 (see the picture at top left of Figure 3.3) seems to advance without any symmetry. The material spreads out not homogeneously due to the irregularities in the initial thickness of the charge and the interaction between the chops, which create shear forces that vary based on the local orientation, warpage and potential crimp of the fibers. Looking at the plate P2, a non-symmetric flow occurs. Part of the material charge flows up to 150mm from the plate center and reaches the mold edges, another part (in the picture of plate P2, the upper-right part) the material flows only up to around 95mm. The plate P3 confirms this flow inhomogeneity. The preferential flow direction is still the bottom-left one. In this portion, the material gets in touch with the mold edge for a larger circumference, while in the right part the material did not get in contact with the mold edges, and it is still evident a scattered front profile.

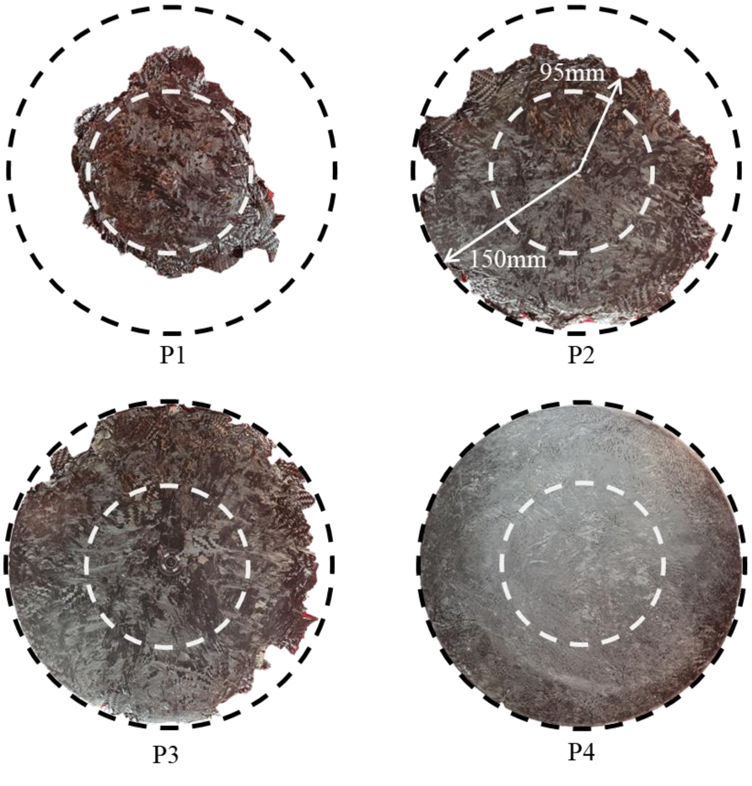

Figure 3.3. Partial compression molding tests (P1-P3) and fully pressed plate (P4). The black circular dashed line represents the mold edges; the white circular dashed line represents the initial charge location and dimension.

This tendency is likely due to the irregularities of the chop distribution within the charge and slight lack of parallelism between the two tools.

The shear flow and no-slip hypothesis at the mold wall were also confirmed by the partial CM tests. A detail of the melt front for the three partial CM configurations is shown in Figure 3.4. Considering the plate structure along the cross section, the central portion (core) is mainly composed by undeformed chops that keep their original structure. The chops are rigidly transported and move according to the flow direction. The thin material layer (around 0.3-0.5mm) on both the top and bottom faces (skins) is subjected to the mold friction, that tends to retain the chops and to form two boundary layers where the no-slip condition occurs. Due to this friction, the chops loose their initial structures and the tows orient themselves in the flow direction. The chops of the core layer move faster than the material in the boundary layer as can be seen in Figure 3.4: the undeformed core chops lay out with advance respect to the chops at the boundary layer. Another aspect worth of note is related to resin accumulation on the melt front and in correspondence of the skins (see plates P2 and P3 in Figure 3.4). These rich resin spots spreads in different locations of the melt front and are mainly due to the difference in the flow properties between the fiber and matrix. In fact, during the flow phases, the viscosity of the resin decreases due to the high temperatures.

P1 P2 P3

Figure 3.4. Flow front details of the partially compressed molded plates. The arrows put in evidence the resin accumulation in the flow-front.

The fibers of the boundary layer tend to stick on the mold surface, but as the compression pressure increases and higher shear forces are generated, the resin flows radially and accumulates along the melt front. Furthermore, as it can be seen from the pictures of Figure 3.4, part of the air initially entrapped in the charge is transported in the melt front and accumulates as small bubbles in these resin-rich spots. This air is then expelled from the mold cavities. However, based on a qualitative visual analysis (Figure 3.4) it appears that the resin accumulation phenomenon is less likely to occur in the core where the resin does not run away from the fibers. Nevertheless, additional research may be necessary to validate this observation.

Considering the plate P4, i.e. the fully pressed one, it was not possible to visually verify the fiber orientation distribution across the thickness. Indeed, after a full compression, it was necessary to understand if the chops in the core layer still keep their pristine undeformed structure. Accordingly, a layer peeling analysis was executed: a portion of the plate large enough to capture the internal inhomogeneities was cut and burnt in the oven at 400° to fully carbonize the resin. The chops were gradually removed using a tweezer to capture the evolution of the structure along the thickness. The results are shown in the Figure 3.5. The top boundary layer (i.e. the layer in contact with the upper tool) presents highly oriented fibers (Figure 3.5a) for a thickness of around 0.3-0.5mm. After peeling this layer off, the core layers become visible (Figure 3.5b). These layers are confirmed to be composed by almost undeformed chops that keep their original structure and there is no evidence of warpage or deformation. The core layer has a thickness of around 1.9-2.3 mm. The bottom boundary layer presents almost the same fiber structure of the top boundary layer. In the picture of Figure 3.5c however it seems that the bottom layer (i.e. the layer in contact with the lower tool) has a slight different structure than the top boundary layer, as, apparently, there is the presence of intact fiber tows detached from the boundary layer. This dissimilarity could stem from two potential causes. Firstly, there may be a weaker interaction between the fibers in the bottom boundary layer and the lower mold, compared to the top boundary layer and the upper mold. Alternatively, the peeling operation might have introduced a bias, as it was challenging to peel the upper chop layers homogeneously while keeping the bottom ones intact. It is author opinion that these factors may have contributed to the observed structural discrepancy between the top and bottom layers.

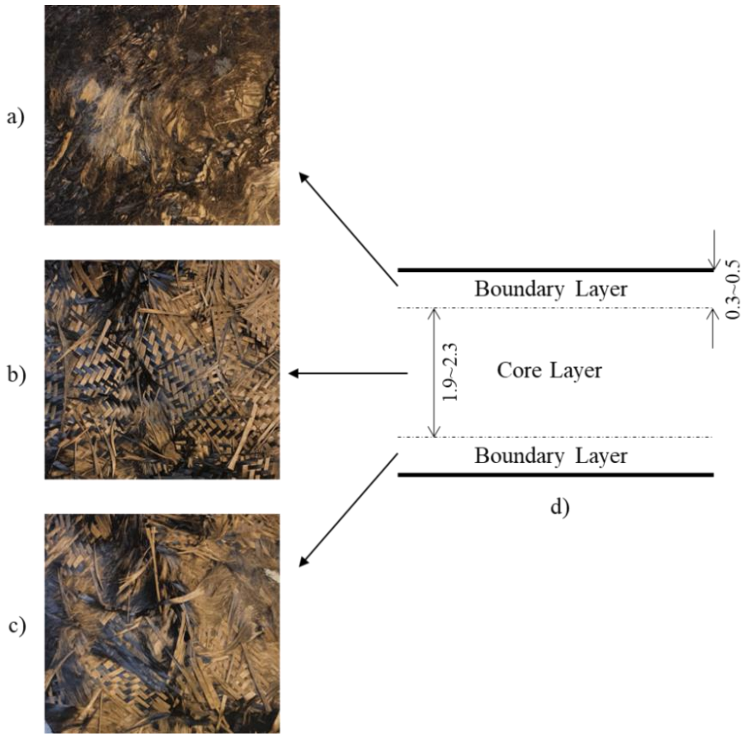

Figure 3.5. Peeling analysis of the P4 plate: a) upper boundary layer; b) core layer; c) bottom boundary layer.

It should be emphasized that computerized tomography (CT) techniques, such as those presented in section 3.1.3, could offer a more accurate assessment of fiber orientation throughout the thickness of a plate. However, the CT scanning of carbon fiber materials can present challenges, particularly when trying to capture high-resolution images of the fiber orientation. Specifically, achieving high resolution typically requires narrowing the field of view, which limits the area that can be analyzed in detail, often to only small sections of the component (up to 20mm, based on the author's expertise in the subject). This limited field of view can make it challenging to gain a comprehensive understanding of the overall fiber orientation across a large area, which was required for this study. The peeling approach provided instead a more global perspective on fiber orientation across a much larger area of the plate, from the center to the edge and allowed to investigate how the fibers tended to reorient themselves during compression phases.

The evolution of the voids during the pressing phases is illustrated in Figure 3.6, which shows the cross-section micrographs of the 4 produced plates. The micrographs were obtained by merging several images taken with an optical microscope at 5x magnification level. The trapped air mainly accumulates at the interface between the chops. Initially (P1 plate) the voids have a rounded and regular shape, but as the pressure increases and therefore the plate thickness decreases (P2 and P3) the voids tend to stretch towards the flow direction. The voids elongates and they can reach dimensions greater than 5mm. These air spots are located at the interface between the chops (inter-layer voids), and once the flow stage is completed, they are almost totally ejected from the mold cavities. This effect can be better appreciated in the Figure 3.7b, that shows two details of the melt front cross-section of the plate P3. From the figure it is possible to see the air accumulation in correspondence of the melt front that generates a large void that is then expelled at the end of the compaction stage (t4).

Figure 3.6. Micrography of the partially molded plates (P1-P3) and of the fully molded plate (P4).

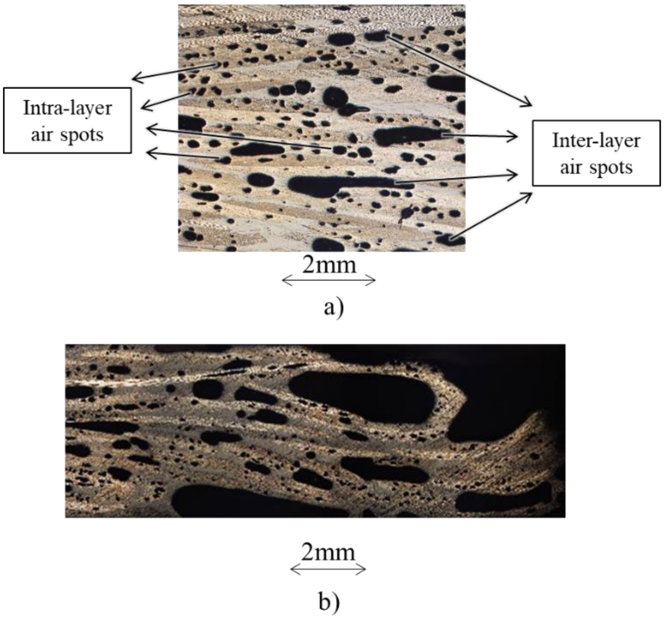

Figure 3.7. Cross-section micrography of the partially molded plate P3: a) detail of the central region of the plate; b) detail of the flow front region of the plate.

The inter-layer voids tend to move during compression and flow towards the melt front, where they accumulate in a single air bubble with a greater dimension than those present in the rest of the plate. In this area, the chops tend to reorient along the thickness direction and assume a swirl pattern.

The intra-layer voids are trapped air within the prepreg and within the chop tow (Figure 3.7a). The dimension of these voids is much smaller than the inter-laminar voids (tenth of millimeter) and presents a rounded shape. Their shape does not change during the flow stages (Figure 3.6, P1-P3) and neither according to their location in the plate (in correspondence of the flow front, the intra-layer voids present the same size as in the rest of the plate). Indeed, as these voids form inside the layers, they move rigidly together with the chop, and are then expelled after the melt flow stage, i.e., during the final compaction phase.

The air movement from the center to the edge of the plate was confirmed also by the porosity analysis. The porosity of the three plates was evaluated in two locations of each plate, specifically at the center of the plate and in the melt front region. The porosity was evaluated by analyzing the cross-section micrography and computing the percentage of the void area respect to the total evaluated specimen area of each acquired image. The

Table 6 recaps the porosity evolution for each produced plate and for the two considered locations. The plate P4 is omitted as the evaluated porosity is lower than the 1% and thus can be considered negligeable. As it was expectable, the porosity decreases as the compression proceeds, but it's interesting to notice that for all the plates, the porosity increases moving from the central portion to the front flow region. This confirms that for this charge configuration, i.e. a partial coverage of the mold that induces high flow during the CM process, the air is transported to the flow front and then expelled from the mold cavities.

Plate	**Porosity** Central region	**Porosity** Front region
P1	20.7%	23.1%
P2	12.4%	17.1%
P3	11.3%	13.9%

Table 6. Porosity at different location of the partially molded plates (P1-P3)

This effect did not occur in the case of a full initial mold filling, as will be explained in the next section.

3.1.3 Full initial mold filling

The influence of the initial position and shape of the charge on the meso-structural properties of the final component was analyzed by producing a plate with an initial mold surface filling of 100% (configuration CP100,

Figure 3.8). This configuration will be named with the acronym CP100 (circular plate 100%)

The charge was arranged to completely fill the cavity of the lower mold. The chops were disposed onto the mold uncompacted and were homogeneously arranged over the lower tool surface. This step required particular attention, as the chops stick each other, and a uniform distribution could be tricky. Accordingly, before the charge distribution on the mold, the chops were refrigerated at minus 20 degrees for 30 minutes. This ensured easy detachment of the chops from each other and allowed to homogeneously distribute them on the mold surface. The processing conditions (temperature, pressure profile and charge mass) were the same as for the production of the plate P4 as reported in the previous section.

Figure 3.8. CP100 charge configuration.

Figure 3.9 illustrates the surfaces of CP25 and CP100 plates. It is evident from the CP100 image that the chops retain their orthotropic structure even in the boundary layer. During the pressing of the charge, the chops compact together, but as they are distributed evenly over the entire surface of the mold, minimal flow takes place.

Figure 3.9. Surface comparison between the a) CP25 plate and b) CP100 plate.

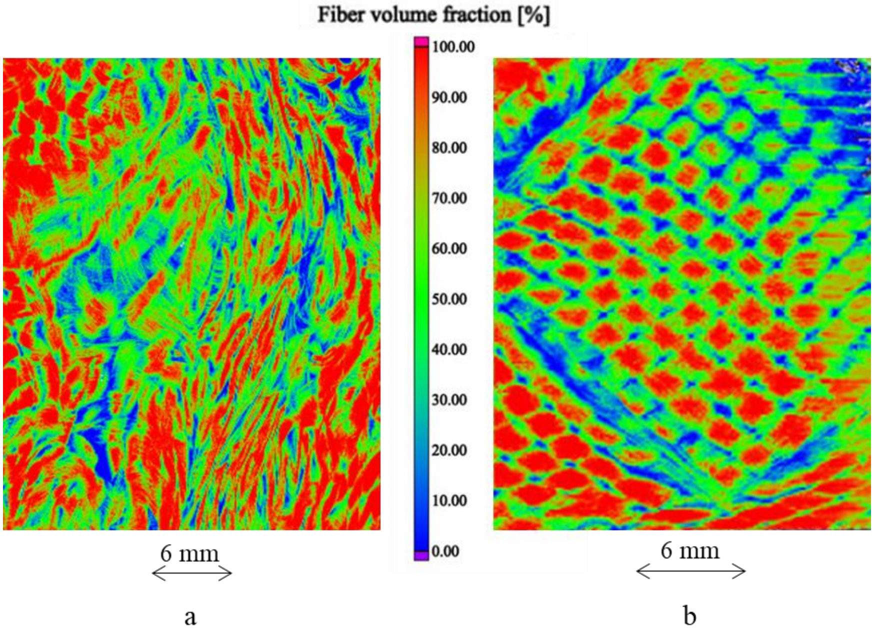

Figure 3.10. Micro-CT images of the surfaces of samples cut from the plate a) CP25 and b) CP100

This results in the formation of clearly defined interface regions between the cut-outs, which are areas of chop overlap where the matrix tends to concentrate. Figure 3.10 compares the Fiber Volume Fraction (FVF) between the CP25 and CP100 configurations. The images were obtained through computed tomography, and the FVF analyses were carried out using the VG Studio Fiber Composite Material package. It can be observed that in the CP100 configuration, the chops' boundaries are well defined by the areas where the FVF tends to zero (i.e., the Chops Interface Regions or CIRs). In contrast, the CP25 configuration has a more homogeneous distribution of fibers, which tend to be aligned along the flow direction, and no CIRs are visible. These CIRs are considered critical in the material as they are the sites of crack nucleation and propagation, as will be discussed in depth in the Chapter 4.

Although minimal flow occurs in the CP100 configuration, there are some spots where the chops tend to be more twisted or lose their original structure. This is due to differences in initial charge thickness. In fact, despite the chops have been evenly disposed on the mold, pressure inhomogeneity due to the initial charge thickness unevenness are generated as soon as the upper tool compacts the charge, as will be explained in detail in the next section.

Figure 3.11. Peeling analysis of the CP100 plate.

The peeling analysis was executed too. A portion of the plate was burnt as described in the previous section and the chop layers were peeled off to catch the chop orientation in the core layer (Figure 3.11). Except for the presence of some slightly warped chops, almost all the chops keep their pristine orthotropic structure also in the core layer. Accordingly, it can be stated that the configuration CP100 exhibits the same structure along the plate cross section and no differences in the chop/fiber orientation between the core and the boundary layer evidently emerged.

This aspect was also confirmed by analyzing the cross-section micrographs. The CP100 configuration assumes a laminated structure (Figure 3.12a): the chops tend to remain oriented in their plane not only in the core, but also in the boundary layers. This effect is less evident in the case of the CP25 configuration (Figure 3.12b), in which laminate-like regions are alternate regions in where the chops tend to bend and form a random orientation pattern.

However, the micrographs along the cross section showed the presence of not-negligeable voids in the CP100 configuration (Figure 3.12a). These voids range in size from 1 mm up to 2 mm and are inter-layer voids that mostly concentrates in correspondence of the interface regions between the chops.

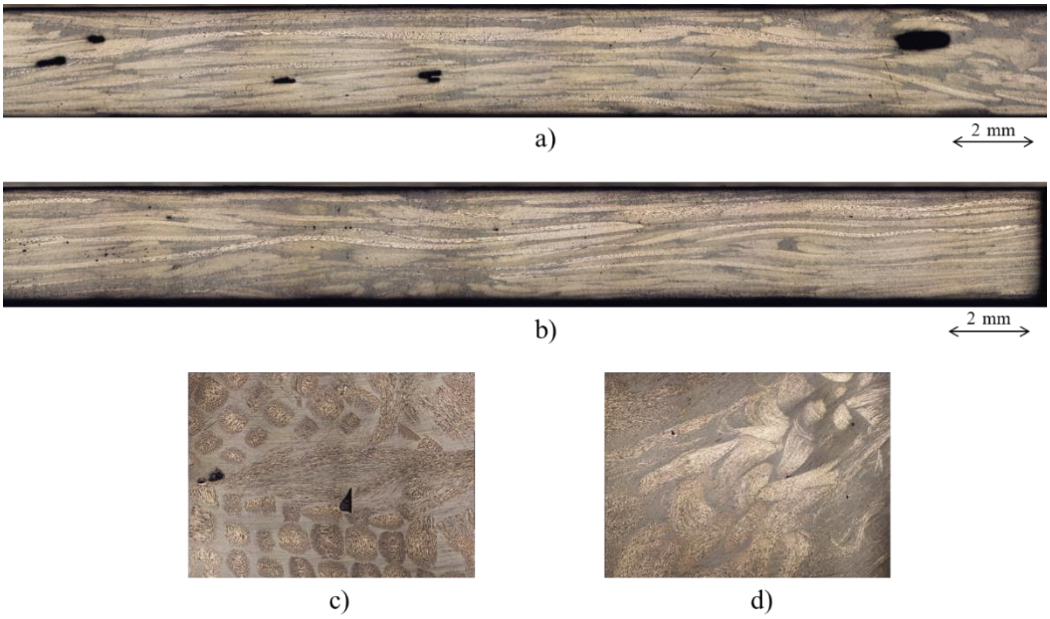

a)

b)

c)

d)

Figure 3.12. Micrographies of the CP100 and CP25 plates: a) cross-section of the CP100 plate; b) cross-section of the CP25 plate; c) surface detail of the chop interface region in the CP100 configuration; d) surface detail of the CP25 configuration.

These are regions where two or more edges of the chops come into contact and weld together. In correspondence of the interface region the formation of resin pockets and resin accumulations is also evident both in the configuration CP25 and CP100 (Figure 3.12a-b). The phenomenon of the superficial blistering was also found near these regions (Figure 3.12c) but only for the configuration CP100. The blistering generated superficial defects and slight surface unevenness across all the plate area.

3.1 Vacuum Bag process

The presence of an inhomogeneous flow direction due to thickness discontinuities in the CP100 configuration was explained by producing a plate using the vacuum bagging process. In fact, the vacuum bagging process guarantees a homogeneous pressure distribution over the entire surface of the charge. The vacuum bagging allows to understand which is the greatest homogeneity along the thickness that can be obtained by manually arranging the chops. Indeed, as the bag adapts to the material, and it does not induce any flow in the melt. On the contrary, the metal tools used in the compression molding process are rigid and theoretically undeformable. In this last case, if the charge presents thickness discontinuities, the mold first comes into contact with some parts of the material, forcing these regions to compact and generating an uneven pressure distribution across the charge.

The vacuum bag charge was composed by 206 grams of chopped material that was placed on an aluminum mold with dimensions of 300mm x 300mm (Figure 3.14a). The surface of the tool was treated with 3 coats of release agent. The chops were evenly arranged on the mold, trying to minimize possible differences in thickness. A perforated release film was placed over the chops, and subsequently the peel ply, the breather and the polypropylene bag were stacked (Figure 3.13). A vacuum pump was used to suck the air from the bag and generate a vacuum pressure of 1 bar. The mold was placed in an oven and the temperature profile was set as follow: temperature ramp from ambient temperature to 135°C in 60 minutes, hold 135°C for 90 minutes and cool down in ambient temperature.

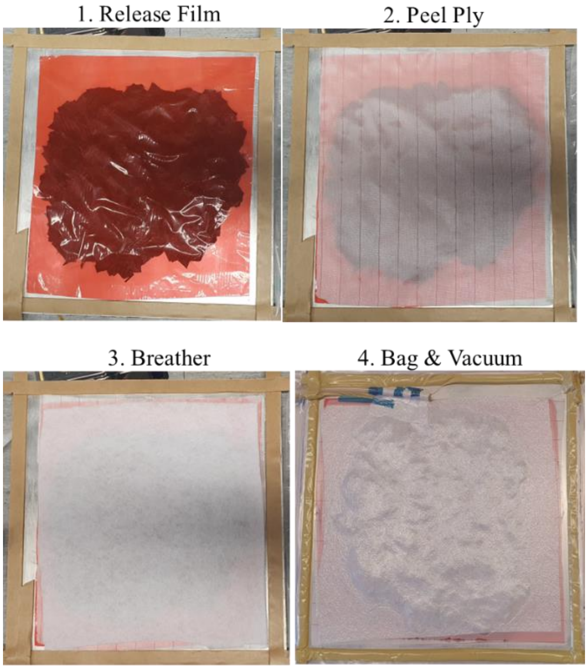

Figure 3.13. Layer stratification of the vacuum bag process.

The produced plate is shown in the Figure 3.14b. In the picture one can appreciate that with this manufacturing process no material flow took place. In order to quantitatively evaluate the thickness discontinuities, a 3D scan image was captured and post-processed with the GOM software. The average thickness value is 3mm within a range of 0.2−5mm (Figure 3.14c). From this picture it is evident the presence of several dips and crests even in the central part of the plate. This particular thickness profile explains and confirms the inhomogeneous melt flow direction that is obtained during the compression molding of the CP100 plate. Indeed, the mold gets in touch with the crests before, and from the crests a melt front starts to propagate. However, the direction of this melt front is not radial, but rather random, as its direction depends on the position of the crests and the amount of material (and thus the number of chops) under these crests. The air tends to be transported in the melt front, and if different front meets, the air is trapped inside (Figure 3.14c) and cannot be pushed out from the molt cavities. This phenomenon is then more marked in correspondence of the interface regions between the chops since the chops are rigidly transported with the melt front.

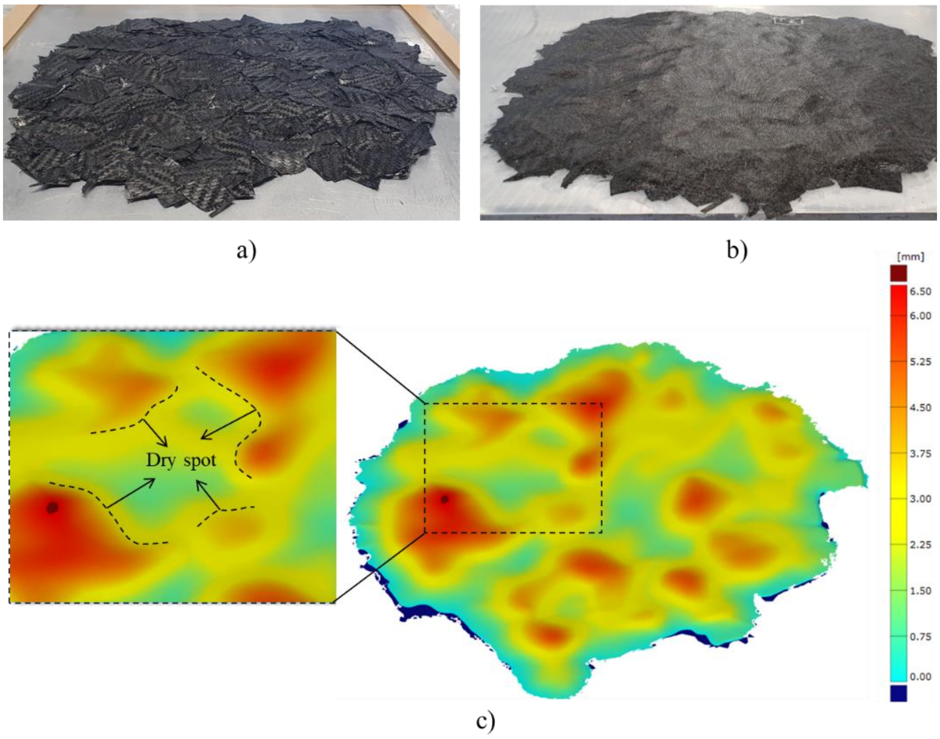

a) b) c)

Figure 3.14. Vacuum bag produced plate: a) chop disposal on the mold surface; b) final plate; c) thickness profile captured with the 3D scan and crests detail.

The Figure 3.15 illustrates a micrography of the cross-section of the plate produced with the vacuum bagging process. The difference in thickness between the left (2.5mm) and the right (4mm) side of the cross section is due to the different number of chops stacked across the thickness, but also to the presence of resin accumulation and resin pockets in the thicker side. The resin pockets have greater dimensions respect to those of the CP100 plate because the lower pressure generated by the vacuum process is not enough to let the resin flow.

Intra-layer voids are also evident in correspondence of the interface regions. These voids, as evidenced with the production of the plate CP100, even after a full compaction, tends to accumulate in correspondence of the interface region. The vacuum bag plate also gives an interpretation of the blistering phenomena evidenced in the plate CP100. The voids that generate the blistering usually forms just under the last material layer before the plate surface, at the interface between two chops (Figure 3.15). In the vacuum bag plate, these voids under the surface layer remains trapped and does not generate layer deformation or cracking. In the CM process instead, as the internal pressure of the entrapped air is released at the moment of the mold opening, this void tends to expand and may lead the superficial layers to expand and eventually crack and form unesthetic voids and defects on the surface of the component.

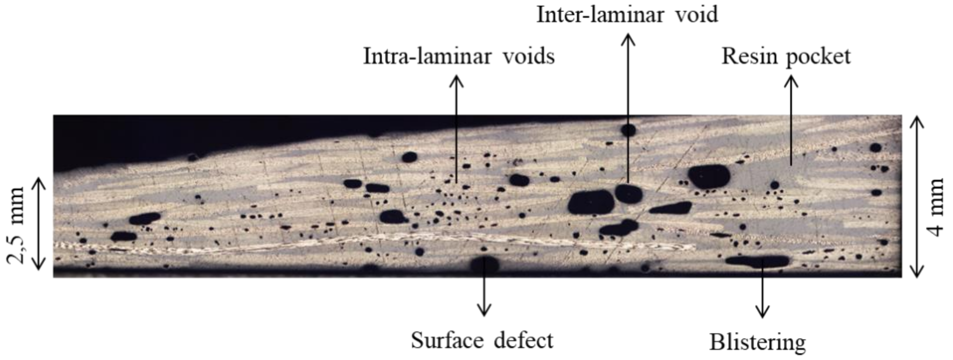

Figure 3.15. Cross-section micrography of the vacuum bag produced plate.

3.2 Conclusion and considerations

In this chapter, the formability of a charge composed of chopped prepreg was investigated. Two configurations were tested: the CP25 configuration, where the charge covered the 25% mold surface and the CP100 configuration, in which the charge was composed by chops homogeneously arranged on the surface of the mold to obtain an initial 100% surface filling.

Considering the results of the analysis done for the configuration CP25, the following considerations can be done:

- The fibers on the boundary layer tend to rearrange in the flow direction due to the no-slip condition at the mold wall interface;
- The core layer is composed by undeformed chops that rigidly move without any warpage;
- The chops in the core layer are stacked along the thickness direction;
- The flow advancement is mainly radial even if the front shape is not homogeneous along the circumference;
- The voids initially present in the charge tend to move towards the flow front and are then expelled through the mold cavities;
- The final plate P4 presents porosity (mainly due to intra-laminar voids) <1%.

Considering the results of the analysis done for the configuration CP100 instead:

- Low flow and low chop movement occur;
- The flow is due to the thickness discontinuity that form crests and dips on the charge;
- The flow is not radial, but is directed along random directions according to the location of the crests;
- The random flow does not allow the entrapped air to escape, and the final plate presents inter-laminar and intra-laminar voids;
- The voids concentrate especially in the chop interface regions;
- The chop interface regions present resin pockets and resin accumulation;
- Surface defects and blistering occurs especially in correspondence of the interface regions;
- The chops tend to keep their original orthotropic structure both in the core and in the boundary layers;
- The final structure is locally orthotropic and macroscopically random.

It is worth noting that both chop placement methods (CP25 and CP100) are practical and time-efficient solutions for medium production volumes in industrial applications. These methods are fast as they do not require a specific local chop re-arrangement, but rather a random placement on the mold. In the case of CP25, the only necessary operation is to pre-compact a charge with the desired weight and place it on the mold in a predetermined position. For industrial production, aiming at automating the process, multiple pre-compact charges of predetermined weight could be prepared in advance and inserted into the mold in an automatic way.

In the case of CP100, the only required operation is to uniformly place the chops on the mold and filling its surface homogeneously. Both solutions are fast and flexible and can be optimized according to the specific production needs.

The qualitative analyzes carried out of the final structure of the plates as a function of the initial process conditions are certainly useful for understanding the general behavior of the material when subjected to different flow conditions. In any case, it is necessary to quantify the mechanical performance to evaluate the configuration that guarantees the optimal mechanical response. In the next chapter, an extensive experimental characterization is proposed whose aim is the evaluation of the material properties under different load conditions and the assessment of the fracture mechanics as a function of the initial process parameters.

4 Mechanical Characterization

The stochastic nature of the manufacturing process incorporates uncertainty and unpredictability into the Discontinuous Fiber Composite (DFC) plates, which usually translate into scattered mechanical performance. The structural properties such as stiffness, strength, fracture toughness, initiation, and propagation of the crack, result to be different compared to the base material (continuous fiber system), and appear to be strongly influenced by:

- Fiber orientation within the chop
- Chop dimension (length, width, aspect ratio)
- Chop thickness
- Chop orientation distribution
- Resin system
- Manufacturing process
- Process conditions

Many authors investigated the properties of the DFCs and all of them demonstrated that the chopped structures present lower and scattered properties compared to the base continuous fiber system. The effect of the chop length on the mechanical performance was analyzed in [84,85] , and there was evidence that longer chops leads to higher tensile and bending strength but did not eventually affect the stiffness of the material. Higher chop size has demonstrated to strongly shift the ultimate strength toward higher value. Indeed, in this kind of structure the load is mainly transferred by shear between the chops. Lower chop dimension leads to premature failure due to the lower overlap interface between the chops [86]. Rashed et al [82] produced and tested specimens made up of thermoplastic woven prepreg and compared the effect of the chop overlap length. They demonstrated that by increasing the overlap the performance of the material increases, but beyond a critical overlap length the stress concentration near the ends of the chop leads to a premature failure initiation. Instead Wan et al [87] associated the effect of the platelet length to the internal structure irregularities that can be generated in smaller chops laminates. Indeed, smaller chops leads to irregular fiber clusters and out-of-plane rearrangement of the chops. However, a smaller size of the chop tends to homogenize the in-plane properties and reduces the properties variability. The chop thickness instead demonstrated to have a pronounced effect on the tensile properties of the component [88,89]. Thicker prepreg leads to an early onset of tow-debonding/ply delamination and reduces the number of crack resistance spot, where the crack can eventually stop its propagation. Furthermore, during the production process, more weak spots are created due to the higher thickness of the chop. Indeed, it is more difficult for neighbor tows to close the gaps and close the voids. However, it has been demonstrated that the tensile modulus is not significantly influenced by the ply thickness.

The properties of the final component depend not only on the composition and structure of the chops, but also on their distribution on the component, which in turn depends on the manufacturing process parameters. Indeed, the flow conditions can modify the stochastic orientation state and the weak spots within produced plate. Feraboli et al [84] cut specimens from a chopped plate in different orientation to verify the in-plane anisotropy. They found a bias in the average ultimate strength between the direction 0 and 90. This is because the flow-induced effects can modify the stochastic orientation state of the fiber, induce more or less chop agglomerates and matrix accumulation spots. Kravchenko et al [[90] tested specimen produced with different flow condition and demonstrated that the coupons have different properties according to the preferential fiber alignment. Also, the plate thickness has an effect on the material response: higher thickness means higher tensile strength [84,89,90] This effect is due to the peculiar crack propagation of this kind of structure. Rasheed et al [82] defined the tortuosity parameter to characterize the meandering crack path, as the ratio between the length of the crack path and the thickness. Then they studied the influence of this parameter on the material performance: greater the tortuosity, more resistance spots the crack found during its propagation, which leads to higher strength of the tested specimen.

The initiation and propagation of cracks in a DFC structure is a complex process that is influenced by the presence of weak spots, such as areas with a high concentration of matrix material, fiber misalignment and agglomeration, or any type of local stiffness discontinuity. Boursier et al [19] investigated the fracture mechanisms of the DFC structure. They found that the first crack location is not necessarily the spot from where the fatal fracture generates and propagates. The DFC structures indeed are more prone to start the crack respect to the continuous fiber composites, and the propagation is very different. During the testing they recorded some audible pings and tings related to the crack initiation, and they investigated the relation of the first crack sound to the ultimate strength. They found that the first crack appearance is not detrimental to the ultimate properties. This is because in the Fracture Process Zone (FPZ), significant non-linear deformations due to sub-critical damage mechanism (delamination, matrix cracking, chop debonding) promote the strain redistribution and mitigate the intensity of the stress field. Ko et al [91,92] carried out a size effect test campaign on notched specimen with UD thermosetting prepreg. They found that the FPZ is not uniform and decreases with the crack opening. The fatal crack did not always generate and propagate from the notch, but can generate from the weak spots distributed across all the specimen surfaces. A size effect was confirmed, and they found that, if the sample is sufficiently large, it has a more brittle behaviour and follows the linear elastic fracture mechanics. They highlighted that the fracture energy is from 2.8 to 5.5 times larger than that of the typical structural aluminum. An important aspect is that the DFC, compared to traditional continuous fiber composites, exhibits an higher pseudo-ductility and its strength seems to be not sensitive to defects, holes, notch and crack [92].

However, almost all the studies found in the literature proposed the characterizations of DFC structures made with UD platelets and thermoplastic resin [93]. De Souza et al [31] performed tensile, compression and short beam shear test on thermosetting composites reinforced with woven fabric. However, the chop dimension is in the order of 130mm by 130mm, and this value is larger than the chop dimension proposed in this study (20mm by 20mm).

In this chapter, it is proposed a complete experimental campaign aimed to fully understand the response of the DFC structure manufactured with fabric thermosetting prepreg. The influence of the chop thickness, and aspect ratio is investigated. Furthermore, specimens cut from the CP25 and CP100 plates are tested in tension and the resulting structural performance compared in order to analyze the flow-induced effects on the mechanical response and evaluate the degree of anisotropy. Finally, a size effect analysis on unnotched specimen is performed to evaluate the effect of the sample size on the fracture response and on the ultimate properties of the material.

4.1 Influence of the prepreg density

4.1.1 Material and Method

The material used was a plain carbon fiber and epoxy resin prepreg. The two types of prepreg used to produce the specimens for testing have different areal densities. One had a surface density of 204 g/m^2 and is made of 3K carbon fiber, while the other had a surface density of 600 g/m^2 and is made of 12K carbon fiber. The thickness of the first (204 g/m2, 3K) is approximately 0.3mm, while the thickness of the second (600 g/m2, 12K) is approximately 0.6mm. The plates from which the specimens were waterjet cut were produced by compression molding by using the same procedure and process conditions described in the section 3.1.3. Randomly oriented prepreg (chops) were used as the thermoforming charge. The flat mold had a size of 350x350cm, and the chops were placed to initially cover all the tool surface. Tensile test and three point bending test were performed on specimens produced with both the prepreg densities (600 gr/m^2 and 204 gr/m^2). The tests were carried out in the DIMEAS testing laboratory of the Politecnico di Torino using an Instron servo-hydraulic universal material testing machine. Figure 4.1a shows the three-point bending test set-up. Two adjustable cylindrical pins were used as support span, and the specimen was loaded with a cylindrical steel head, fixed to the hydraulic grips of the testing machine, and centered with respect to the support span. The specimen had an average thickness and width of 2.8 mm and 12.9 mm respectively, and the span was set equal to 42mm.

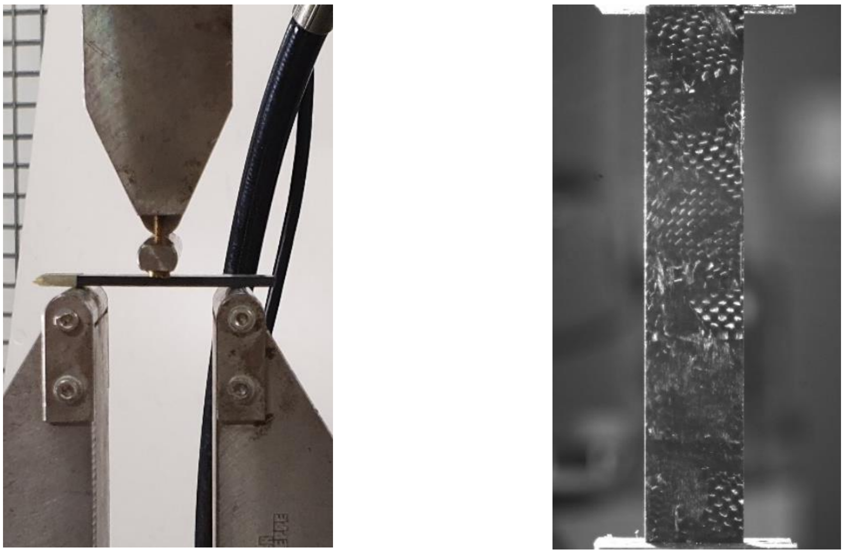

a b

Figure 4.1. Experimental test set-up: a) three point bending test; b) tensile test

The tensile test set-up is shown in Figure 4.1b. The specimen was constrained on both sides to the test machine grips. The tensile specimens were painted white, and a black paint speckle was created using an airbrush, to evaluate the deformation gradient through the Digital Image Correlation (DIC) system. The standard three point bending test were executed according to the ASTM D790, and the tensile tests according to the ASTM D3039.

4.1.2 Results

All of the results presented in this section have been normalized for comparison purposes. This means that the values have been adjusted based on the maximum load or stiffness obtained in the particular batch of specimens being tested. Normalizing the results allows for more accurate comparison between different batches or samples, and it also helps to protect the confidentiality of the company involved.

Figure 4.2 displays the results of the tensile test in terms of normalized stress-strain. For ease of understanding, only three curves from the tested batch are shown in the graph. These particular curves were chosen because they represent the three main failure behaviors that were observed during the testing of all the samples. It is important to note that, while the results from the other samples are not shown in the graph, they were still taken into account and analyzed in the overall interpretation of the data. Despite the dispersion, it is possible to group the results into 3 main categories, according to the failure type: 1) linear-elastic behavior until the ultimate strength and failure; 2) presence of one or more stress drops in the elastic phase, maximum strength, and failure; 3) linear-elastic phase followed by a “step-like” post-peak trend related to crack propagation. The stress values shown in Figure 4.2 were normalized as a function of the maximum stress value measured in the tests. Each of the identified failure modes can be linked to a specific type of crack initiation, nucleation, and propagation. In other words, the observed failure behavior is influenced by the way in which the cracks begin, grow, and eventually lead to failure. Understanding these relationships can help to identify the critical points at which failure is most likely to occur, and to develop strategies to mitigate or prevent these failures from happening.

Analyzing the material at a mesoscopic scale, it can be divided into two main structures: the orthotropic regions and the Chop Interface Regions (CIR). The orthotropic regions are material portions where the prepreg chops keep their pristine orthotropic structure. The CIR are transition areas between one chop and another. Here, the fibers of the chops can create agglomerates, the resin accumulates, and the fibers form a swirl path. The CIR represent a material discontinuity, where stresses can concentrate, and thus, according to their position and orientation, they can highly influence the material mechanical response.

Figure 4.3 shows the deformation map of the tested specimens acquired through the DIC system. The maps show the deformation state of the specimens immediately prior to their ultimate failure. The behavior of type 1 is associated to a localized nucleation and propagation of the crack. As it can be seen from Figure 4.3a, the maximum deformation region is restricted to the primary nucleation site: the fracture propagated transversally from the nucleation tip and extended between the two edges of the specimen, following the path of a CIR.

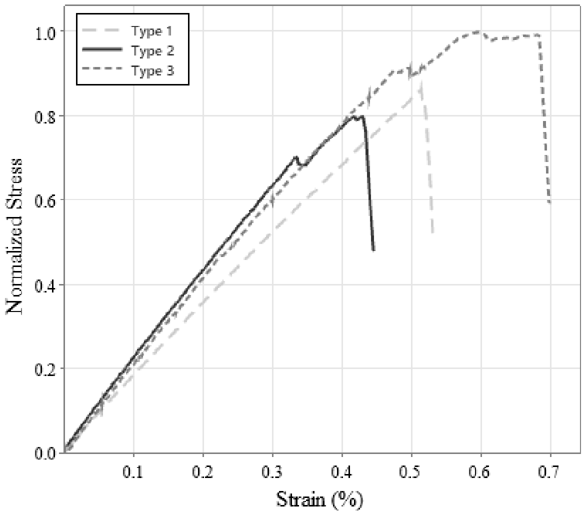

Figure 4.2: Tensile test results, normalized stress as a function of the strain

In the case of type 2 small load drops were detected in the linear-elastic phase. During the test, some cracks and tips were audible, associated to the presence of secondary nucleation sites, i.e., regions where cracks initiated but did not cause the failure. Near to the edges of the central section of the specimen a secondary nucleation site is evidenced in Figure 4.3a (highlighted by the white dashed box). The crack paths of the type 1 and 2 are shown in Figure 4.3b. The crack followed the path of least resistance, passing through the CIR and the rich resin areas. In this case, the chops were aligned along the thickness, leading the crack to easily propagate across the rich matrix areas.

Considering the type 3 behavior, the zones of maximum deformation were more extended (Figure 4.3a) than for the other two types, and the specimen globally demonstrated a higher maximum deformation than the type 1 and 2 behaviour. Multiple fractures generated in different portions of the specimen caused by the simultaneous presence of primary sites over a wide portion of the specimen surface. There was an extensive degradation of the properties, which generated a post-elastic load trend characterized by a plateau and load oscillations. Analyzing the fracture along the thickness, an extended stepwise crack path and chop debonding is noticeable, as evidenced in the Figure 4.3b.

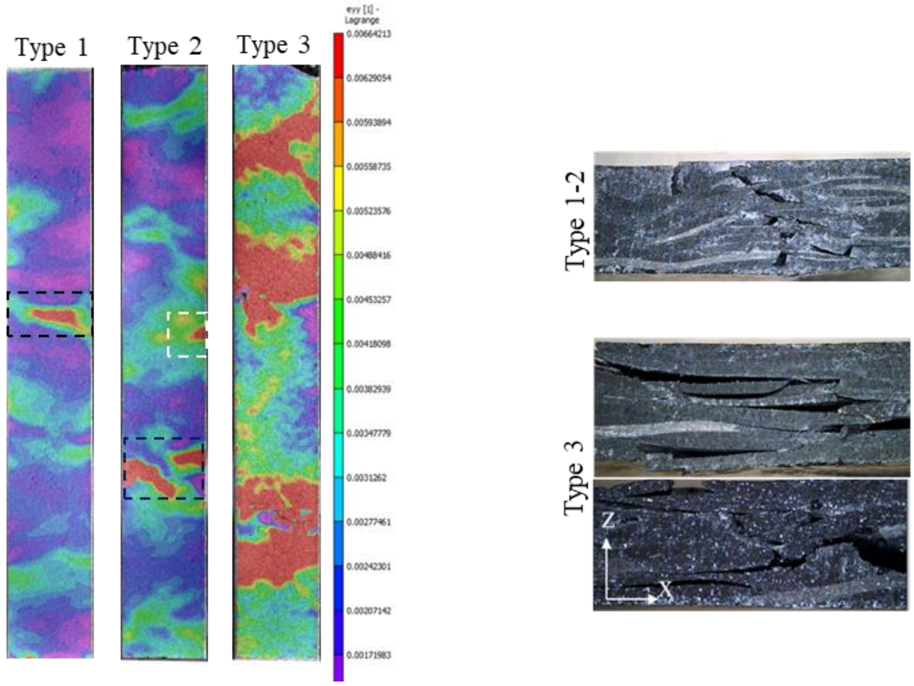

a b

Figure 4.3: Damage of the tensile specimens: a) strain map acquired with the DIC system; b) transversal fracture surfaces; the reference system is considered the same for all the three micrographs.

The crack propagation interfered with several resistance points, such as fibers oriented in different directions or interface regions. The crack-path was longer and discontinuous, generating the above-mentioned load fluctuations. The final failure generally occurred by chop debonding, due to the interlaminar shear between the chops.

Figure 4.4 shows the box plot of the tensile test results for all the tested samples. The data are normalized according to the maximum strength and Young modulus values found in the batch of the tested specimens. The specimens with the prepreg density of 204 gr/m^2 performed better than the 600 gr/m^2 ones in terms of strength. The mean strength value of the 204 gr/m^2 specimen was 17% higher than that of the 600 gr/m^2 coupons.

Strength confirmed to have high results dispersion: the normalized standard deviation was 0.203 for the 600 gr/m^2 specimens, and 0.13 for the 204 gr/m^2 specimens. Considering the stiffness, the difference in performance between the two densities is less marked: 204 gr/m^2 coupons had an 8% higher Young modulus respect to the 600 gr/m^2 specimens.

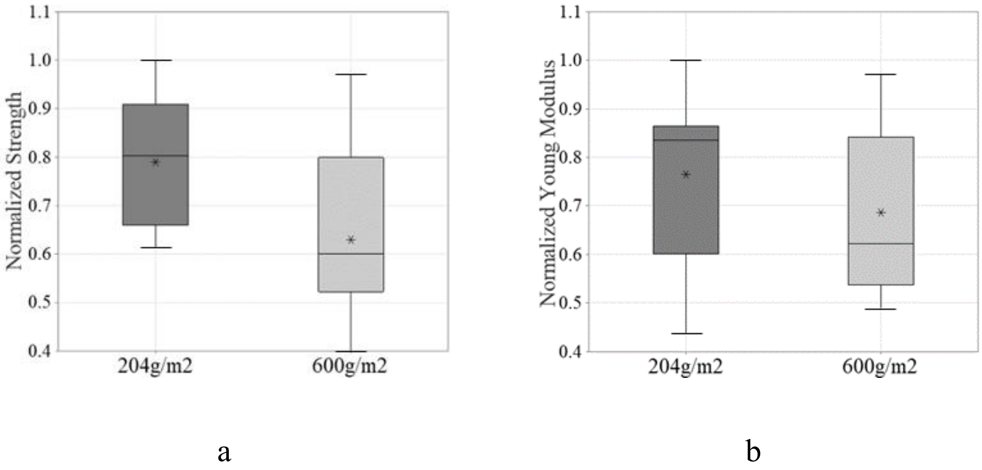

Figure 4.4: Box plot of the tensile test results: a) normalized strength as a function of the prepreg density; b) normalized Young's modulus as a function of the prepreg density

Figure 4.5 shows the bending test results of the standard specimens in terms of the force-displacement trend. The loads were normalized as a function of the maximum force value measured in the tests. To improve the clarity and readability of the graph, also in this case only a selection of results from the flexure tests are presented in the figure. These specific specimens were chosen because they provide a good representation of the overall flexural response observed in all of the specimens tested and highlight the average failure behavior across all specimens. By including only a subset of the data, the graph is easier to interpret and understand. It is worth noting that the results from other specimens and tests, while not shown in the graph, were still taken into consideration and analyzed in the overall interpretation of the data.

The high degree of the material inhomogeneity causes result dispersion in terms of stiffness, and the maximum load results are scattered too due to the different crack nucleation and propagation modes. It is possible to distinguish two different types of post-linear behavior (Figure 4.5b): type 1) propagation and delamination, and type 2) quasi-brittle failure. The discriminant between these two behaviors is the initial nucleation point of the fracture.

Considering the type 1 specimens, the crack nucleates and propagates starting from the CIR (Figure 4.5b). The primary fracture occurs in correspondence of the transition area between two chops (CIR), far from the load application section (i.e., the point that carries the higher load). Due to the discontinuity of the CIR, stresses redistribute near these zones, where the properties are matrix-dominated due to the presence of resin pockets. As soon as the crack extends along the entire CIR, moving along the y direction (Figure 4.5b), the delamination starts to propagate in the x direction (Figure 4.5b). During this stage, a step-like trend of the force occurred, similarly to what happens in a single leg bending test, where the crack is loaded in a mixed way (mode 1 and mode 2)[94,95]. Considering the type 2 fracture behaviour, fiber rupture caused the failure in proximity of the surface of the load application point. The crack propagated in the z direction, and no delamination occurred (Figure 4.5b).

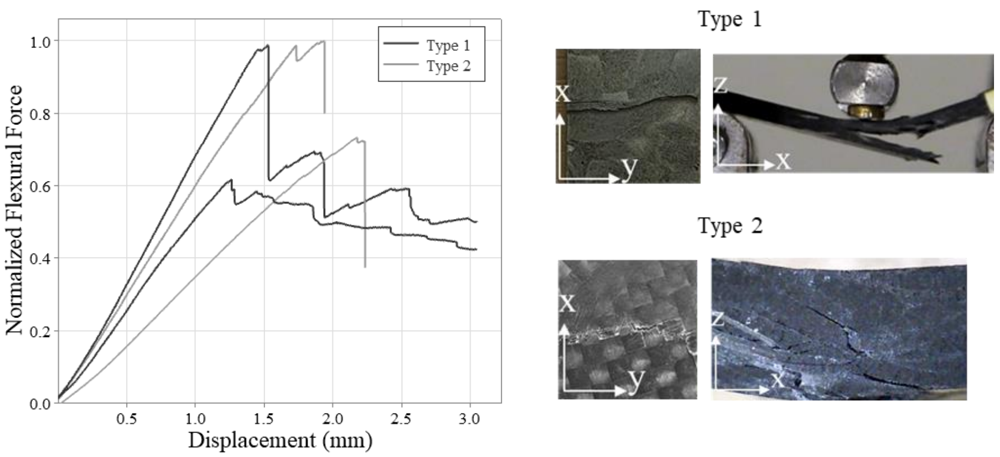

a b

Figure 4.5: Three point bending test results: a) normalized force trend vs displacement; b) fracture surfaces. Type 1 and type 2 represents the two main failure modes evidenced by the specimen tested in bending.

Figure 4.6 shows the three point bending test results for all the tested specimens. The results are normalized according to the maximum values of strength and Young modulus found in the batch of the tested specimen. Specimens with the prepreg density of 204 gr/m^2 performed better than the 600 gr/m^2 ones in terms of strength. From Figure 4.6a, it is possible to appreciate that the mean strength value of the 204 gr/m^2 specimens is the 30% higher than the 600 gr/m^2 specimens . Furthermore, for these latter specimens, the dispersion of the strength results is higher respect to that of the 204 gr/m^2 coupons. Indeed, the normalized standard deviation of the 204 gr/m^2 specimens was 0.127 against 0.135 of the 600 gr/m^2 specimens (around the 6% difference), both values are in the acceptability range. Considering the Young Modulus (Figure 4.6b), the mean value of the 204 gr/m^2 and the 600 gr/m^2 specimens are comparable. Also in this case, the result dispersion is remarkable both for 204 gr/m^2 and 600 gr/m^2 specimens (normalized standard deviation respectively 0.17 and 0.15).

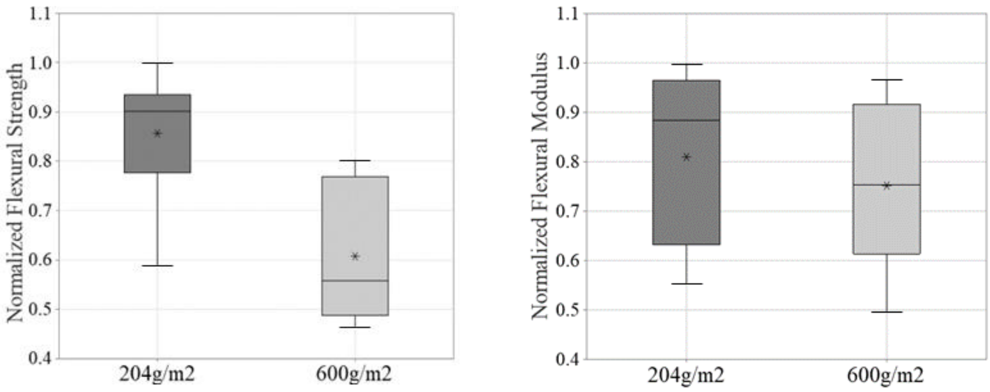

a b

Figure 4.6: Box plot of the bending test results: a) normalized strength; b) normalized Young modulus. Data are grouped according to the prepreg densities. The asterisk represents the data mean; the horizontal line represents the data median

4.1.3 Discussion

The data analyzed in the previous sections showed a dispersion in the results and in the fracture modes, even within specimens belonging to the same batch. Contrary to non-oriented short-fiber composite materials, where the randomness of the fiber orientation makes the structure globally isotropic, in this type of structure the properties strongly depend on the local conditions of the material.

The main failure modes highlighted during the tests were found to be delamination, brittle fracture of the matrix, fracture of the CIR and debonding or pull-out of the chops. During the mechanical tests, the failure generally occurred as an interaction between all these fracture modes. The material generates simultaneously several fracture precursors sites where the crack propagated. The coexistence of primary and secondary crack nucleation sites was found on several specimens tested in traction. Primary sites usually nucleated at the specimen edge where defects and weak spots concentrates due to the cutting procedure, and then propagated to the opposite edge. This propagation "through the with" is usually accompanied by a simultaneous spread "through the thickness".

The occurrence of one of the types of fracture above highlighted may seem a purely stochastic event and not predictable a priori, even if analyzing the stacking path of the chops it is possible to move towards a more deterministic approach.

The crack tends to generate and propagate towards the areas of least resistance, which in the analyzed material are represented by the CIR. Aligned interface regions along the thickness (Figure 4.7a) lead the crack to pass through them, following a shorter path. On the contrary, if the chops are stacked with a greater overlap (Figure 4.7b), the CIR are less aligned, and consequently the crack run across a longer and tortuous path, faces more resistance zones, and the global load carrying capability of the specimen increases.

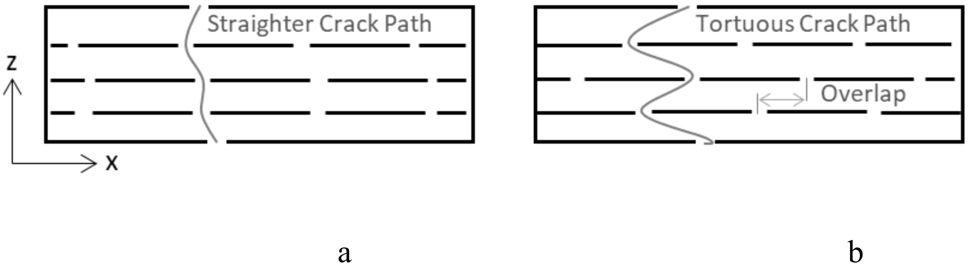

Figure 4.7. Crack propagation paths: a) transversally aligned chops; b) overlapped chops

The specimens with a prepreg density of 600 gr/m^2 showed lower strength than the specimens with a prepreg density of 204 gr/m^2. The 600 gr/m^2 and 204 gr/m^2 prepregs have a thickness respectively of 0.6 mm and 0.3 mm. Consequently, the 600 gr/m^2 specimens will have a lower number of chops along the thickness than the 204 gr/m^2 specimens. A smaller number of chops along the thickness means a lower probability for the crack to face propagation resistance spots, and consequently these specimens are characterized by a lower mechanical strength.

4.2 Influence of the chop aspect ratio

4.2.1 Material and Method

The effect of the chop dimensions on the tensile and bending performance of the material has been investigated. Two size variables will be considered: the chop aspect-ratio (AR, maximum edge length L over minimum edge length l, Figure 4.8) and the chop area (or chop size, expressed as lxL). As confirmed by previously published works[84–87,91], the dimension of the chop highly influences the material response. Therefore the possibility to find a design variable to improve the strength and stiffness of this material could be of paramount importance for the development of products with chopped structure. However, in literature it was not possible to find any trace of the effect evaluation of the chop dimension and aspect ratio carried out on specimen made up with chopped bi-directional prepreg. Furthermore, no authors isolated the effect of the chop area from the AR variable. Indeed, increasing the aspect ratio does not necessarily means increase the chop area. The Table 7 resumes the number of coupons tested and refers to both the tensile and bending samples.

The nomenclature of the specimen in the following will be as follow: Fl×L will refer to a flexural (F) tested specimen with chop size of l×L (for example F10×40); Tl×L will refer to a tension (T) tested specimen with chop size of l×L (for example T10×40).

The dimensions and aspect ratio of the chop were carefully selected to satisfy both process and structural requirements. At this early stage of technology development, the "chopping" operation is carried out manually by operators, as an automated process is still being developed. Using chop dimensions smaller than 10x20 results in dimension inaccuracies and is excessively time-consuming. Moreover, reducing the chop dimensions below 10x20 risks reducing the fiber length to an extent that can lead to an excessive degradation of the mechanical properties. On the other hand, the maximum chop size was determined based on the type of waste generated during the ply cutting stages. Specifically, the maximum chop size is limited by the minimum size of the waste produced during the ply cutting operations.

Chop size [mm]	**Aspect Ratio[mm]**	**Tested specimen**
20x20	1	8
10x20	2	8
20x40	2	8
10x40	4	8
20x80	4	8

Table 7. List of the tested chop size and aspect ratio.

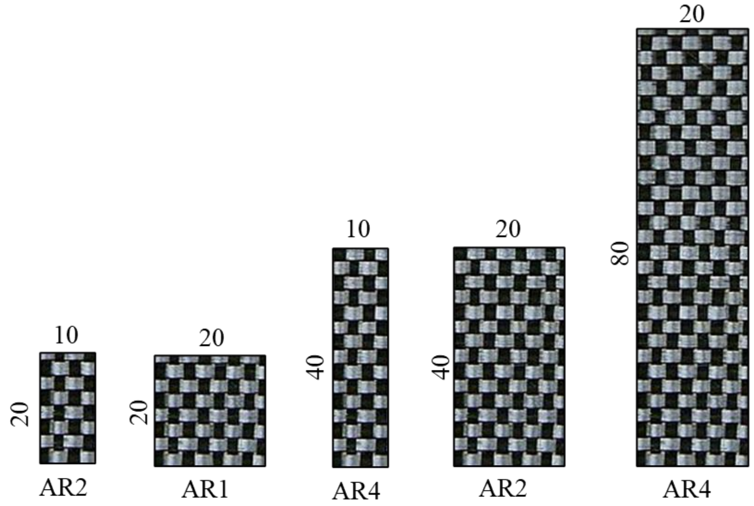

Figure 4.8. Chop sizes scheme.

The testing conditions were the same described in the section 4.1.1, except for what concerns the DIC system set-up. The transversal anisotropy of the specimen could lead to a misleading interpretation of the strain map acquired by the DIC system. Due to the discontinuous and random nature of the meso-structure, the deformations of the specimens can have different value in different location, not only on the specimen surface, but also through the thickness.

Figure 4.9. Tensile test set-up. Detail of the double camera DIC system.

In order to have a more solid evaluation of the global strain field, a double camera DIC system was used to simultaneously acquire the deformation map on both the specimen surfaces. The test set-up is shown in the Figure 4.9.

4.2.2 Results

The Figure 4.10 shows the deformation maps of the surface of the specimen T20×40 tested in traction. The strain on the two surfaces (front and rear) differs not only in the local intensity but also in the distribution. For instance, in the region 1 and region 3 of the front surface (Figure 4.10a) the strain intensifies around the CIRs. The region 2 instead, is characterized by a chop aligned to the load axis and the corresponding CIR is also aligned to the same axis. The deformation in this region is lower and confirms that the CIRs, that are aligned to the load direction, do not lead to a degradation of the properties. The same considerations can be done on the rear surface (Figure 4.10b). Here, in the region 1 and region 3 the deformations copy the local structure, with intensification in correspondence of the CIR and higher stiffness in the orthotropic regions. The region 2 instead is a portion of the specimen that presents fiber agglomeration and resin accumulation. From this portion the crack initiated and propagated until the failure. It is possible to notice that the concentration of the strain in this region is not visible from the frontal surface. Accordingly, by acquiring just one of the two surfaces of the specimen could be not enough to capture the crack evolution during the failure process or track the first nucleation spot. In correspondence of the region 2 of the rear surface, the local rigidity was around 0.5 times the global stiffness, evaluated by averaging the deformations across all the specimen area. However, although the local properties seem to dramatically differ, by comparing the mean deformations across the front and the rear surfaces, the values differ of less than 5%. Accordingly, in order to evaluate the global elastic response, it is acceptable to consider just one of the two surfaces. In all the tested specimens, the crack propagated from the surface, and not internally. Indeed, in all the test, when the audible crack and ping occurred, a crack opened in one of the two surfaces (front or rear). The failure occurs in the surface because the chops only have the shear reinforcement on one side. Accordingly, track the crack evolution and the first crack onset by the DIC is a reliable method, independently of the propagation phenomenon that occurs through the thickness.

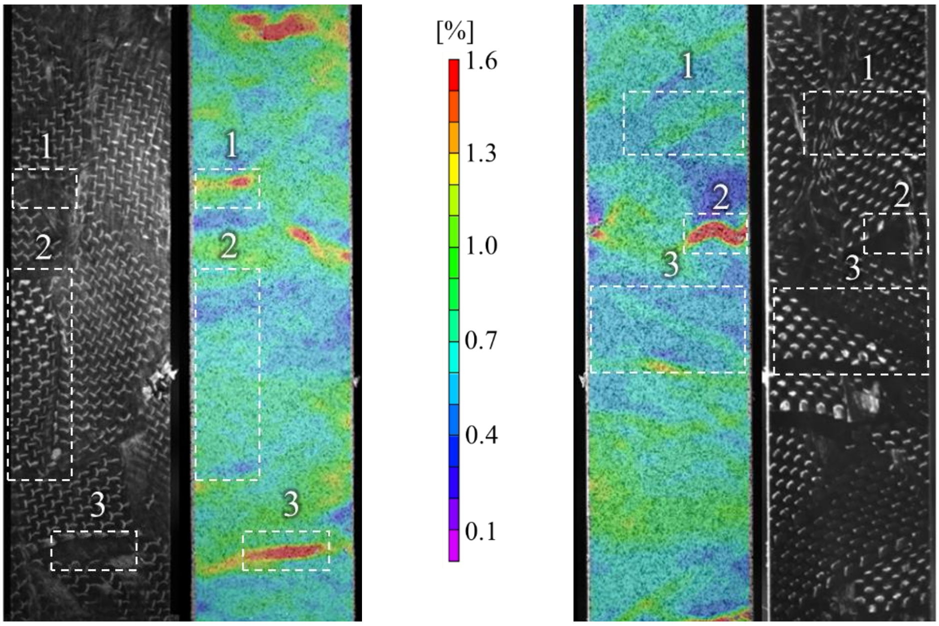

a b

Figure 4.10. Tensile specimen 20×40: a) front specimen surface and deformation map; b) rear specimen surface and deformation map.

The Figure 4.11 shows the analysis of the results of the tensile test carried out on specimens with different chop sizes and AR. The data are collected in interval plots, which shows the 95% of confidence interval around the mean of each group. The central dot represents the mean value for the specific group. It is evident that the chop size generates a bias in the material strength (Figure 4.11a). Increasing the chop size, the mean value of the strength increases as well. The increase in the strength between the worst performing configuration (T20×20) and the best performing one (T20×80) was around 68%. However, increasing from T10×20 to T20×20, there was a slight reduction in the ultimate strength, although the greater chop size that theoretically should transfer more load by shear. For this reason, data were then grouped by chop aspect ratio (Figure 4.11b). The effect of the chop AR is even more evident, and the significance of this parameter was confirmed also by the ANOVA carried out at the 95% of confidence level, which result in a *p* value equal to 0.001. The mean strength increases of around the 45% from AR1 to AR4. However, this plot can be misleading, as it does not isolate the information of the chop area. Indeed, equal chop AR (for instance 10×20 and 20×40) can have different strength value due to the different area of the chop. Different chop dimensions can be contained within the same AR category. Accordingly, the data were grouped as a function of the minimum chop length (L_{min}) and of the aspect ratio AR (Figure 4.11c). For instance, the configuration L_{min}=10 and AR=2 represents the specimen made up with the chop equal to 10×20mm. The results of the ANOVA showed that both Lmin and AR had a significant effect on the strength response, with P-values of 0.004 and 0.002, respectively. However, the interaction between these two factors was not found to be significant, with a P-value of 0.819. These results indicate that while both Lmin and AR play a role in determining the strength of the samples, the interaction between them is not a significant factor.

Let’s look at the elastic modulus results. Contrarily to what found by Feraboli et al [84], where no influence of the fiber length on the elastic properties of the material was found, from the Figure 4.11d and e it is evident that the AR has an effect on the stiffness too, even if in a lower extent than on the strength. The increase in the modulus between the worst performing configuration (20×20) and the best performing one (20×80) was around 20%. However, the ANOVA analysis did not confirm the significance of the L_{min} value on the stiffness (*p* value equal to 0.766). The dominant factor seems to be just the chop aspect ratio (*p* value equal to 0.002). Indeed, looking at the graph in Figure 4.11d its evident that keeping the AR equal to 2 and doubling the area, the mean of the stiffness decreases. Instead, for an AR=4 a doubling of the area lead to a slight increase in the stiffness. It can be concluded that the area of the sample has no effect on the stiffness, but the only dominant factor is the chop AR.

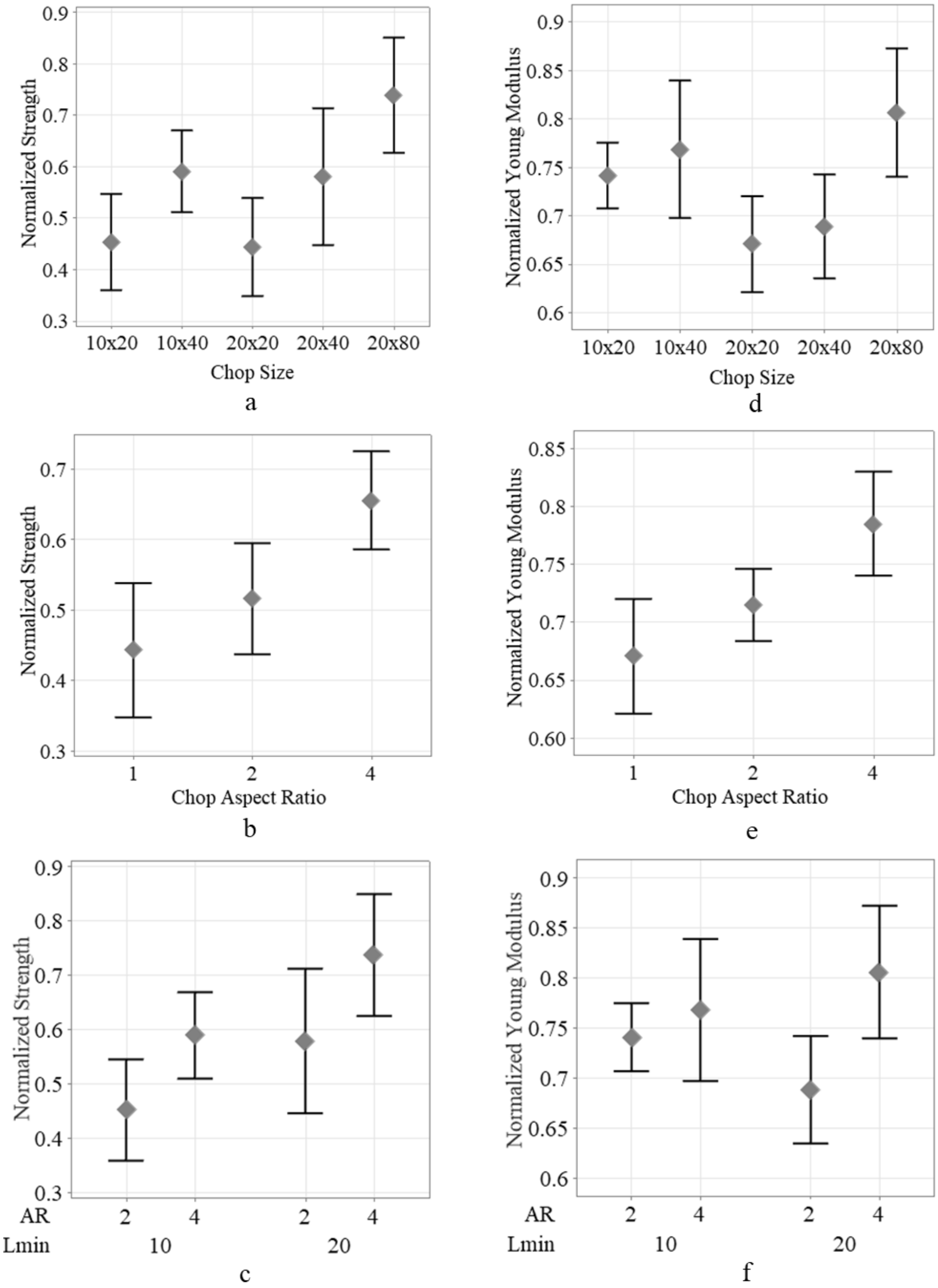

a d b e c f

Figure 4.11. Tensile tests results presented in interval plots. Individual standard deviations are used to calculate the intervals. The maximum strength and the maximum stiffness obtained in this batch of tests were used to normalize the data.

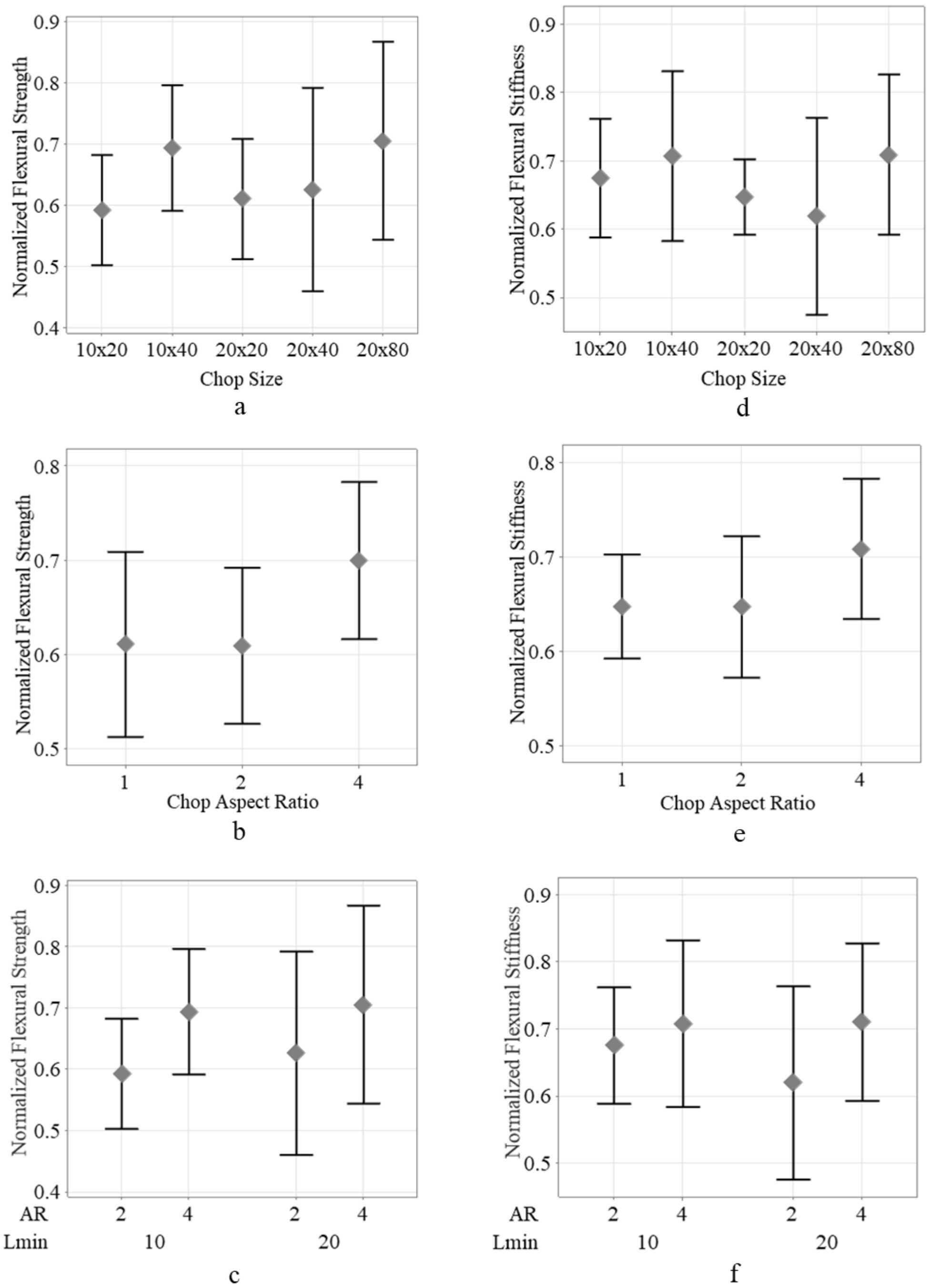

a d

b e

c f

Figure 4.12. Three point bending tests results presented in interval plots. Individual standard deviations are used to calculate the intervals. The maximum strength and the maximum stiffness obtained in this batch of tests was used to normalize the data.

The Figure 4.12 shows the interval plot of the bending tests results. In this case, the ANOVA analysis did not confirm the significance of the AR, of the L_{min} and of the chop size both on the ultimate strength and stiffness. This aspect goes in contrast with some findings in literature, where some authors found an increasing trend [84] and other a decreasing trend [85] of the strength as a function of the platelet fiber length. However, by looking at the Figure 4.12b-e, it is clear that the stiffness and strength response is not affected by an increment of the AR from 1 to 2, but it is remarkably higher passing to an AR4.

Considering the Figure 4.12a and d, the 20×80 mean values of the strength and of the stiffness are respectively the 15% and the 10% higher in comparison to those of the chop standard size 20×20. A trend of the mean values can be qualitatively appreciated. However, as the confidence intervals of the 20×20 configuration totally overlaps to the interval of the 20×80 configuration, this conclusion cannot be considered quantitatively solid as the 20×20 and 20×80 results can belong to the same population.

4.2.3 Fracture surface analysis & discussion

The fracture initiation and propagation modes encountered for each different AR were similar to the one described in the section 4.1.2. The resin rich areas, the resin pockets and the CIRs confirmed to be the crack initiation sites. The Figure 4.13 shows the fracture surface of the specimen T20×20 (a-b) and T20×80 (c-d). Note that only 2 fracture surfaces are here described, as these are representative of the two main failure modes found for all the other chop sizes. For the configuration with smaller chop size, the main failure mode was chop pull-out and delamination (Figure 4.13a). The crack initially nucleates on the surface, in correspondence of the CIR (Figure 4.13b) and then transversally propagated between the plies following the least resistance path (Figure 4.13a). It is possible to notice that no fiber rupture occurred, and an inter-ply propagation of the crack occurred.

Chop debonding and delamination were the main failure mode of the specimens T10×20, T20×20, T10×40. This is due to the lower shear force transferred between the chops respect to the 20×40 or 20×80 configuration. Although in these last two configurations the chops are more prone to pull out too, we found some specimens that failed for fiber rupture (Figure 4.13c-d).

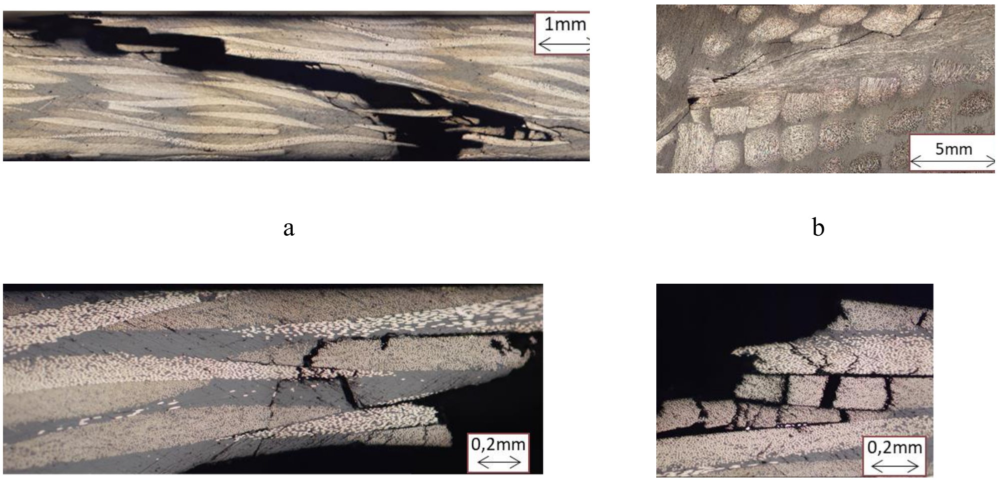

a b

c d

Figure 4.13. Fracture micrography after the tensile tests: a) cross-section of the 20×20 specimen; b) surface view of the 20×20 specimen with a detail of the CIR fracture; c-d) cross-sectional micrography of the 20×80 specimen.

Here, the crack initiated within the chop ply and then propagated through the thickness. In the Figure 4.14c, the fracture has a stepwise path, and several crack modes are noticeable, such as delamination between the ply, fiber rupture and matrix cracking. Here, the crack had a heterogeneous propagation, as it passes through the tow and then through the resin pocket agglomeration.

The high dispersion of the bending results is due to the localization of the maximum load that is induced in this type of test. For all the specimens, the fracture occurred for tension load (i.e. in the lower surface), but not always in correspondence of the point of load application. Indeed, although the maximum tensile stress is localized in a single point, the weakest spot may be some millimeter away from that point, and for this reason the crack starts not exactly in the region where the load is applied. The Figure 4.14c shows the cross-thickness micrography of the F20×20 specimen loaded in bending. The crack initiation point was found to be 5 mm on the left respect to the load application point, in correspondence of a chop interface region localized in the bottom surface of the specimen (evidenced in the figure by the white box). From this point, the crack propagated through the plies until it reached the top surface of the specimen.

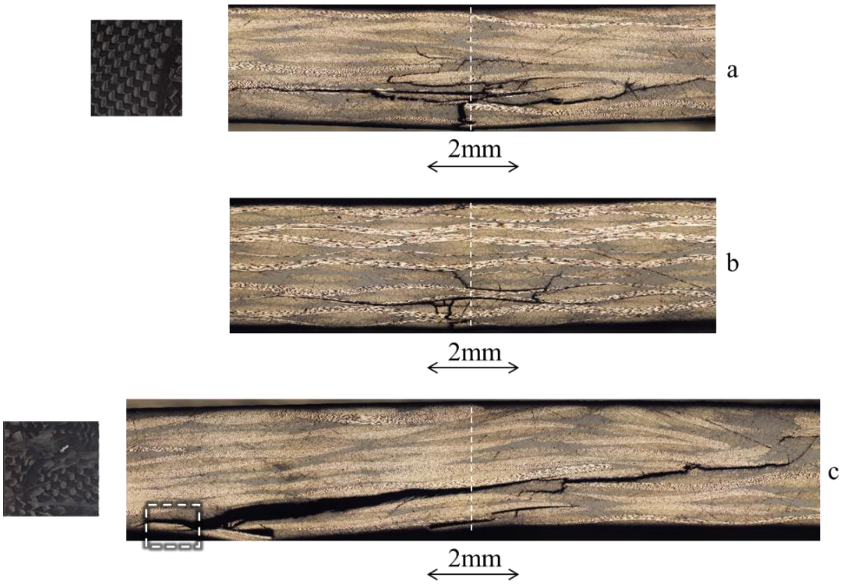

Figure 4.14: cross-sectional micrography of the 3 point bending specimens: a) 20×80 specimen; on the left a detail of the bottom surface in correspondance of the loading pin; b) continuous fiber specimen; c) 20×20 specimen; on the left a detail of the bottom surface in correspondance of the loading pin. The white dashed line indicates the axis of application of the load.

The propagation has a regular and linear pattern, and it is mainly characterized by delamination. After the peak, the load did not drop sharply, but the drop was characterized by a scattered trend related to the propagation of the crack (Figure 4.15). The Figure 4.14a shows instead the micrography of a F20×80 specimen. In this case, the coupon presented a chop aligned with the specimen axis that covered all the bottom surface. No weak spots were visually notable on this surface. The crack location in this case was in correspondence of the bottom surface, under the load application point. The initiation was due to chop failure. The crack propagated through the chops, causing fiber rupture for some tenth of millimeter through the thickness, and then it propagated horizontally in both direction through the plies, causing delamination. However, the crack did not propagate across all the specimen thickness, but its propagation was stopped by several resistance spot. This crack pattern had a similar fashion to the one that occurs in a continuous fiber laminate (Figure 4.14b). Furthermore, the maximum load and the stiffness of this F20×80 specimen are comparable to the continuous fiber coupons (Figure 4.15). The F20×80 specimen reaches a slightly lower maximum load respect to the continuous fiber one (10% lower) and near the ultimate point the load has a scatter trend that looks like a plateau, and it is related to the crack propagation. The continuous specimen instead, has a sharp drop in load associable to a catastrophic event.

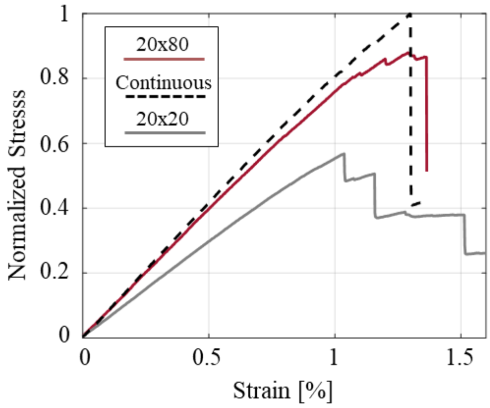

Figure 4.15. Normalized flexural stress-strain trend of the F20×80, F20×20 and continuous fiber specimens.

However, not all the F20×80 specimens had a similar trend. Some of them had an ultimate stress even lower than the average F20×20 ones. This is due to the stochastic presence and localization of interface regions or weak spots under the point of load application. The localization of the load that occurs during the bending tests together with the stochastic nature of the material lead the bending results to have a great variability and dispersion. The mean standard deviation of all the group size for the bending specimens is around 0.15 against the 0.12 of the tensile specimens. Indeed, contrarily to what happens for the bending, in traction all the point of a cross section are subjected to an equal load. Accordingly, the weak spot probability distribution along all the cross section is more uniform, and thus in all cross section there could be an equally loaded potential crack nucleation point that can generate the fracture.

4.3 Influence of the plate anisotropy

The degree of the in-plane anisotropy of the configuration CP25 and CP100 was verified by cutting specimen in different plate location and orientation. Two square plates (370×370mm) with an average thickness of 2.8mm were produced with the same process conditions described in the section 3.1.1 (configuration CP25) and 3.1.3 (configuration CP100). The cutting layout is shown in Figure 4.16. The specimens 3-7 (0° specimens) were cut to verify a possible bias of the material properties according to the distance from the center of the plate. Indeed, as demonstrated in the section 3.1.3, the porosity increases in the radial direction as the air bubbles are transported from the center of the plate to the edges.

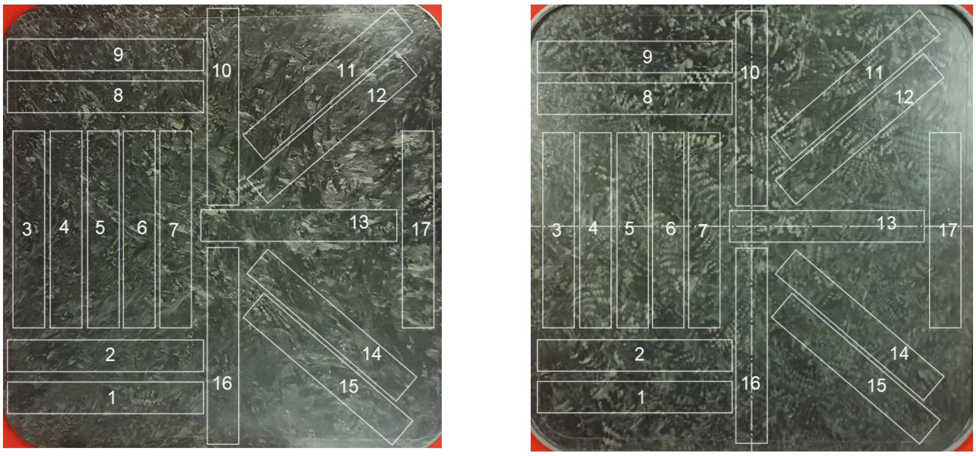

a

b

Figure 4.16. Cut layout for the CP25 plate (a) and CP100 plate (b).

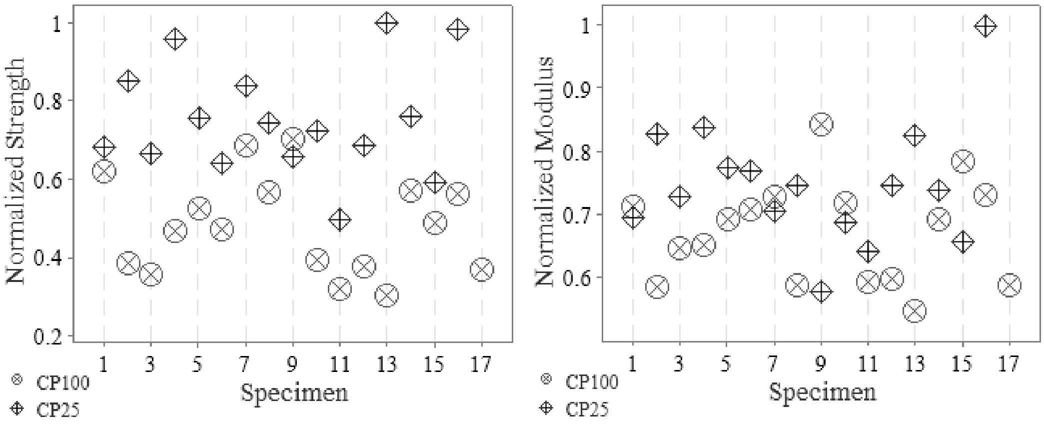

a

b

Figure 4.17. Tensile test results: a) normalized strength and b) normalized Young modulus as a function of the specimen number and cut location. The data were normalized according to the maximum stress and strength observed within both the CP25 and CP100 specimen batch.

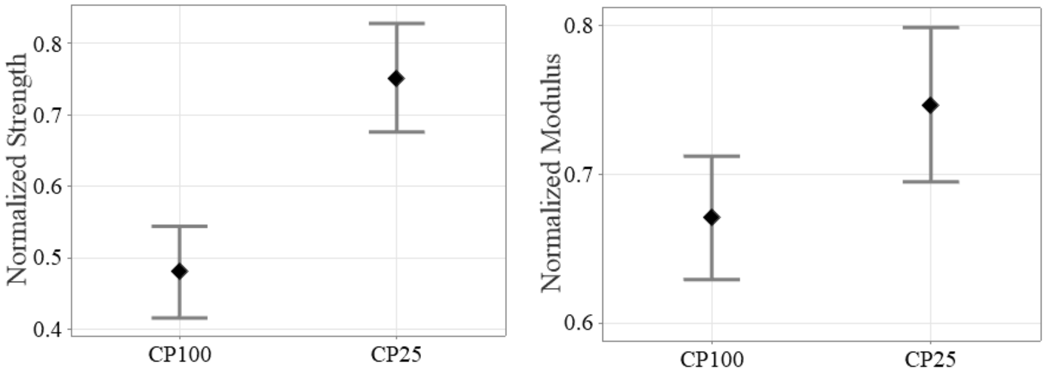

a b

Figure 4.18. Interval plot of the normalized strength (a) and normalized Young modulus (b) as a function of the compression molding configuration.

The specimens 11,12,14,15 were cut at 45° respect to the plate vertical axis and the specimens 1,2,8,9,13 at 90°.

The results of the tensile test are shown in Figure 4.17. Contrarily to the findings of Feraboli et al [84], no bias was found in the ultimate strength according to the specimen orientation or location on the plate for both the configurations. The data are highly scattered even if the standard deviation for the CP25 specimens was slightly higher than for the CP100 ones (0.14 against 0.12). This aspect could be related to a slight anisotropy of the CP25 configuration due to the flow-induced phenomenon. In average, the ultimate strength of the CP25 specimens was higher of the 37% respect to the CP100 specimens (Figure 4.18).

The Young Modulus of the specimens for both the configurations was evaluated by averaging the deformations across all the specimen surface, acquired by the DIC system. The elastic properties are less affected by the flow-induced phenomenon and the difference between the CP25 and CP100 configurations is less marked: the CP25 specimen had an average stiffness 10% lower than the CP100 specimen. Although the difference in the average stiffness is not large, the deformation distribution across the specimen surface is highly influenced by the flow properties. The Figure 4.19 shows the deformation map of the specimens 11 CP100 (Figure 4.19a), 11 CP25 (Figure 4.19b), 13 CP100 (Figure 4.19c) and 13 CP25 (Figure 4.19d). The maps refer to an applied load of 4.5kN (11 CP25 and CP100) and 5.5kN (13 CP25 and 100). The specimens CP100 tends to intensify the strain in specific weak spots (usually CIRs), the CP25 instead presents more homogeneous deformations across the surface. This aspect was also confirmed by the strain standard deviation difference between the CP100 and CP25 specimens. The specimen 13 CP100 and 13 CP25 had a strain standard deviation respectively of 0.35% and 0.11%. The flow induced phenomenon in the CP25 configuration reduces the heterogeneity of the structure and the effect of the major stress concentration spots.

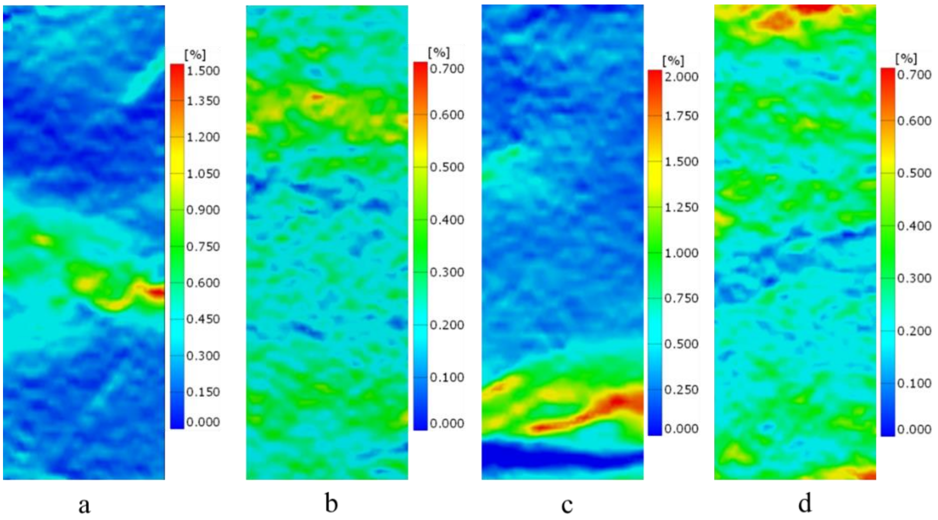

Figure 4.19. Deformation map of the a) CP100 specimen 11; b) CP25 specimen 11; c) CP100 specimen 13; d) CP25 specimen 13. The color bar indicates the strain along the load direction

The chops redistribution along the flow direction homogenizes the meso-structure and limits the formation of the CIR which are the most compliant part of the structure. Although the average global deformation between the two configurations has a comparable value, the maximum strain in the strain concentration spot for the CP25 configuration is around 2-2.3 times higher than the CP100 configuration.

4.4 Conclusion and Considerations

An experimental test campaign was carried out in order to analyze the mechanical performance of the chopped material and study the effect of the process variables and of the initial material constituents on the fracture mechanics, on the strength and stiffness response. The ultimate material properties were evaluated, and one of the first aspect that came out is the high scatter and dispersion of the results. Indeed, the mechanical properties are strongly influenced by the meso-scale structure, where the major stress concentrations stemming from the discontinuities influences the crack initiation and propagation. The stress concentrations spots are usually generated by the interface regions between the chops (CIR), resin rich areas or chops agglomerate that are randomly distributed across all the plate area. The reduction of these discontinuities can be achieved by optimizing the process conditions (i.e. allow for fiber redistribution through a high flow compression molding configuration, as occurred in the CP25 configuration). Indeed, the CP25 specimens performed better than the CP100 ones. It should be pointed out that, as demonstrated in the section 3.1.1, this fiber homogenization and redistribution in the CP25 configuration only occurs on the plate boundary layers, while in the core layer the chops of the CP25 configuration are distributed as the CP100 ones, with the formation of CIRs and chop agglomerates. However, in this kind of structure the fracture always initiates on the specimen surface, as here there is no chop shear reinforcement, and the stresses concentrates more. It is evident thus that the fiber distribution in the boundary layer has an important effect on the material response, as the CP25 configurations performed better than the CP100 ones. The ultimate properties are influenced also by the meso-constituents geometry and structure. Indeed, the meso-scale stress transfer between the chops depends on the morphology of the composite meso-structures. As the load is mainly transferred by shear between the chops, it was confirmed that by increasing the chop area or the chop aspect ratio, the ultimate properties increase as well. However, the material response strongly depends on the kind of the load the structure is subjected to, and also on its localization. Punctual loads (such that generated by the three-point bending test) accentuates the effect of the discontinuities and leads to higher result dispersion. The meso-scale interactions between the chops determine the dominant factors that control the progressive damage and the macroscopic strength of the structure. Prior to the failure, several damage nucleation sites occurred, generally at chop interface. Chop delamination, brittle fracture of the matrix, chop pullout and CIR fracture are the primary failure modes. Contrarily to what happen on continuous composite structures, where the crack initiation is often defined as failure, the first crack nucleation site is not always the one that generates the ultimate fracture, as the crack path depends on the presence of resistance spots or weak regions. The structure doesn’t collapse catastrophically, and the ultimate failure depends on the crack path length and tortuosity. This gives to the structure a more progressive and controllable failure mode even if the load that onset the first crack from which the failure propagates is almost unpredictable, due to the stochastic nature of the structure. The experimental tests have shown that crack and tip sounds are often heard before the crack propagation and failure stages. Accordingly, acoustic emission recognition methodologies could be applied to detect and monitor the generation of the crack nucleation sites. By using acoustic sound techniques, as reported in [19], it may be possible to determine the location, the size, the severity and the rate of crack growth (i.e. the propagation) by analyzing the sound amplitude, frequency and duration. According to this information, it could be possible to predict the damage intensity and potentially correlate it to the residual life of the component.

Although the properties of the material have been normalized for confidentiality reasons, it is relevant to compare the mechanical behavior of the chopped carbon fiber specimens with that of their continuous fiber counterparts. Considering the mean values obtained from all the mechanical tests carried out in the experimental campaign, which include specimens with different chop size or aspect ratio, initial mold filling and prepreg surface density, it was found that the chopped specimen exhibit on average the 27% of the tensile strength and the 57% of the tensile stiffness of their continuous fiber counterparts. Considering the dispersion interval, the lowest and highest range values for strength are 21% and 35%, respectively, while the lowest and highest values for stiffness are 52% and 62%, respectively. The identified range of variation in strength and stiffness can be attributed to different manufacturing conditions and mesostructures of the specimens.

Regarding the flexural properties, the results indicate that chopped carbon fiber specimens exhibit, on average, 63% of the strength and 66% of the stiffness of their continuous fiber counterparts. The lowest and highest values of the interval for the strength are 59% and 68%, respectively, while the lowest and highest values for stiffness are 63% and 70%, respectively.

These average properties result to be comparable, if not superior, to those of commonly used structural aluminum (Al6061) and are suitable for use in light structural applications.

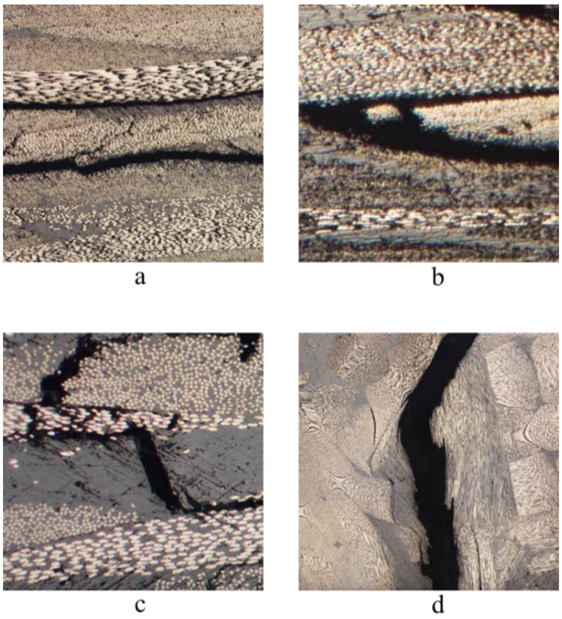

Figure 4.20. Classification of the fracture surfaces: a) delamination; b) chop pull-out; c) matrix fracture; d) interface region crack propagation.

5 Process Simulation

The anisotropic distribution of the constituents of a DFC structure strongly depends on the initial process condition and on the flow phenomenon induced by the stamping operation. The prediction of the final structure and of the distribution of the constituents through numerical simulations is still an open topic that can be faced through statistical approaches and constitutive models. The techniques proposed in the literature are mostly aimed to predict the local properties variability of such structures and capture the stochastic constituent distribution that induces a scattered ultimate response. Accordingly, predictive simulations are required to understand the development of the meso-structural features and aid in the design process of both the material system and the molding process.

The numerical modelling techniques proposed in literature can be categorized into three main groups: micro (fiber scale), meso (chop scale) and macro (molded-geometry scale)[93]. It is evident that simulating the material in the micro scale would require an out of order computational effort. Viceversa, a macro approach loses the microstructure information with limitations in the prediction of the property variability. With the recent advent of high-performance computing, the complex material behaviors can be predicted based on the microstructure Representative Volume Element (RVE) approach and then homogenized across all the considered domains. Accordingly, the material properties are predicted based on statistically equivalent microstructure reconstructions[96,97]. The RVE is defined as a representative volume large enough to contain enough micro-features so that the RVE properties are considered as spatially invariant[98,99]. However, in DFCs this can be not totally true, as the constituent distribution is stochastic across all the part and form a random repeating pattern of local maxima and minima across all the specimen surfaces that strongly depends on the process-induced phenomenon. Feraboli et al [100] proposed a methodology to capture this random pattern by means of a Random RVE. They implemented a randomization process that assign the elastic properties to the RVE based on random stochastic considerations. A similar approach was implemented by Kravchenko et al [101]. They noted that the variable distribution of the overlaps between the chops (CIR) translate into the variability of the effective tensile properties of the DFCs. This complex CIR distribution does not allow the definition of a periodic RVE, and therefore they proposed a non-periodic RVE for the homogenization of the material properties. A deterministic approach based on physical observation was instead proposed by Nachtane et al [102] they defined a multiscale model to study the influence of the microstructure on the mechanical properties. They built a numerical multiscale model based on morphological characteristics obtained through optical measurements and Micro-CT analysis. The numerical model integrates the chop arrangement distribution, the defects, and the rich matrix areas, based on microstructural observations. They used a modified random sequential adsorption algorithm to append consecutive fibers on the RVE. Other authors proposed stochastic finite element techniques to predict the properties variability of the DFCs without any homogenization technique, but by simply assigning to the macro model a local fiber orientation based on stochastic algorithms. Selezneva et al [103] discretized the macro model into chops by using partitions, and each partition contained the information about the local layup and fiber orientation. Cutting et al [104] implemented the material card “Enhanced composite damage” (MAT54) to simulate in LS-Dyna environment the flexural response of a DFC material. They wrote a chop generation code that transferred the orientation information into an existing baseline FE model. The properties of the chops were used as input into the MAT54 card, and to each element an in-plane orientation angle was assigned to represent the platelet fiber direction. Lim et al [105] simulated the damage initiation and propagation of SMC material. They built a RVE based on image analysis. The model of the constituents is based on statistical bundle or chop dispersion according to the manufacturing-dependent parameters that are used to match the targeted statistical distribution of the fiber orientation and FVF. In all the proposed model in the literature review the generation of the RVE constituents is based on physical observation carried out on molded samples. However, the process itself is intrinsically stochastic and simulation is the appropriate approach to capture the flow-induced material anisotropy. Sommer et al [27] proposed a flow-induced fiber orientation distribution predicted using an anisotropic viscous constitutive model implemented in a nonlinear, explicit finite element solver. Each chop that composes the initial charge is discretized into “voxels” with the same orientation and the same thickness. The SPH (Smoothed Particle Hydrodynamics) method is used to discretize the charge domain and simulate the reorientation and redistribution of the chops during the compression molding process. Continuum damage mechanics and a cohesive interfacial behavior were then used to perform the progressive failure analysis. However, as demonstrated in the previous sections, the initial charge condition and orientation state strongly affect the flow-induced phenomena and the final part structure. Accordingly, Favaloro et al [28] accounted for the initial orientation state by using the fiber orientation information captured by a CT-scan performed on a pre-consolidated charge of thermoplastic material. They also used the SPH method and a user subroutine to set and track the fiber orientation during the compression molding simulation. However, the direct molding simulation based on a Lagrangian description of the chop orientation by the SPH method could be time demanding. Indeed, the setting of the rheological and kinetic equations of the material by means of a specific VUMAT subroutine, could be not a flexible, and easily scalable approach. Several authors proposed the simulation of the compression molding process through commercial flow-based software such as Moldflow[106] and Moldex3D [107]. Song et al [108] simulated the molding of a bulk charge by accounting for the initial fiber orientation. Computer tomography is used to scan the bulk charge and estimate the initial orientation. They developed a mapping algorithm in MATLAB to estimate the fiber orientation and then the orientation information is transferred to Moldex3D. They confirmed that the initial charge condition highly influences the finished part properties.

The complex models such as the constitutive models based on sample microstructure observation, or the flow induced Lagrangian SPH method could have some drawbacks in industrial application, where the model set-up must be direct, rapid and flexible. Accordingly, the aim of the proposed work is to implement a methodology for the simulation of the compression molding process of a charge made up of chopped prepreg, that must be easily scalable, and the results must predict the flow-induced phenomenon during the process as well as estimate the final properties and fiber orientation distribution of the molded component.

In this work, the simulations were carried out by integrating the commercial softwares Moldex3D, Digimat, Ls-Dyna and Matlab. A flow chart of the steps is shown in Figure 5.1.

The process model was fully defined in the Moldex3D environment, where the part mesh was generated as well as the charge geometry and material properties. As the Moldex3D environment does not allow to user-define the initial fiber orientation within the charge, a Matlab script was written to discretize the charge and generate the initial orientation conditions. The charge was then re-imported in Moldex 3D and the flow-simulation was run. The Digimat multiscale software was used to map the fiber orientation distribution of the molded plate process mesh, generate the microstructure and the material card. This information was then transferred in the structural mesh and used as input in the Ls-Dyna model to simulate standard tensile tests and predict the global response of the material.

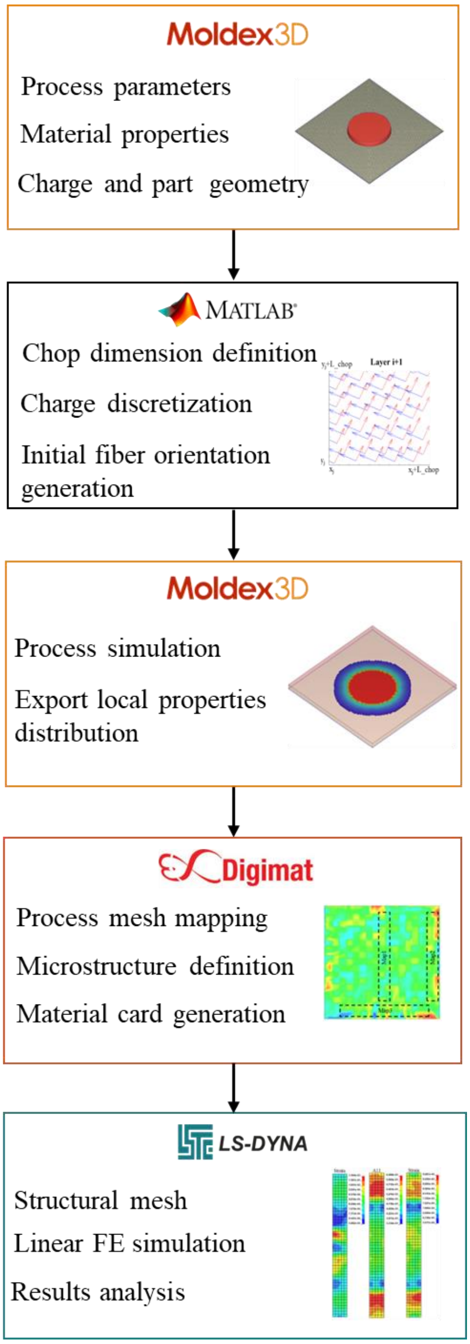

Figure 5.1. Simulation process flow chart.

5.1 Process Simulation set-up

5.1.1 Moldex3D: Theory background

Moldex3D is a commercial software specialized in molding process simulations [109]. Initially it was developed as software for the simulation of Injection Molding processes. Recent developments allow to simulate Compression molding, Resin Transfer Molding processes, Compression-Injection molding etc. It is widely used in the plastics industry and recently also in the field of composite materials. Moldex3D integrates a flow-based simulation solver, which uses the Eulerian approach to solve problems. This approach is based on the finite volume method, which involves solving equations on small volumes, or "elements," within a mesh. The solution is then determined by applying specific boundary conditions to the mesh. These boundary conditions can include information such as the pressure, temperature, and chemical composition of the fluid at the edges of the mesh . To manage the motion of rigid particles in a viscous flow such as fibers dispersed in a liquid matrix, Moldex3D uses mathematical models based on the combination of the Jeffery hydrodynamic model [110], with the Folgar-Tucker rotational diffusion model [111]. This mathematical model is defined as the iARD-RPR model (improved anisotropic rotary diffusion-retardant principal rate). The fiber orientation is described using an orientation distribution function $\psi(\mathbf{p})$. The orientation of a single fiber can be indeed described by the unitary vector ***p*** (boldface will be used to express a vector quantity) directed along the fiber axis. Its orientation within a three-dimensional space can be described as follow (Figure 5.2):

$$\begin{aligned} p1 &= sin\vartheta\ cos\phi \\ p2 &= sin\vartheta\ sin\phi \\ p3 &= cos\vartheta \end{aligned} \qquad 5.1$$

However, as in a composite material there are thousands of fibers per cubic centimeter, it is not convenient to describe the orientation state of each single fiber. Accordingly, a statistical approach that accounts for the probability of a fiber to have a certain orientation is more efficient and can be described through the orientation distribution probability function $\psi(\vartheta, \phi)$. This function gives an indication of the orientation state of the fiber in a certain region of the composite material.

A more effective description of the orientation state was introduced by Advani and Tucker [111], which proposed a second order tensor for the representation of the orientation distribution:

$$\boldsymbol{a}_{ij} = \langle p_i \otimes p_j \rangle = \int \psi(\mathbf{p})\, p_i p_j d\boldsymbol{p} \qquad 5.2$$

Accordingly, the unitary vector is averaged over a selected volume to describe the average orientation condition in a certain region. The vector has a unitary trace:

$$a_{11} + a_{22} + a_{33} = 1 \qquad 5.3$$

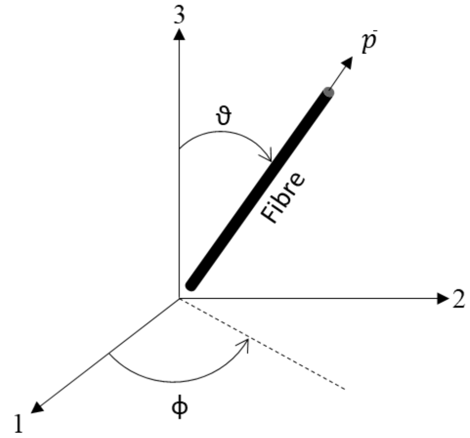

Figure 5.2. Representation of the fiber orientation in a three-dimensional space. The vector $\boldsymbol{p}$ indicates the fiber direction.

The eigenvectors of $\boldsymbol{a}_{ij}$ represents the principal orientation directions, while the eigenvalues represent the fiber distribution along the three principal directions [112]. Accordingly, a high probability of fiber alignment in a specific principal direction (for instance a_{11}) is indicated by an eigenvalue close to 1. Conversely, a value of the three eigenvalues close to 1/3 means that the fibers are randomly oriented in the space.

5.1.2 Moldex3D: Simulation set-up

The process simulations have been performed in the compression molding module of the Moldex3D software. The educational licenses for the compression molding module have been kindly provided by Ing. Giorgio Nava of Moldex Italia.

This section presents the methodology employed to simulate the production process of a plate using the Moldex3D software. The two configurations described in the experimental tests, namely CP25 (high flow) and CP100 (high flow), are simulated, in order to have a numerical-experimental comparison of the influence of the initial charge condition on the final structure of the component.

In the first step, the software requires to set a “compression zone”, i.e., the control volume where the flow stages are calculated and where it is expecting to occur significant change in the fluid properties. The compression zone created had a dimension equal to 350×350×17 mm, and it was meshed by means of the dedicated Moldex3D meshing tool with 40 layers of solid prism elements. Then, the model of the final part has to be built. The part is intended as the representation of the object to be molded and is located within the compression zone. In our case, the final part is a square plate with the dimension of 350×350×2.5mm. Five layers of a hybrid Boundary Layer Mesh (BLM) were used for the discretization of the molded part. This is a sandwich-like mesh, where the skins are discretized by prismatic elements and the core by tetrahedral elements. The BLM mesh allows to accurately simulate the viscous phenomena that dominate the flow boundary layer.

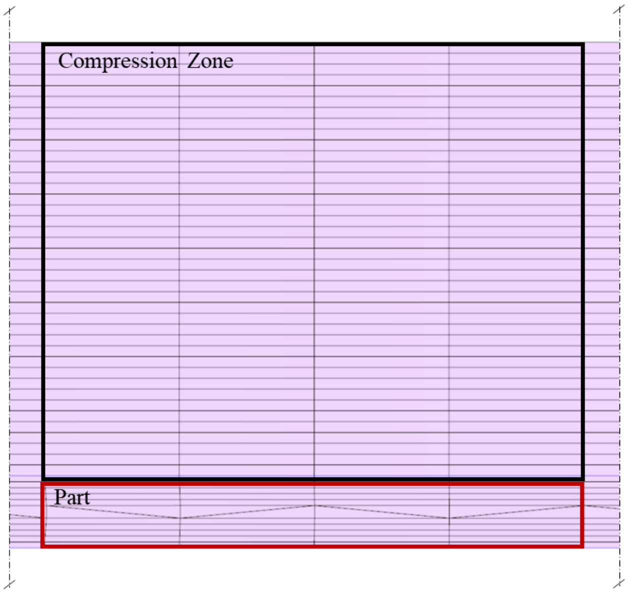

Figure 5.3. Discretization of the compression zone (black box) and of the part (red box). The part was meshed with the BLM mesh option.

The charge geometry was imported in the Moldex3D environment as a STEP file. In order to perform flow and fiber orientation analysis, the two different configurations of the initial charge geometry were reproduced (CP25 and CP100). The CP25 charge was modeled as a cut spherical cup shape (Figure 5.4a), with a lower diameter of 148mm, an upper diameter of 143mm and a thickness of 20mm aiming to capture the higher concentration of chops near the center of the charge. The CP100 charge was modeled as a parallelepiped with a thickness of 3.6mm. Note that in this latter case the initial mold surface filling is slightly lower than 100%. Indeed, the aim was to reproduce the higher concentration of chops nearby the center of the tool, as usually during the chop disposal procedure, at the edge of the mold there is a lower chop concentration.

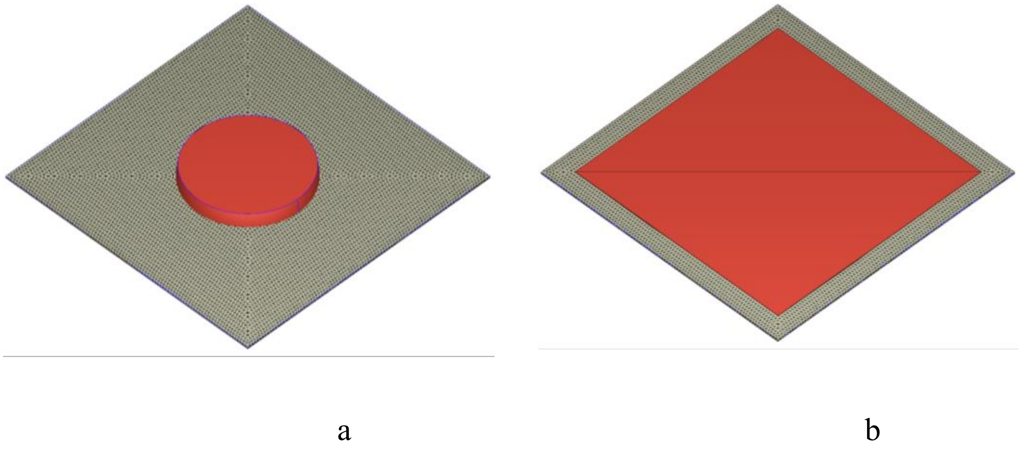

Figure 5.4. Two charge configurations: a) CP25 (high flow); b) CP100 (low flow).

The material properties have been set based on a CAE model available in the Moldex3D material library. The rheological properties of the prepreg and the cure kinetics of the resin were approximated by the evaluation carried out in the chapter 2. As PVT properties of the charge were not characterized, the ones proposed in the Moldex3D material library for an epoxy resin system were used. The viscosity was described by the Castro-Macosko model, the cure kinetics by the combined Kamal-Sourour model [48,70], and the PVT properties by the Tait-C model [113]. Thermal conductivity and heat capacity were kept constant. The physical-mechanical properties of the fibers were obtained from the prepreg datasheets, or, if not available, obtained from the Moldex3D material library, as are summarized in the Table 7.

The Mori-Tanaka micromechanics model has been set and the improved anisotropic rotary diffusion (iARD) technique was chosen for the prediction of fiber orientation. The iARD model needs three parameters to be set: the fiber-fiber interaction for isotropic diffusion (Ci), the fiber-matrix interaction for anisotropic diffusion (Cm) and the RPR model alpha factor.

Matrix (Epoxy resin)		
Density	(kg/m^3)	1200
Poisson Ratio	(-)	0.3
E	(GPa)	3.2
CLTE*	(1/K)	$3.2e^{-7}$
Reinforcement (Carbon Fiber)		
Weight Percentage	(%)	54
Density	(kg/m^3)	1800
Poisson Ratio	(-)	0.2
E1	(GPa)	240
E2	(GPa)	240
G12	(GPa)	22
CLTE*	(1/K)	$1e^{-5}$
Length/Diameter	(-)	3333
Interaction Coefficient	(-)	0.01
Fiber Diameter	(µm)	6
Friction Index*	(-)	3

Table 7. Material model physical parameters. Values marked with the asterisk have been taken the Moldex3D Material Library.

These three parameters have been chosen according to the value suggested by Moldex3D support channel for long fiber composites: they were respectively set equal to 0.01, 1, and 0.1.

The compression time was set to 10 seconds, with a mold closure speed of 10mm/s. A pre-heating time of 5 second was input, and the initial mold temperature was set at 150°C, in accordance with the experimental molding executed. Additionally, the cooling parameters were set: the mold-open time and the air temperature were set respectively at 5 seconds and 25°C. A maximum compression force of 9800kN was set and no initial cure conversion of the resin was chosen.

5.1.3 Initial fiber orientation: MATLAB Script

The final meso-structure of the component depends not only on the initial charge geometry and position, but also on its local fiber orientation that could induce flow and fiber rearrangement anisotropy. For an appropriate prediction of the fiber orientation in the molded part, it is necessary to set-up a reliable description of the initial orientation state within the charge. It was not possible to evaluate in a deterministic way the initial orientation state of the chops. This is due to the fact that the charge is not pre-consolidated, and the chops are randomly arranged on the mold. As a result, there are handling challenges in preserving the fiber orientation while taking the charge, scanning it using micro-CT, and reintroducing it into the mold without altering the chops orientation. Accordingly, a qualitative approach was implemented, with the aim of reproduce the initial local orthotropic fiber structure and global stochastic chop orientation within the initial charge.

Indeed, the basic chop constituent are plain wave braided fibers that forms an orthotropic structure. Accordingly, each chop represents a subdomain of the charge where the fibers are locally orthotropic oriented. Each subdomain is therefore capable of interacting with the surrounding ones according to its initial state. Globally, however, each chop is randomly oriented. It is therefore necessary to subdivide the problem of the initial orientation of the fibers on two scales: chop level, in which the fibers are oriented in an orthotropic way, and the charge level, in which the chops are randomly oriented. This problem cannot be addressed directly into the Moldex3D environment, which allows to set the initial fiber orientation only as random, planar random and manual. The manual setting allows to choose a vector that represent the global orientation, and all the fibers within the charge are supposed to be oriented in the same direction of the pre-set vector. Considering instead a random orientation, all the fibers are randomly oriented within the charge domain. However, this set-up is misleading in our case, as the orthotropic information of the chop would be lost.

The information of the charge shape, dimension, position, and fiber orientation are contained in an ASCII file with .cmbc extension, generated by the Moldex3D software once created the charge geometry (Figure 5.5). The data are organized in a matrix, in which each line represents an element contained within the charge mesh, specifies the coordinates of the element center in the global reference system, and the orientation of the vector representing the fiber associated with that element. At the bottom of the file, the CAD geometry representing the charge is written.

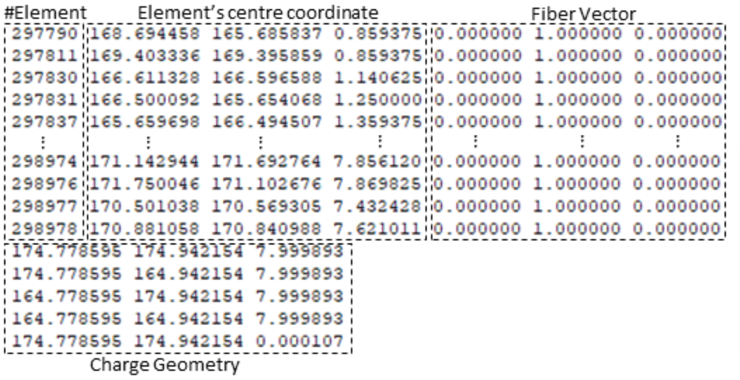

```
297790 168.694458 165.685837 0.859375 0.000000 1.000000 0.000000
297811 169.403336 169.395859 0.859375 0.000000 1.000000 0.000000
297830 166.611328 166.596588 1.140625 0.000000 1.000000 0.000000
297831 166.500092 165.654068 1.250000 0.000000 1.000000 0.000000
297837 165.659698 166.494507 1.359375 0.000000 1.000000 0.000000
  ⋮         ⋮          ⋮          ⋮        ⋮        ⋮        ⋮
298974 171.142944 171.692764 7.856120 0.000000 1.000000 0.000000
298976 171.750046 171.102676 7.869825 0.000000 1.000000 0.000000
298977 170.501038 170.569305 7.432428 0.000000 1.000000 0.000000
298978 170.881058 170.840988 7.621011 0.000000 1.000000 0.000000
174.778595 174.942154 7.999893
174.778595 164.942154 7.999893
164.778595 174.942154 7.999893
164.778595 164.942154 7.999893
174.778595 174.942154 0.000107
```

Figure 5.5. Example of a .cmbc file structure.

A Matlab script was then written to modify the .cmbc file and generate a locally orthotropic and globally random charge structure. The code opens the .cmbc file and imports the mesh elements, the coordinate information and the direction of each fiber vector in the Matlab environment. It is worth to notice that each element belonging to the same mesh layer has a fluctuation of the z coordinate. Since the mesh is of the BLM type, this effect is accentuated in the central portion of the part, where the prismatic elements are lying (Figure 5.6). A nearest-mean partition algorithm is used to stratify the mesh and find the cluster of elements belonging to the same z coordinate (i.e. to the same layer). The thickness of the charge is then modeled as 15 stacked layers of 0.16mm thickness each (Figure 5.6a), which is half the thickness of the prepreg. Two consecutive stacked layers (for example layer i-th and i-th+1) model the thickness of a single prepreg lamina (~0.32mm). The code uses a nested for loop, where it divides the lamina (i.e. two consecutive stacked layer) in the XY plane into grids (or subdomain) of L_chop x L_chop and assigns an orientation vector to the elements within each grid (Figure 5.6b) . The orientation vector V_i randomly generated is assigned to all the elements belonging to a subdomain of the i-th layer that has coordinates of $x_j < X < x_j + L\_chop$ and $y_j < Y < y_j + L\_chop$ (Figure 5.6c). These elements represent only half the thickness of the chop. An orientation vector V_{i+1} perpendicular to the vector V_i is assigned to all the element of the same subdomain but belonging to the i+1 th layer in order to reproduce the orthotropy of the chop (Figure 5.6d).

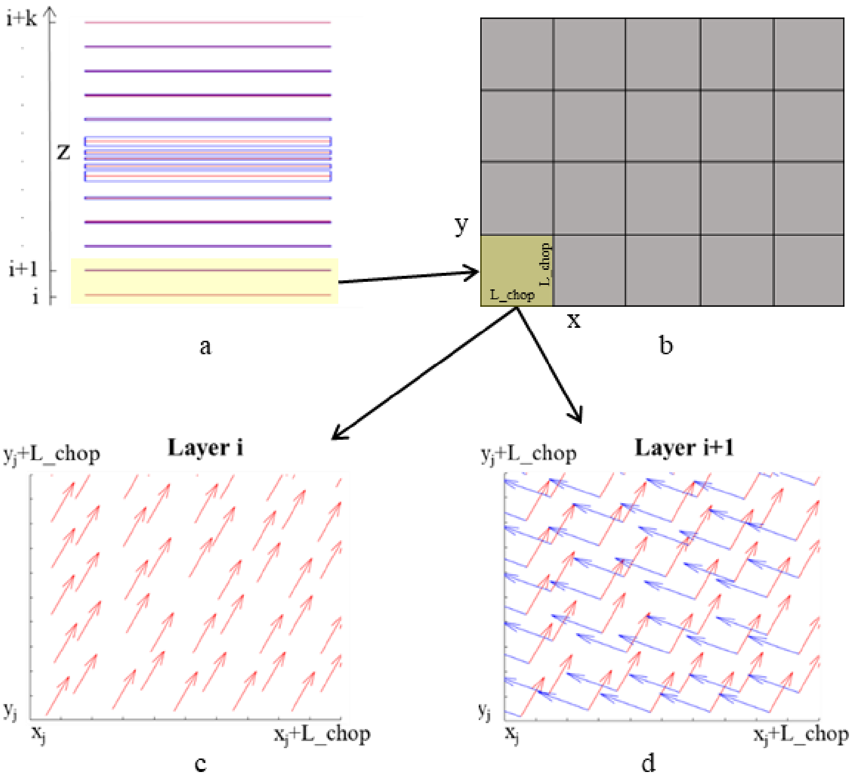

Figure 5.6 Chop generation. a) Clustered layers along the Z direction, the two consecutive elements layer that compose a lamina are evidenced; b) subdomain division of the lamina; c) XY view of the layer i; d) XY view of the layer i+1, where the orthotropic structure is generated.

In our case, the L_chop was set equal to 20mm. This procedure is then iterated with a nested for loop. Indeed, after the first chop generation, the code moves on the next subdomain along the X direction. Accordingly, x_j is set equal to x_j+L_chop, while y_j is kept constant. Consequently, the code generates a first row of chops along the X direction. Once x_j+L_chop is equal to the length of the plate, and thus the last subdomain along the X direction is generated, x_j is set equal to 0. The code moves back on the first column of subdomains, but y_j is set equal to y_j+L_chop and then the iteration along X starts again, to generate the second row of chops. Once the fiber orientation is assigned to all the subdomains of the i-th and i-th+1 layers, the procedure is iterated moving the z over the i+2 th and i+3 th layers in order to generate the second lamina along the thickness direction. A sketch of the charge fiber orientation generation process is shown in Figure 5.7.

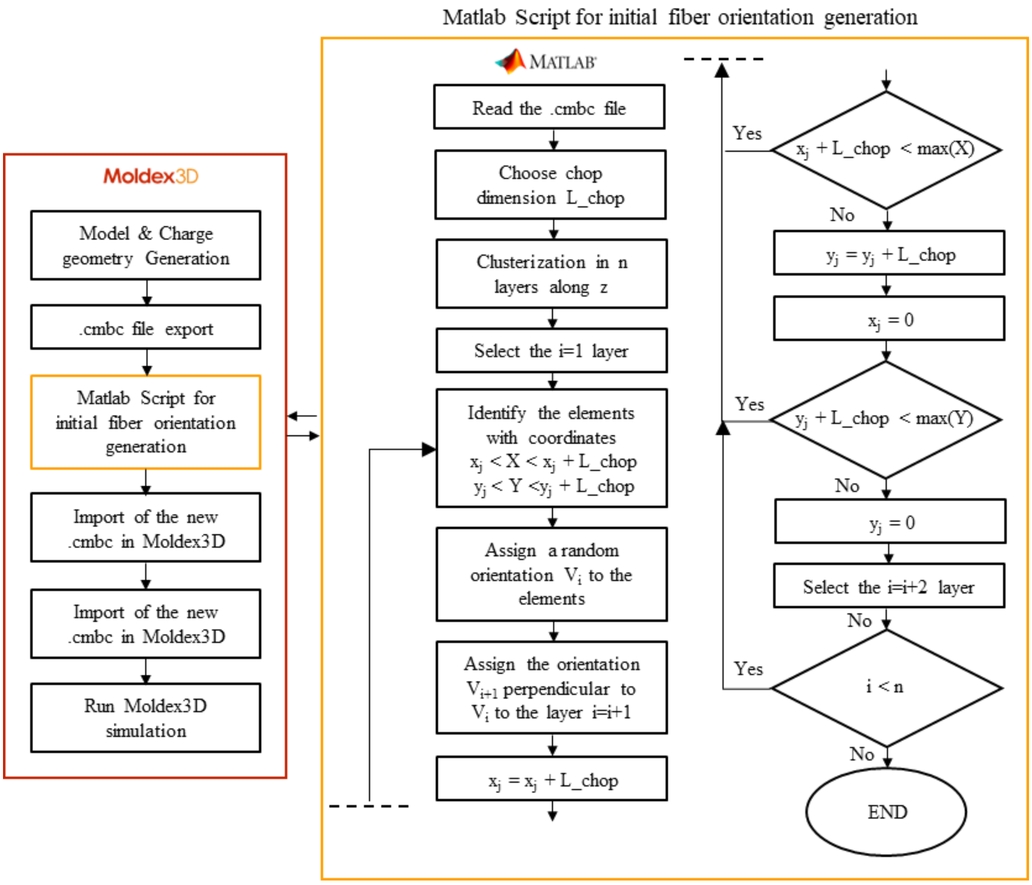

Figure 5.7. Charge discretization and chop generation process flow chart.

The methodology used in the code can be applied to a charge of any geometry. The input parameters of the code are the width, length and thickness of the single chop, the number of layers of the mesh and the previously generated .cmbc file.

The information of the new fiber vectors orientation is then overwritten in the last three column of the .cmbc file, that is then imported in the Moldex3D environment (Figure 5.8). It is important to note that this modeling is an approximation, since in the real case, the chop change orientation across all the charge domains. In the proposed modeling, all the chops are initially parallel each other, but the fiber orientation vector inside them changes randomly, although the orthotropic condition is guaranteed.

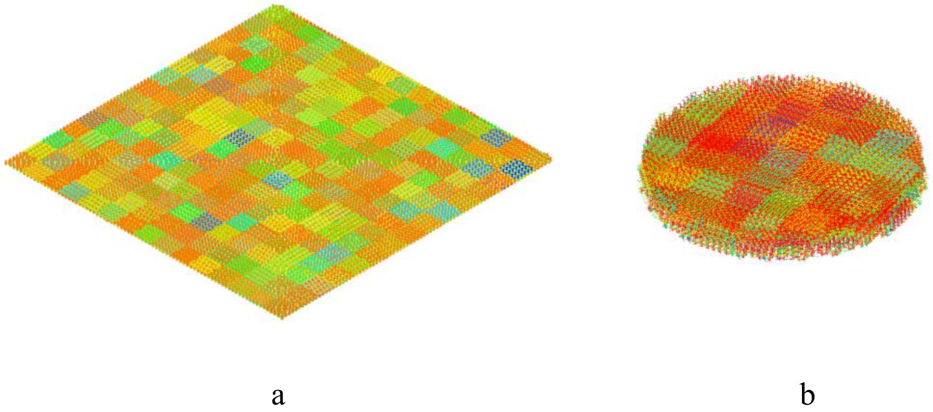

Figure 5.8. Initial fiber orientation within the charge for the configuration a) CP100 and b) CP25.

5.2 Process Simulation results

The process simulation results in terms of fiber orientation for the configurations CP100 and CP25 are shown in Figure 5.9. The color map indicates the A_{xx} component of the second order orientation tensor, which gives an indication of the fibers tendency to be aligned along the global X direction. Considering the configuration CP100, it is appreciable how the fibers present low tendency to rearrange due to the low flow of the melt. The fibers within the chops withstand to small rearrangement and their structure is kept almost undeformed respect to the initial configuration. However, the fibers lying at the interfaces between two contiguous chops tends to rearrange and overlap themselves, generating an orientation distribution like that analyzed in the experimental tests, in correspondence of the CIR. A greater fiber reorientation tendency is appreciable near the mold edges. The Figure 5.9b highlights the changes in fiber orientation in the vicinity of the perimeter of the charge, before (left) and after (right) the compression. Prior to compression, the red chop contains fibers oriented primarily along the X-axis, as indicated by the A_{xx} value being close to 1. After compression, the fibers lose their preferential alignment along the X-axis, instead realigning along the Y-axis. This change in orientation is reflected by the shift in color from red to yellow, which indicates a decrease in the A_{xx} value to around 0.7. The Figure 5.9c shows the results of the compression molding simulation of the CP25 configuration. In this case, the melt front advancement was radial, and the fibers tend to rearrange in the radial direction too. Looking at the central portion of the plate, nearby the initial charge location, the fibers exhibit less tendency to align in the flow direction, and the chops tend to retain their initial structure, as shown in detail in the Figure 5.9d. This figure provides a detailed view of the central part of the plate. On the left side of the figure, there is a detail of a chop before pressing. The chop appears blue, indicating a preferred alignment of fibers along the Y-axis. Despite the strong flow in the X direction in this area, the fibers within this chop do not fully reorient along the X-axis, as can be observed by the color change from blue to light-blue, which suggests final A_{xx} value close to 0.2. As we move away from the location where the charge was initially applied, fibers align with the flow direction and the initial structure of the chopped material is fully lost. The melt-front flows in a radial direction, and once it reaches the boundaries of the mold, it moves in a direction parallel to the mold wall. As a result, the fibers in these areas aligns parallel to the mold edge, as occurred also in the experimental test.

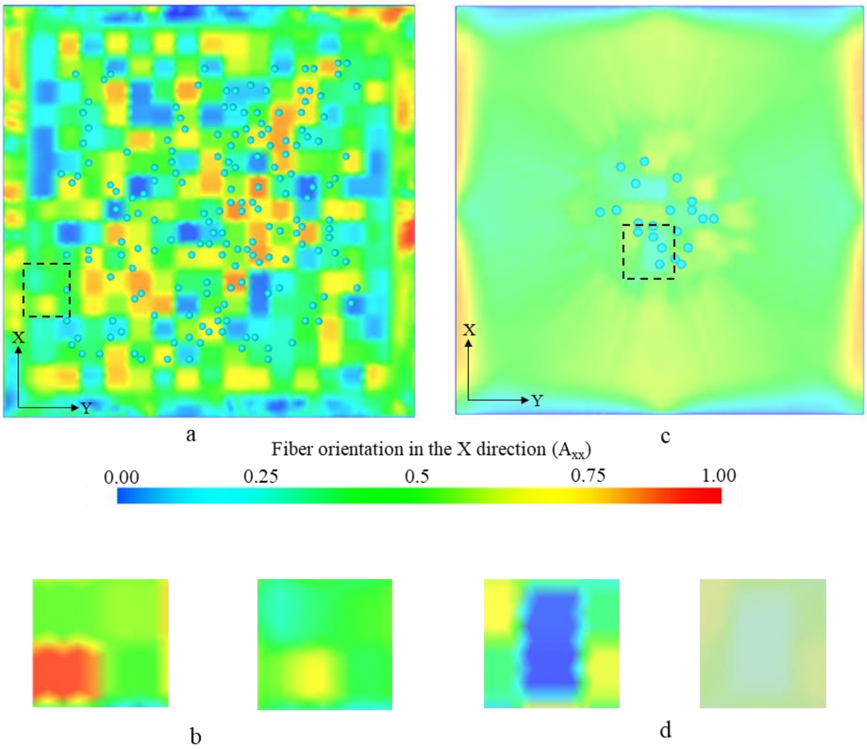

Figure 5.9 Process simulation results: a) CP100 configuration; b) detail of the region evidenced by the black dashed box of the CP100 plate, left image before compression, right image after compression; c) CP25 configuration; d) detail of the region evidenced by the black dashed box of the CP25 configuration, left image before compression, right image after compression. The color bar represents the A_{xx} component of the orientation tensor. The sky-blue circles represents the predicted location of the trapped air.

An interesting result regards the analysis of the voids within the plate. The sky-blue bubble in the Figure 5.9 represents the air trap location. Moldex3D consider the air trap results as the possible locations that void trap could have occurred, as a function of converging melt fronts. It can conclude that an air trap can occur at the location where the melt front comes in all the directions.

The configuration CP100 presents a higher number of potential air trap locations and widely distributed across all the plate surface respect to the CP25 configuration. This result captures well the wide void presence found in the experimental compression molding test due to the melt flow imbalance of the configuration CP100, as widely discussed in the chapter 3.

The Figure 5.10 shows a detail of the part's cross section in correspondence of the edge of the plate. The results are highlighted in terms of fiber orientation. The arrows represent the eigenvectors, and the color of the arrows indicates the eigenvalue associated to that eigenvector. More specifically, the eigenvectors represent the principal direction of the orientation state, while the eigenvalue is a scalar that describes the relative magnitude of the fiber alignment along the corresponding principal direction. In other words, it gives information about how much the fibers are oriented in the direction of the eigenvector.

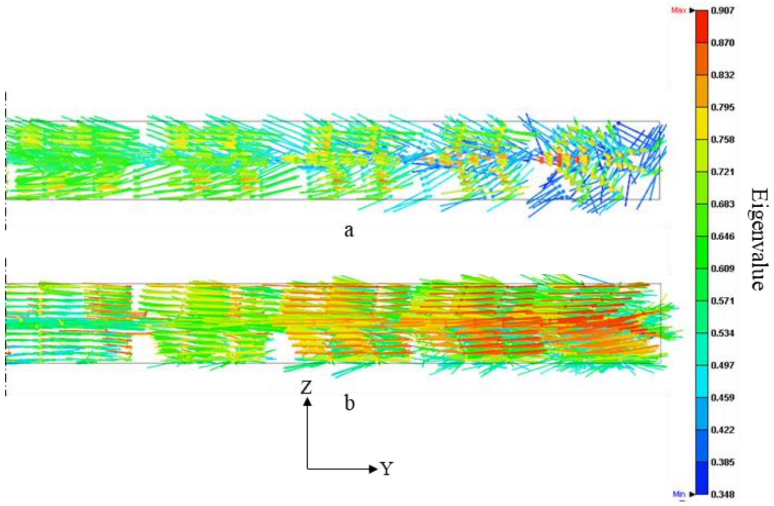

Figure 5.10. Thickness view of the simulation results of the a) CP25 configuration and b) CP100 configuration. The arrow represents the eigenvectors, while the color bar represents the associated first eigenvalue.

Considering the fibers within the CP25 plate (Figure 5.10a), they tends to rearrange also along the z direction and form a swirl path as experimentally evidenced (section 3.1.1). In this region, the air bubbles tend to be transported and then expelled from the mold cavity. Near the edge of the mold, the eigenvalue has a value close to 0.33, meaning that the fibers are randomly oriented. This effect does not occur in the CP100 configuration (Figure 5.10b). Here, the fibers are forming a laminate-like structure and have lower tendency to rearrange along the Z direction, due to the lower flow path that induces less fiber reorientation. This aspect is confirmed by the presence of the red arrows aligned along the Y axis, that presents an eigenvalue close to 1, meaning that the orientation along that eigenvector is strong.

In order to better understand the fiber orientation tendency across the specimen thickness, the Figure 5.11 shows the value of the A_{xx} component of the orientation tensor across the specimen thickness in different locations of the plate.

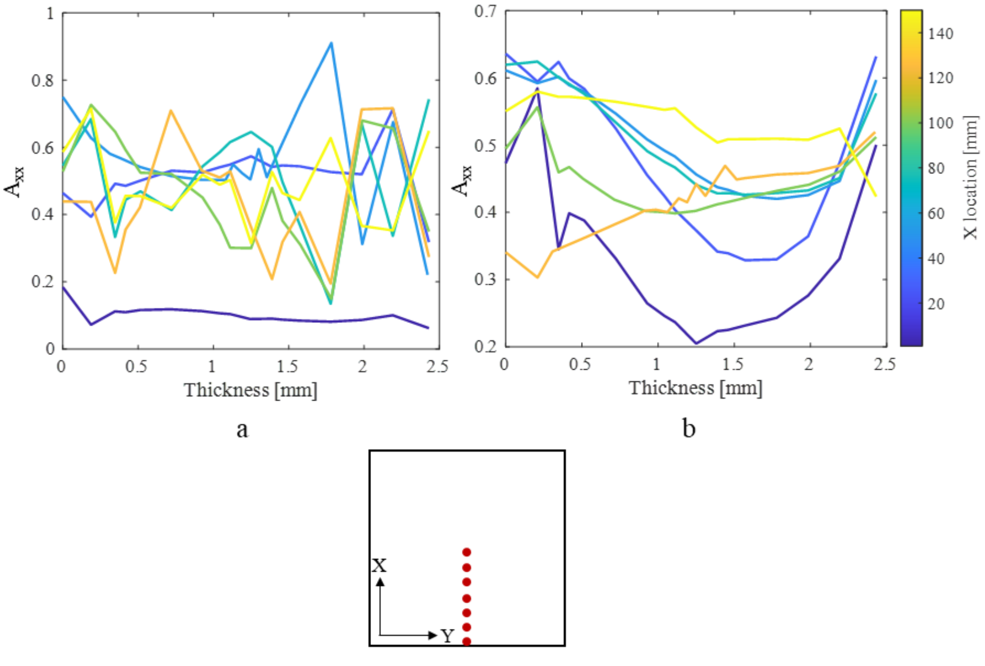

a

b

c

Figure 5.11. A_{xx} trend as a function of the plate thickness: a) CP100 configuration; b) CP25 configuration, c) sampled points location. The color bar indicates the X location of the sampled point.

Seven points have been sampled in the central part of the plate, moving along the X direction, starting from the edge until the central portion of the plate (Figure

5.11c). Considering the configuration CP100, the A_{xx} component has an “up and down” trend as a function of the thickness, especially in samples taken at greater X location (i.e. closer to the center of the plate). This up and down trend means that the chops keep their orthotropic structure (i.e. alternates fiber of 0° and 90° respect to the local chop coordinate system) and has low tendency to a realignment. However, approaching the edge of the plate, the A_{xx} has less variation and tends to stabilize to a value equal to 0, meaning that the fibers tend to rearrange along the Y direction. Considering the CP25 configuration (Figure 5.11b), the fibers are more aligned at lower and higher thickness (i.e. in correspondence of the boundary layers). Indeed, at thickness close to 0 and close to 2.5, the A_{xx} tends to have the same value of around 0.5. Around in the half of the thickness there is a minimum of the A_{xx} and this can be linked to the core layer where the fibers has less tendency be reoriented along the flow direction.

5.3 Structural Analysis

The Digimat software has been used to map the process mesh and generate the material card for the finite element structural simulation. Digimat MF (Mean-Field) was used to carry out the homogenization of the material, starting from the properties of the individual phases (resin and fiber) and obtaining the macroscopic composite properties. The properties of the fiber and the matrix were then entered, and after a series of attempts to calibrate the model as a function of the quasi-static experimental results, a fabric-type microstructure was defined.

Digimat MAP was used to map the fiber orientation in different portions of the process mesh, and to study the influence of local fiber arrangement on mechanical properties. A 250×25mm specimen, modeled with 5mm side square shell elements with 6 integration points along the thickness was used as receiving mesh. A solid to shell element mapping algorithm was used to transfer the fiber orientation distribution from the solid element layers of the process simulation mesh (donor mesh) to the receiving mesh. This algorithm uses an integration point/node to integration point mapping method [114]. The fiber orientation was transferred to each of the 6 thickness integration points of the receiving structural mesh. The integration points of the receiving mesh are localized in the donor mesh and the data are mapped from the donor mesh nodes to the integration points of the receiving mesh. Subsequently the data are interpolated from the integration points to the receiving mesh nodes. Figure 5.12 shows the mapping strategy adopted for both CP100 and CP25 configurations. The MAP_1 specimen was mapped at the centerline of the part, in the area where the fibers did not undergo to large redistribution. The other two specimens were mapped at the edges of the plate, in correspondence of the high flow region, where the fibers have greater tendency to rearrange.

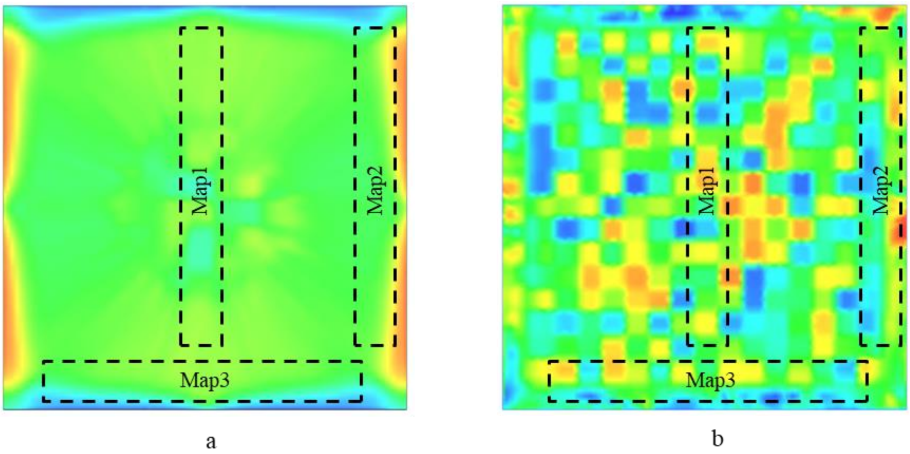

Figure 5.12. Map procedure of the process mesh: a) CP25 configuration; b) CP100 configuration.

Some results of the mapping process are shown in Figure 5.13. Only one specimen per configuration has been reported (MAP1 specimen for CP100 and MAP3 specimen for CP25), and the local orientation of the fibers for each of the 6 integration points is shown in terms of eigenvalues and eigenvectors. Analyzing the Figure 5.13a, it is possible to better appreciate a local redistribution of the fibers also along the thickness. The fibers inside some chops tend to slightly reorient towards the direction of the flow motion (Y axis) generating semi-circular and swirl paths as also observed in the experimental tests. However, no global reorientation of the fibers occurred: the chopped structure still appears intact and the chops are macroscopically randomly oriented. On the other hand, considering the CP25 MAP3 specimen, a preferential fiber direction along the Y direction in all the integration points is noted. This is due to the melt front motion, which deviates when getting in contact with the mold walls. In the central area of the specimen, on the other hand, it can be noted a flow-separation spot, where the fibers tend to remain oriented along the radial flow direction (X) and then deviates in the Y direction as can be appreciated in the first and sixth integration points.

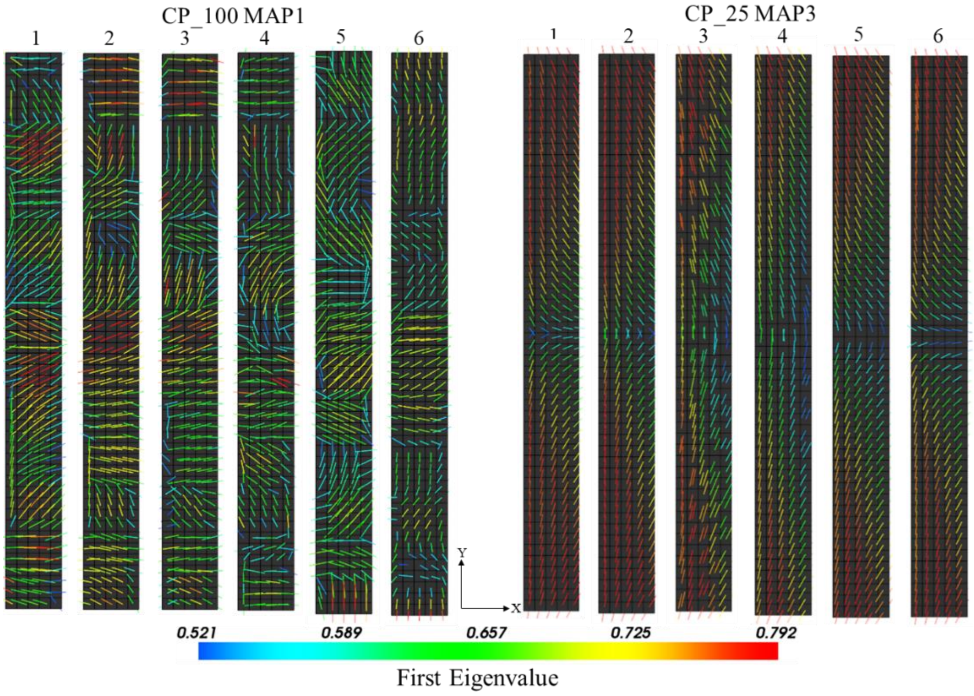

Figure 5.13. Eigenvector distribution across the 6 integration points of the specimens a) CP100 MAP1 and b) CP25 MAP3. The color bar highlights the first eigenvalue.

The structural FE simulation of the tensile test was performed with the LS-Dyna solver (R11.0) in its explicit formulation, using the specimens whose local properties and local fiber orientation were obtained through the mapping process. A linear elastic simulation was run, with a displacement ranging from 0 to 0.2mm and no failure criteria was implemented. Figure 5.14 shows the longitudinal strain and the A_{xx} component map on the first and sixth integration points for the CP100 and CP25 configurations. Only two samples are shown and were chosen to demonstrate the most interesting features of each configuration. For the CP25 configuration, the MAP1 sample was chosen to illustrate how the fibers in the central portion of the plate tend to maintain their initial structure and withstand to an alignment in the flow direction. The CP100 MAP2 specimen, on the other hand, was selected to show the effects of flow-induced phenomenon near the walls of the mold. It is possible to notice different local deformation states for each area of the specimen, as confirmed by the experimental tests. The variation of the deformations across the specimen area indicates a variation of the local elastic properties of the material, due to the different orientation of the fibers in specific sample portion. Minor deformations and therefore greater local stiffness are evident in the regions where the fibers are preferentially oriented along the Y axis (blue areas, Figure

5.14). On the other hand, more pronounced deformations are noticeable in the areas where the fibers are preferentially oriented along the x direction (red areas, i.e greater A_{xx}).

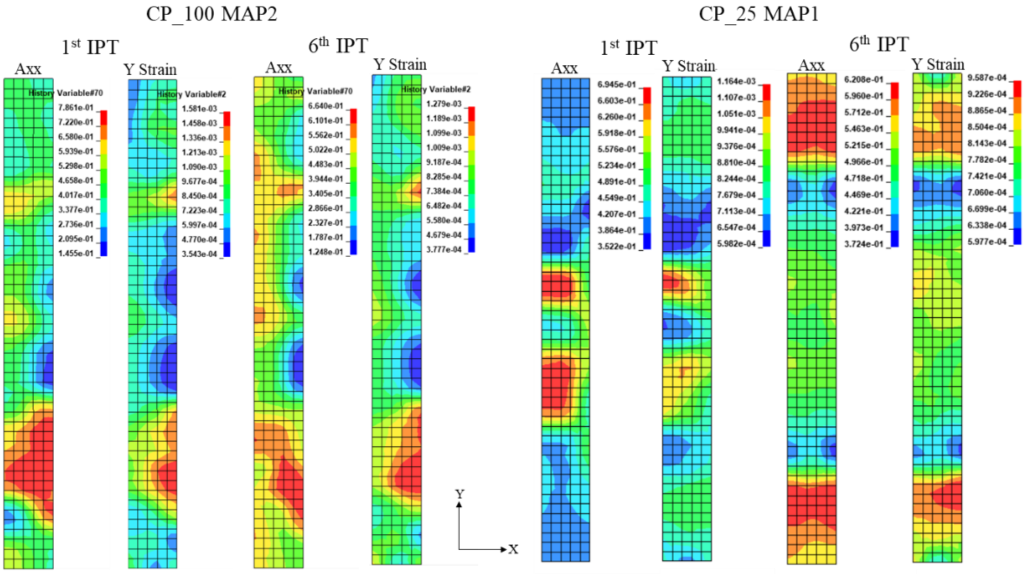

Figure 5.14. Tensile simulation results in terms of A_{xx} and longitudinal strain: a) CP100 MAP2 specimen; b) CP25 MAP1 specimen.

Figure 5.15 shows a comparison between the numerical and experimental results in terms of force-displacement plot. The experimental tests were performed on specimens of the same size as the simulated ones. The graph shows 3 experimental curves, to highlight the results dispersion. Considering the CP100 configuration, the numerical model well captures the experimental trend with an average difference of less than 2%. The 3 specimens CP100 MAP1, MAP2 and MAP3 show lower slopes (and thus lower stiffness) compared to the CP25 configuration. The difference in the average slope between the numerical CP25 and CP100 configuration was around 10% (Table 8). This value is in accordance with the findings in the experimental campaign. Indeed, the experimental tests evidenced a difference in the slope around the 15%. Considering the simulation of the CP25 configuration, the fibers reorientation in the flow direction tends to accentuate the anisotropy of the material. The MAP2 and MAP3 specimens have the greatest stiffness, since in these portions of the plate the fibers align in the specimen longitudinal direction. The MAP1 specimen, on the other hand, has the lowest stiffness, since in the central plate portion the fibers tend to maintain their initial random orientation, due to low flow-induced fiber realignment. This can be appreciated in Figure 5.14: the orientation map of the specimen CP25 MAP1 is like the CP100 MAP2. However, in the case of the CP25 configuration the numerical-experimental correlation gave less accurate results: the average difference between the simulation and the experimentally evaluated slope was around 15%.

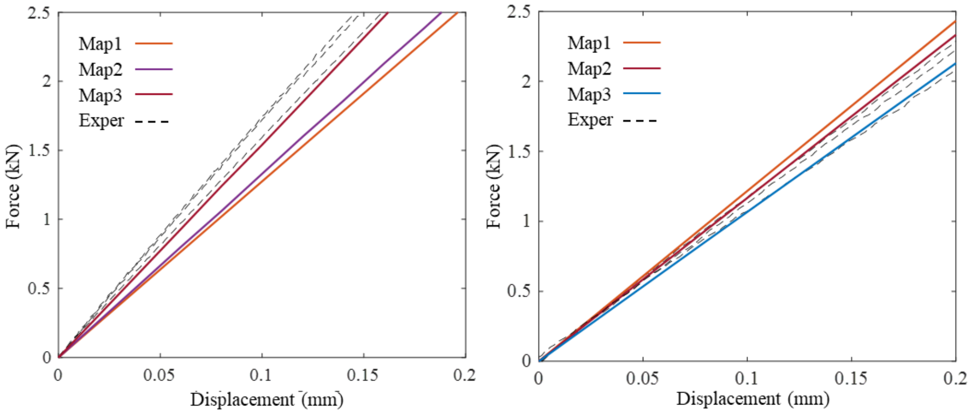

a b

Figure 5.15. Experimental-numerical correlation of the specimen tested in tension: a) CP25 configuration; b) CP100 configuration.

CP25 (kN/mm)		**CP100 (kN/mm)**	
Map1	12.7	Map1	12.1
Map2	13.3	Map2	11.6
Map3	15.4	Map3	10.6

Table 8. Stiffness values of the FEM tensile test simulation

5.4 Conclusion

A methodology for the compression molding simulation of a chopped charge that accounts for the initial fiber orientation state was proposed in this chapter. The Moldex3D flow-based FEM solver was used to simulate the process and a Matlab code was written to set the initial fiber orientation within the charge. Although the model presents some limitations and approximations, it captures the different flow-induced phenomenon according to the initial charge geometry, such as the fiber stratification across the thickness, local fiber orientation and the void presence on the plate surface. The mapping procedure was capable of capture the local fiber orientation, and the adopted strategy allowed for the identification of the local strain variation, with maps similar to the ones obtained through experimental tests. Furthermore, the tensile linear-elastic simulation well captured the local elastic properties variation due to the flow-induced fiber re-orientation. However, the presented methodology has some limitations and approximations. Although the local fiber orientation was initially defined, the charge was considered as a continuum bulk, as it was not possible to discretize each single chop. Consequently, the weld lines that can potentially be generated at the interface between two contiguous chops cannot be accurately predicted. Furthermore, the software considers the fibers as immersed in a continuum resin system. In reality, the material is a fabric prepreg, the fibers are already embedded in the resin that flows together with the chop fibers. Lastly, the fibers are modelled as single long fibers and not as tows. Accordingly, intra-chop interactions, such as crimp and friction are difficult to be predicted. However, the proposed methodology requires a low computational effort to simulate the process. Furthermore, the easy set-up, the flexibility and the scalability make this modelling strategy preferable for industrial applications.

Considering the FEM structural model, an important improvement could involve incorporating failure criteria into the model to predict material strength. As previously discussed, the weak point of the material that has an impact on the overall strength of the structure are the chop interface regions, which consists in rich matrix areas with low FVF. A micro-CT based approach can be used to create an RVE that represents the material microstructure, fiber distribution, and relative FVF. Subsequently, it would be possible to assign the microstructural properties of the different constituents, such as stiffness and strength. The RVE properties could be then homogenized across the entire structure based on the outcomes of the process simulations. This approach could significantly enhance the predictive capabilities of the model, and future development will focus on implementing this methodology.

6 Case Study

The analysis conducted so far in the thesis work, focused on the production of simple flat plates, which do not fully reflect the complexities required for actual components. To address this issue, in this chapter the author proposes a case study, in which a component with complex shape is produced through the technology described in the thesis, to evaluate its potential in producing parts with intricate geometries. The component, shown in Figure 6.1, represents an accelerator pedal lever of a Formula SAE vehicle [115] and it was selected to challenge the forming capability of the chopped material. Indeed, the presence of ribs, sharp corner and narrow section creates restrictions and obstructions to the flow and could lead to mold incomplete filling or the presence of defects.

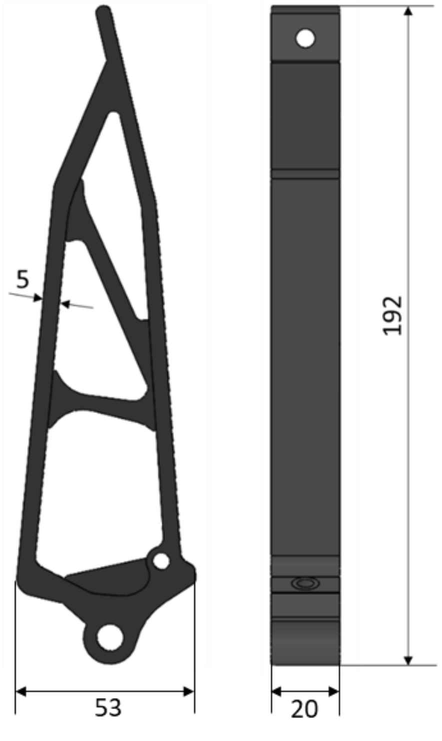

Figure 6.1. Pedal lever geometry. Dimensions are expressed in millimeters.

6.1 Production Process

The accelerator pedal was produced by compression molding of a charge composed of chopped prepreg (chop dimensions 20mm×20mm×0.3mm). The prepreg considered for this study had an areal density of 204gr/m^2. The two steel tools used for the production were custom-designed by the HP Composites company. The female tool (Figure 6.2a) consists of different parts: 3 central islands and two side semi-mold that can be split to remove the component from the mold once the production cycle is completed. The male tool (Figure 6.2b) has 4 semi-cylindrical pins designed for centering the upper with respect to the lower molds. The tool does not have cooling loops and heating resistances, as the heating power is directly transferred and controlled by the molding machine heated plates.

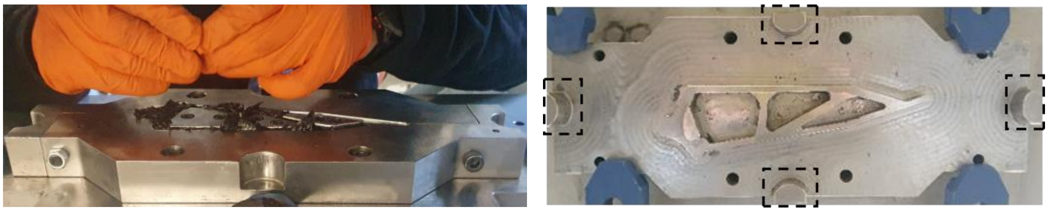
a b

Figure 6.2. Molds for the production of the pedal lever: a) lower (female) tool; b) upper (male) tool. The dashed boxes evidence the centering pins

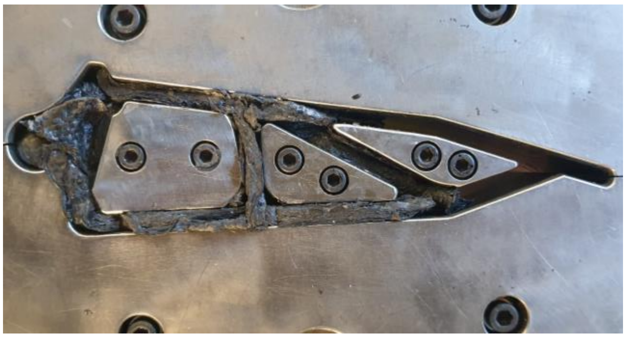

Figure 6.3. Lower tool cavity partially filled. The image refers to the procedure B, where only a portion of the mold surface is filled.

The mold cavity was filled with 80 grams of chopped material. The filling procedure required particular attention as the mold cavity presents narrow sections where it is intricate to dispose the chopped material. Two mold filling procedures were adopted. According to the first methodology (procedure A) the chops were bent and manually forced within the cavity trying to compact them and let the excess air escape. The mold base surface was completely filled, and this methodology recalls the CP100 configuration. Procedure B had a further target: to study the influence of the flow induced phenomena on the component quality, and thus an attempt was made to partially filling the mold cavity. The aim was to initially fill just the 50% of the mold base surface, however the confined space in which to operate made it difficult to insert the 80 grams of chop into just half of the mold cavity. Accordingly, 5 pre-compacted charges were created, by placing 5 chops bunches of 16 gr each under a press and compacting them to a final thickness of 4mm. The pre-compacted charges were then placed within the mold cavities as shown in Figure 6.3. Even with the charge compacted, it was not possible to initially fill only 50% of the mold surface; the minimum initial filling that could be achieved was around 70%.

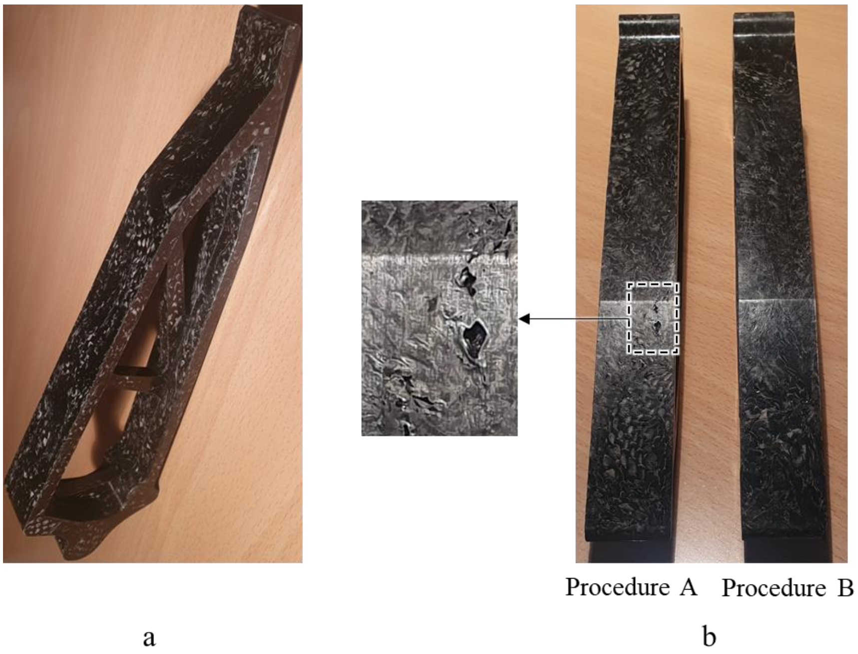

Figure 6.4. Produced accelerator pedals: a) pedal manufactured using the procedure A; b) comparison of the surface finishing of procedure A and B. A detail of the surface blistering is shown.

The component manufactured by means of the procedure A is shown in Figure 6.4a. It is possible to appreciate that the chop tends to retain their initial orthotropic structure, as occurred for the plate produced with the CP100 configuration. Although the presence of ribs and edges makes the component challenging to produce with this technology, the quality of the final product is remarkable. However, the presence of air spots and blistering was evident on the surface of the pedal lever produced with the procedure A (Figure 6.4b). Conversely, the pedal produced with the procedure B had a better finishing, less presence of dry spots and blistering on the surface, and, after a visual inspection, it could be assumed that the fibers tend to be more aligned in the flow direction (as occurred for the plate produced with the CP25 configuration). This result confirmed the findings of the chapter 3, where the high-flow configuration (CP25) guaranteed a better expulsion of the trapped air respect to a low-flow configuration (CP100).

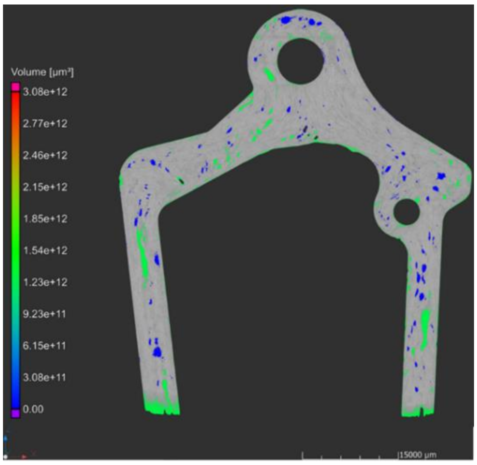

Figure 6.5. Computerized tomography of the pedal produced with the procedure A. The color bar on the left indicates the volume of pores expressed in micrometers.

The Figure 6.5 shows a computer tomography of the pedal produced with the procedure A. Note that, at the time of writing this thesis, the author had not the possibility to execute a micro-CT analysis of the pedal produced with the procedure B. The color bar indicates the void and porous volume. It is possible to notice the high presence of pores within the pedal, and these voids had an average dimension of 4.5 mm^3. By a visual inspection of the image, it can be stated that most of the voids presents a rounded shape, even if some of them are flat and stretched and can reach a length up to 10mm. The computed average porosity across all the component volume is around 7.5%. The peculiar geometry of the pedal with its thick walls makes difficult to expel the air initially trapped between the chops. Indeed, being the thickness higher respect to a flat and large component (such as the plate produced in the chapter 3), there are more chops axially stacked with a higher presence of intra-chop trapped air that is more difficult to expel.

6.2 Mechanical Performance

The accelerator pedal lever was mechanically tested in bending, in order to reproduce the load condition to which it is subjected during its operative cycle (Figure 6.6a).

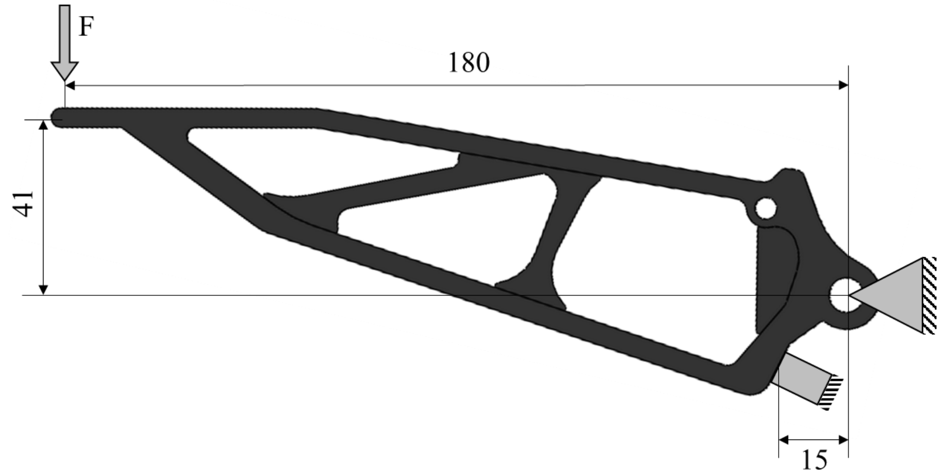

a

b c

Figure 6.6. Testing frame: a) Load and constrain condition (dimensions are expressed in mm); b) test set-up; c) detail of the hinge area; the screw reproduces the end of the pedal stroke.

The test configuration recalls a cantilever beam loaded on its extremity point and it was carried out on a fixture specifically built for this kind of test (Figure 6.6b). Two holes were manually drilled near the anchor area of the pedal before conducting the test. The testing setup includes a pin around which the pedal can freely rotate. This pin is inserted into the larger of the two holes. The downward travel of the pedal is constrained by a stop screw that get in contact with the pedal (Figure 6.6b). This screw reproduces the condition in which the pedal gets in contact with the limit switch of the support on which it is mounted. The load is applied by a loading pin at 180mm respect to the hinged point, simulating the load applied by the driver foot in the direction perpendicular to the lever axis. The load was measured using a 10kN load cell, and the stroke was measured at the point of load application by means of a displacement transducer. All the tests were executed in a quasi-static condition.

The Figure 6.7 proposes the test results in terms of normalized force-displacement trend. Four pedals were tested, and the resulting global stiffness (in the linear part of the characteristic) was rather repeatable in all the tests. The maximum load instead had a scatter with a difference between the minimum and the maximum ultimate load value of the 32% and a normalized standard deviation of 0.1. As found in the standard tests (Chapter 4) the ultimate failure could be instantaneous or can occur after a damage propagation phase. Indeed, the pedal 1 and the pedal 4 had a progressive damage propagation before the ultimate failure, as can be appreciated by the change of the slope after a normalized force value of approximately 0.7. During this phase, several crack and tips occurred that were associable with the crack propagation. These sounds were not appreciable on the samples 2 and 3, where instead the load dropped almost instantaneously without any audible sound that could be associate to a crack propagation phase. A pedal produced with a commercial carbon fiber SMC charge was tested too. Its ultimate failure occurred at a load that was the 35% lower respect to the average maximum load evaluated on the 4 pedals produced with prepreg chops, and the 24% lower respect to the least performant pedal tested with the chopped material. Although this result could be not statistically reliable as only a single test was performed on the SMC pedal, it can give an indication of the good performance of the chopped material respect to the commercially available SMCs.

The Figure 6.8 shows the fracture regions of the 4 tested pedals. Considering the pedal 1 and 2, the failure occurred in correspondence of the drilled hole, in the location A (Figure 6.8). In this area the pedal structure underwent to tensile load, and the failure mainly occurred due to debonding between the chops and delamination. The tested pedal 3 and 4 failed instead in proximity of the hinged hole and in this case the failure occurred mainly due to fiber and chop debonding too. It is worth to notice that the occurrence of the failure in the location A instead that the location B or vice versa could be mainly due to the uncertainness of the drilling operation. The drill in the location A was manually performed by an operator and its position could slightly vary from one pedal to another one.

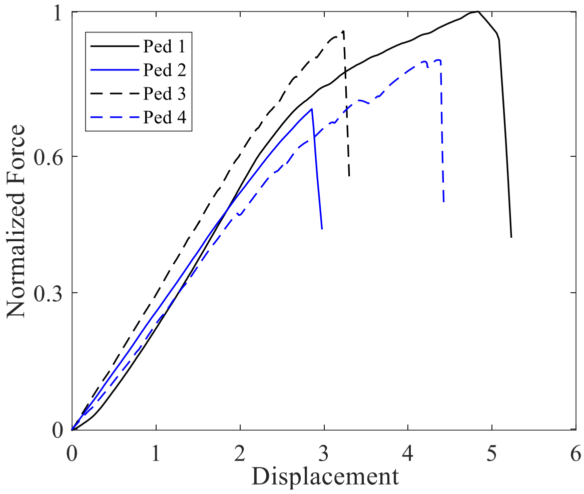

Figure 6.7. Normalized force versus displacement trend of the 4 tested pedals. The force was normalized based on the maximum force value found when testing the pedal 1.

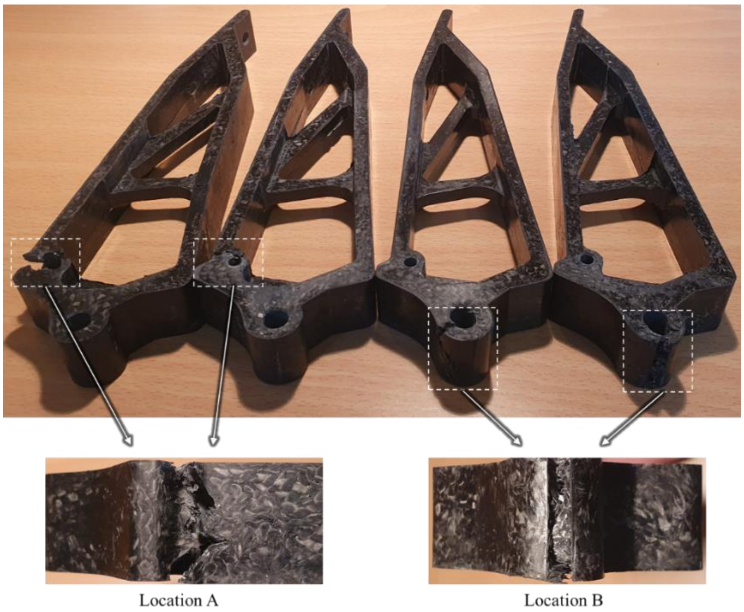

Figure 6.8. Fracture locations with a detail of the fracture surfaces of the tested pedals. From left to right, pedals 1 to 4.

6.3 Process Simulation

The compression molding process for the production of the accelerator pedal was simulated in the Moldex3D environment. The material card, the process and computation parameters used as input were the same descried in the chapter 5. The height of the compression zone was set equal to 35mm according to the mold dimension and was meshed with prism elements (Figure 6.9). The part was instead meshed with a mesh of the BLM type.

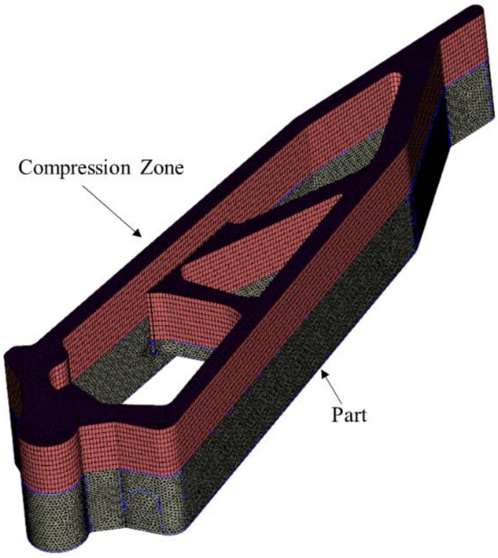

Figure 6.9. Process simulation set-up. Detail of the meshed part and compression zone.

The initial chop distribution within the charge was generated by the MATLAB code, and the chop dimension was set equal to 20mm by 20mm as for the experimental tests. Each chop is supposed to be parallel to the direction of the pedal face where it is lying. This is an approximation, as in the real production process some chops can bend or rearrange during the mold filling process. Accordingly, the script was adapted to a complex geometry such that of the pedal. The pedal geometry was divided into 5 sub-domains in order to capture the flat and straight faces of the pedal. Each sub-domain was re-oriented to have the flat face perpendicular to the global z axis (Figure 6.10). For each sub-domain the chops orientation was generated as described in the chapter 5.

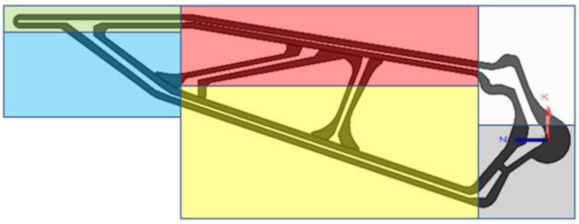

Figure 6.10. Pedal subdomain division

After that, each pedal sub-domain was merged to get the initial pedal structure, and the charge CAD model is ready to be imported in the Moldex3D environment. The Figure 6.11 shows the compression molding simulation results in terms of the fiber orientation. The color bar on the left indicates the first eigenvalue associated to the eigenvectors. In correspondence of the region A the fibers tend to retain their initial orientation as low flow is induced in this part of the pedal. A similar behaviour was found also in the experimental tests, where in correspondence of that flat portion the chops tend to crimp on the mold wall and to retain their original orientation. Considering the region B instead (i.e. the hinge location), the fibers form a swirl path and tend to rearrange in all the 3 directions. The Figure 6.11b shows a detail of the hinge region, and a comparison of the fiber orientation with a computer tomography image. Note that the hole of the scanned component was drilled after the part was extracted from the mold. In correspondence of the region D, G and F, where a section restriction is present, the fibers tend to be highly aligned, as can be also appreciated by the Micro-CT image. There is the presence of two flows that come from the location G and D, and then meet in the E point where a weld line may form. The fiber orientation in this location is well captured by the simulation as can be appreciated by comparing the simulation results with the Micro CT image. Furthermore, in proximity of the C point the fibers rearrange and form a swirl path as they get in contact with the mold walls. However, the hinge location represents the most critical region of the pedal structure, not only because it is potentially the one that support the highest load, but also for the processing condition. Indeed, a point located exactly in the center of this part has the highest distance between the mold walls. Consequently, in this location there is the formation of a bulk of material which tends to slowly warm up, as can be appreciated from the Figure

6.12a. In correspondence of the red bulk (Figure 6.12a), the temperature is around 120 °C, while near the mold walls the temperature reaches a value of 145°C.

The Figure 6.12b shows instead the reactive heat generated by the cross-linking reaction during the curing stage.

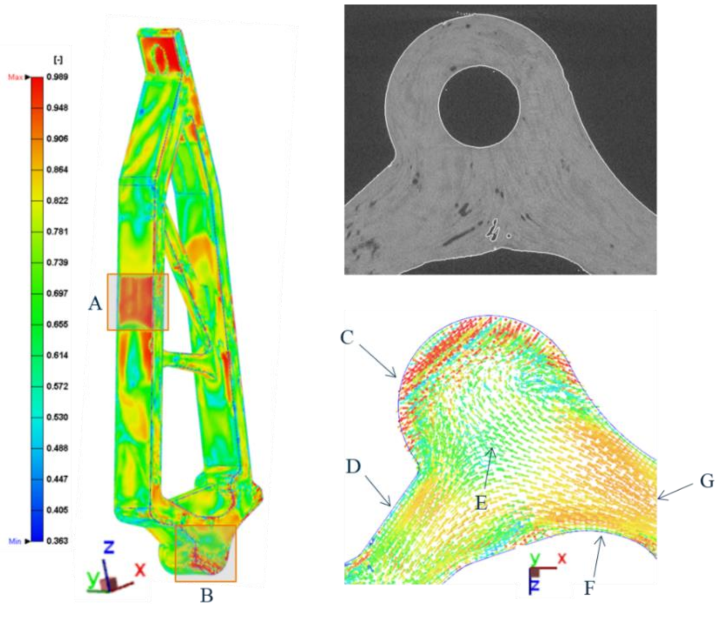

a

b

Figure 6.11. Compression molding simulation of the pedal: a) fiber orientation distribution; the color bar indicates the first eigenvalue; b) detail of the hinge portion of the pedal and comparison with an image obtained with a micro-CT. The letters indicates the interest regions for comparison with the micro-CT image.

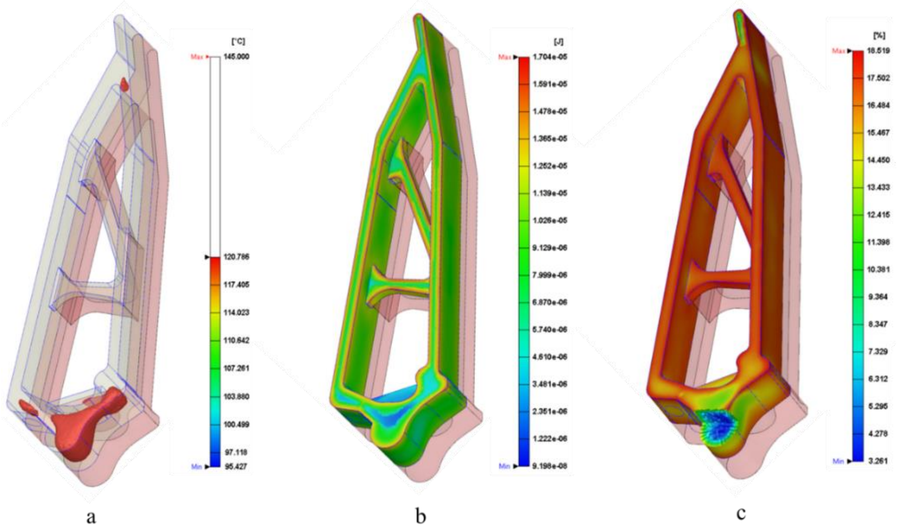

Figure 6.12. Simulation results: a) temperature of the material located in the hinge region; b) reactive heat generation; c) conversion state.

It is possible to notice that the portion of the component in contact with the mold walls (that are at higher temperature) generates more reactive heat due to a faster cross-linking reaction respect to the central portion in correspondence of the hinge region (blue color Figure 6.12b). Indeed, the central portion is exposed to a lower temperature, and thus the cross-linking reaction is slower. This causes a temperature gradient that could lead a different thermal expansion of the central points respect to the ones closest to the mold. Furthermore, the Figure 6.12c shows the resin conversion state after 3 minutes of cycle. The central part of the hinge bulk at this time reached a 3% of conversion, while the material located at the external skin is almost at the 19% of conversion. Accordingly, once the external skin is fully cured and starts to cool down, the resin within the bulk still presents a lower viscosity and it is still generating reactive heat due to the ongoing cross-link reaction. This may induce the air within the bulk to expand, but as the external skin is cured, it remains trapped generating higher porosity and residual stresses.

6.4 Conclusion

The accelerator pedal lever of a formula SAE race vehicle was made using compression molding with chopped charge. Despite the complex shape of the component, including ribs, sharp edges, and thin sections, which can make it difficult to produce using this method, the chopped charge was malleable enough to flow and fill all the spaces and narrow sections without causing any fiber crimps.

The resulting component was of acceptable quality in terms of surface finish and shape accuracy, although there were still some surface imperfections. The mechanical bending tests, developed to simulate the operative loading conditions, demonstrated a scatter of the response (in particular for the maximum sustained load at failure), in line with the findings of the standard experimental tests. Although the high presence of voids evidenced by the CT scan images, the maximum load and the stiffness retrieved from the experimental tests appear to be more than sufficient for the considered application, where the involved maximum loads are moderate and usually do not exceed a level of 1kN. In order to limit the presence of voids, a high melt flow configuration should be reached. It was not possible to experimentally obtain this configuration, as the designed mold present narrow section and low extra-space to fill the necessary material just in one portion of the tool. Accordingly, a specific tool with an external burr chamber could be designed, allowing to dispose the charge material externally from the tool, and let the material flow during the compression molding, letting the fiber to align and the air to be easily expelled. This approach would not only improve the component quality but also increase automation capabilities, which is crucial in industrial settings. This is particularly relevant in situations where mold cavities are narrow and difficult to access, such as in the case of pedals, making manual positioning of chopped fibers challenging. The burr chamber would provide enough maneuvering space, even in the prospect automating the process by using a robot to place the charge within the chamber.

It is important to remark that the proposed element represents the first prototype, and different process and geometric parameters require several optimization cycles that will be deepened by the author in future works. It is necessary to study the correct size of the cutouts, to guarantee a homogeneous filling of the mold, especially in correspondence of the ribs and the sharp edges. The mold temperature during the charge placement must be optimized to ensure that the chops sit well on the mold surfaces. The type of material to be used, the thickness and density must be properly designed according to the component to be produced. Indeed, although it has been shown by standard tests that the prepreg with a surface weight density of 200 gr/m^2 turns out to be more performing, it has a smaller thickness. This implies to manage and handle a greater number of chops, making the mold charging procedure more intricate. The simulation results evidenced a good correlation of the fiber orientation with the experimental tests, especially in the critical regions where the fibers tend to realign. Furthermore, the analysis of the thermal state evidenced that in correspondence of the wider sections where a higher bulk of material is present, the cross-link condition of the resin could be inhomogeneous, and this aspect may eventually generate residual stresses within the component.

Conclusions

This research aimed to explore the potential of utilizing scraps from carbon fiber prepreg, generated during the cutting phase of the production cycle, to create new components. Previous studies have demonstrated, through a life cycle assessment, that incorporating these scraps back into the value chain can significantly reduce the environmental impact and increase the process efficiency. Built on these findings, the current study aimed to move on the implementation of the proposed technology. To do so, it was necessary to:

-Assess the mechanical properties of the material produced from these scraps to determine its potential applications and correlating them with the manufacturing process parameters;

- Study the forming capabilities of the chopped charge and understand how they differ from the conventional molding compounds;

- Investigate and build efficient and flexible methods to predict the structure properties starting from the process conditions.

The innovative aspects of this study rely in the use of bidirectional composite scraps with an orthotropic structure and a thermosetting matrix, a feature that sets it apart from previous researches in this field. These scraps produced during the prepreg cutting stages are utilized as a raw material for the production of new components through the compression molding process. This kind of charge exhibits a high level of heterogeneity due to its composition, consisting of cuts of prepreg fabric known as chops. During pressing, these individual chops interact with each other, resulting in a global rheological response that differs from that of the virgin material. In order to fully understand the behavior of the chopped charge and optimize its use in the production of new components, it was necessary to carefully examine the effects of different processing conditions.

As a first result of the performed testing campaign, it has been pointed out that, during the pressing stages, the individual chops flow and move independently, aligning themselves differently depending on their distance from the mold walls. Near the mold walls, the chops have a greater tendency to reorient due to the friction between the mold and the fibers, while away from the walls, in the core region,, they maintain their initial orthotropic microstructure and moves as a solid unit. It is important to carefully consider the initial mold coverage as it influences the material flow and the resulting microstructure. Two different manufacturing configurations were compared: one with a smaller charge coverage of the mold that induces an higher material flow, and one with a larger coverage with lower induced flow during the pressing stages. Reduced initial coverage of the mold has been shown to induce a greater fiber alignment. However, it was found that this alignment does not result in a statistically significant disparity in the mechanical properties between the longitudinal and transverse direction to the flow. This is in contrast to what has been previously reported in literature, where an anisotropy in properties was observed as a function of the flow direction, especially when molding traditional SMC compounds. Further, it was found that, ensuring full coverage of the mold causes the chops to maintain their initial orthotropic structure. By comparison of plates stamped with a partially covering of the mold, and with fully covering, this latter chop arrangement has been found to result in lower mechanical properties in terms of the final part strength and stiffness. This is due to both fiber alignment and the presence of internal defects, weak spots, and increased porosity. While limiting the flow of material can lead to increased global isotropy, it can also create problems such as internal defects and weak spots. The inhomogeneous and discontinuous nature of the chopped fiber bulk charge can result in difficulties in proper air expulsion, potentially leading to the formation of air pockets within the material and surface blistering if flow is restricted. This differs from traditional molding compounds like SMC, which are pre-compressed and have fewer initial voids and trapped air, resulting in fewer issues with air expulsion during the molding process.

The defects and the trapped air can lead to premature failure of the chopped material. In this kind of structure, it has been observed that the stress tends to concentrate in the regions of stiffness discontinuity such as at the interface regions where the resin accumulates. This aspect differs from other types of materials where stress concentration mainly originates from geometrical details (notches). Since the load is primarily transferred between the chops through shear, the predominant failure modes observed during the coupon testing are chop pull-out and chop debonding. It was considered of interest to investigate the impact of chop size on the material mechanical properties, with the aim of mitigating the material sensitivity toward these failure modes. The experimental test campaign showed that the size of the chops has a significant effect on the mechanical response of the material. It was found that increasing the size of the chops, either in terms of area or aspect ratio, improved the maximum strength of the material, as it facilitated the load transfer between the chops through a larger area. This result is in line with previous studies that have found similar effects in unidirectional fiber systems. However, in contrast to these studies, the current campaign found also an influence of chop size on the stiffness of the material. This discrepancy might derive from the fact that the previous studies considered only unidirectional scraps, while the present work considered orthotropic chops. Despite this, the results highlight the importance of chop size as a key design parameter for improving the mechanical performance of composite materials. However, it should be noted that controlling the size of the scraps may be limited by the need to minimize material waste and the variable size of scraps generated during production of different components.

Although the tests have confirmed a clear influence of the processing conditions and initial structure of the charge on the mechanical performance of the material, the data are affected by a high degree of dispersion and variability, also with regards to the crack nucleation and propagation. This variability, due to the inherent heterogeneity of the structure and complex interactions between the individual chops during crack propagation, is typically greater in comparison to more well-known and homogeneous materials and has been observed in full-scale components as well. Indeed, within the frame of the present research activity, an accelerator pedal was manufactured and tested, exhibiting a failure mode similar to those observed in the standard coupon tensile and bending tests, and primarily characterized by chop debonding.

The challenge in predicting the mechanical behavior of the material lies in the inherent material heterogeneity, that is influenced by the manufacturing conditions. To achieve this target in the prediction, a simulation of the production process, that includes the information of the initial fiber orientation, is crucial to capture the evolution of fiber orientation and the presence of voids within the final formed material. To accomplish this result, an integrated simulation approach involving Matlab, Moldex3D, Digimat, and Ls-Dyna software was originally devised and developed. This integration enables the simulation of both the production process and structural response in a single workflow. This integrated approach allows for the efficient and flexible estimation of structural behavior, starting from the initial charge condition that was defined using a Matlab code. The simulation of the production process provided insights on the evolution of fiber orientation and the presence of voids within the material, and these information were then used in the structural simulation of the specimens. The linear-field structural simulation confirmed the dispersion in the results due to the local elastic properties inhomogeneity the structure. The effectiveness of the proposed integrated simulation has been assessed with the application to the pedal case study and the comparison of the obtained result with the experimental ones.

In conclusion, it can be stated that designing a component using a charge material made from prepreg scraps requires careful considerations, particularly in terms of the production process. Experimental tests and simulations have suggested that ensuring the charge to flow during pressing can improve the material maximum strength and mechanical properties, without affecting the degree of anisotropy. A flow helps to homogenize the structure of the material and reduce the structural discontinuities that could compromise the strength. Furthermore, the material formability is suitable for producing complex components with ribs and sharp edges. However, as the chopped charge requires a more efficient means of removing the trapped air for a successful molding, it is still important to ensure a flow of the charge during the pressing and to design the mold with external chambers to evenly distribute the material and reduce the porosity. It is worth to consider the worst-case scenario when designing a chopped-structure component using prepreg scraps, to ensure its reliability and durability. This is especially due to the significant variability observed in the mechanical test results, which highlighted a variable material response. However, even considering the worst-case mechanical performance, the properties are comparable to those of the most used aluminum alloys (such as 6061). Indeed, just focusing on the automotive field, some components suitable for manufacturing with this technology could be:

- Battery cases
- Aerodynamic devices (rear wing, spoiler, splitter, etc)
- Seat frames
- Bonnet
- Rooftop
- Door’s panel

Other industries suitable for the application of this material could be aerospace (interior components such as seat frames, overhead compartments), sporting goods (rackets, golf clubs, ski), biomedical (prosthesis) or in general applications that require intermediate levels of strength and stiffness, and medium/high production volume rates.

Indeed, the use of compression molding as a production method offers significant benefits, including a streamlined process setup, shortened cycle time, and energy savings in comparison to other composite material production methods. Furthermore, this technology also holds the potential to reduce the environmental impact of the composite industry and provide economic savings, especially when dealing with high-production volumes, through a noble re-utilization of scrap material that would otherwise be discarded and poorly reduced in powder to be used as inert filling. Through this study, a deeper understanding of the material behavior has been acquired, which can aid in the design of more efficient and cost-effective manufacturing processes and components. In conclusion, the results of this work provide a solid foundation for the development of design guidelines for the production of components made of recovered prepreg.

References

[1] Zhang J, Chevali VS, Wang H, Wang CH. Current status of carbon fibre and carbon fibre composites recycling. Compos B Eng 2020;193:108053. https://doi.org/10.1016/j.compositesb.2020.108053.

[2] Giorgini L, Benelli T, Brancolini G, Mazzocchetti L. Recycling of carbon fiber reinforced composite waste to close their life cycle in a cradle-to-cradle approach. Curr Opin Green Sustain Chem 2020;26:100368. https://doi.org/10.1016/j.cogsc.2020.100368.

[3] SUCH M, WARD C, POTTER K. Aligned Discontinuous Fibre Composites: A Short History. Journal of Multifunctional Composites 2014;2:1995–8. https://doi.org/10.12783/issn.2168-4286/2/3/4.

[4] Zhang J, Chevali VS, Wang H, Wang CH. Current status of carbon fibre and carbon fibre composites recycling. Compos B Eng 2020;193:108053. https://doi.org/10.1016/j.compositesb.2020.108053.

[5] Hyde JR, Lester E, Kingman S, Pickering S, Wong KH. Supercritical propanol, a possible route to composite carbon fibre recovery: A viability study. Compos Part A Appl Sci Manuf 2006;37:2171–5. https://doi.org/10.1016/j.compositesa.2005.12.006.

[6] Pimenta S, Pinho ST. Recycling carbon fibre reinforced polymers for structural applications: Technology review and market outlook. Waste Management 2011;31:378–92. https://doi.org/10.1016/j.wasman.2010.09.019.

[7] Nilakantan G, Nutt S. Reuse and upcycling of thermoset prepreg scrap: Case study with out-of-autoclave carbon fiber/epoxy prepreg. J Compos Mater 2018;52:341–60. https://doi.org/10.1177/0021998317707253.

[8] Suzuki T, Takahashi J. Prediction of energy intensity of carbon fiber reinforced plastics for mass-produced passenger cars. Ninth Japan International SAMPE Symposium JISSE-9 2005:14–9.

[9] de Bruijn TA, Vincent G, van Hattum FWJ. Recycling C/PPS laminates into long fibre thermoplastic composites by low shear mixing. ICCM International Conferences on Composite Materials 2017;2017-Augus:20–5.

[10] Kiss P, Stadlbauer W, Burgstaller C, Stadler H, Fehringer S, Haeuserer F, et al. In-house recycling of carbon- and glass fibre-reinforced thermoplastic composite laminate waste into high-performance sheet materials. Compos Part A Appl Sci Manuf 2020;139. https://doi.org/10.1016/j.compositesa.2020.106110.

[11] Wirawan R. Recyclability of Natural Fiber-Filled Thermoplastic Composites. Elsevier Ltd.; 2020. https://doi.org/10.1016/b978-0-12-803581-8.11293-7.

[12] Oliveux G, Dandy LO, Leeke GA. Current status of recycling of fibre reinforced polymers: Review of technologies, reuse and resulting properties. Prog Mater Sci 2015;72:61–99. https://doi.org/10.1016/j.pmatsci.2015.01.004.

[13] Pimenta S, Pinho ST. Recycling carbon fibre reinforced polymers for structural applications: Technology review and market outlook. Waste Management 2011;31:378–92. https://doi.org/10.1016/j.wasman.2010.09.019.

[14] Yang Y, Boom R, Irion B, van Heerden DJ, Kuiper P, de Wit H. Recycling of composite materials. Chemical Engineering and Processing: Process Intensification 2012;51:53–68. https://doi.org/10.1016/j.cep.2011.09.007.

[15] Tapper RJ, Longana ML, Hamerton I, Potter KD. A closed-loop recycling process for discontinuous carbon fibre polyamide 6 composites. Compos B Eng 2019;179:107418. https://doi.org/10.1016/j.compositesb.2019.107418.

[16] Liu B, Zhu P, Xu A, Bao L. Investigation of the recycling of continuous fiber-reinforced thermoplastics. Journal of Thermoplastic Composite Materials 2019;32:342–56. https://doi.org/10.1177/0892705718759388.

[17] Cousins DS, Suzuki Y, Murray RE, Samaniuk JR, Stebner AP. Recycling glass fiber thermoplastic composites from wind turbine blades. J Clean Prod 2019;209:1252–63. https://doi.org/10.1016/j.jclepro.2018.10.286.

[18] Bianchi I, Forcellese A, Marconi M, Simoncini M, Vita A, Castorani V. Environmental impact assessment of zero waste approach for carbon fiber prepreg scraps. Sustainable Materials and Technologies 2021;29:e00308. https://doi.org/10.1016/j.susmat.2021.e00308.

[19] Boursier B, Lopez A. Failure initiation and effect of defects in structural discontinuous fiber composites. International SAMPE Technical Conference 2010.

[20] MALNATI P. Composites-intensive masterwork: 2020 Corvette, Part 2. 27/07/2020 n.d. https://www.compositesworld.com/articles/composites-intensive-masterwork-2020-corvette-part-2 (accessed January 2, 2023).

[21] Clifford J. GR Yaris bodywork: how it is bespoke. Toyota UK Magazine 2020. https://mag.toyota.co.uk/gr-yaris-bodywork-how-it-is-bespoke/ (accessed January 2, 2022).

[22] Feraboli P, Gasco F, Wade B, Maier S, Kwan R, Masini A, et al. Lamborgini “forged composite” technology for the suspension arms of the sesto elemento. 26th Annual Technical Conference of the American Society for Composites 2011: The 2nd Joint US-Canada Conference on Composites 2011;2:1203–15.

[23] Feraboli P. Lamborghini Forged Composite. Technology for the Suspension Arms of the Sesto Elemento 2011:1203–15.

[24] CIRCE - Circular Economy Model for Carbon Fibre Prepregs n.d. https://www.life-circe.eu/ (accessed January 27, 2023).

[25] Such M, Ward C, Potter K. Aligned Discontinuous Fibre Composites: A Short History. Journal of Multifunctional Composites 2014;2:155–68. https://doi.org/10.12783/issn.2168-4286/2/3/4/such.

[26] Selezneva M, Roy S, Lessard L, Yousefpour A. Analytical model for prediction of strength and fracture paths characteristic to randomly oriented strand (ROS) composites. Compos B Eng 2016;96:103–11. https://doi.org/10.1016/j.compositesb.2016.04.017.

[27] Sommer DE, Kravchenko SG, Denos BR, Favaloro AJ, Pipes RB. Integrative analysis for prediction of process-induced, orientation-dependent tensile properties in a stochastic prepreg platelet molded composite. Compos Part A Appl Sci Manuf 2020;130:105759. https://doi.org/10.1016/j.compositesa.2019.105759.

[28] Favaloro AJ, Sommer DE, Denos BR, Pipes RB. Simulation of prepreg platelet compression molding: Method and orientation validation. J Rheol (N Y N Y) 2018;62:1443–55. https://doi.org/10.1122/1.5044533.

[29] Martulli LM, Muyshondt L, Kerschbaum M, Pimenta S, Lomov S v., Swolfs Y. Carbon fibre sheet moulding compounds with high in-mould flow: Linking morphology to tensile and compressive properties. Compos Part A Appl Sci Manuf 2019;126:105600. https://doi.org/10.1016/j.compositesa.2019.105600.

[30] Evans AD, Qian CC, Turner TA, Harper LT, Warrior NA. Flow characteristics of carbon fibre moulding compounds. Compos Part A Appl Sci Manuf 2016;90:1–12. https://doi.org/10.1016/j.compositesa.2016.06.020.

[31] de Souza CSR, Opelt CV, Cândido GM, de Souza SDB, Botelho EC, Fernandes Marlet JM, et al. Reuse of Uncured Carbon Fiber/Epoxy Resin Prepreg Scraps: Mechanical Behavior and Environmental Response. ACS Sustain Chem Eng 2019;7:2200–6. https://doi.org/10.1021/acssuschemeng.8b04852.

[32] Al TB et. Reuse of aeronautical uncured prepreg. Materiales Compuestos 2018:1–5.

[33] de Wayne Howell D, Fukumoto S. Compression molding of long chopped fiber thermoplastic composites. CAMX 2014 - Composites and Advanced Materials Expo: Combined Strength Unsurpassed Innovation 2014.

[34] Jin BC, Li X, Jain A, González C, LLorca J, Nutt S. Optimization of microstructures and mechanical properties of composite oriented strand board from reused prepreg. Compos Struct 2017;174:389–98. https://doi.org/10.1016/j.compstruct.2017.05.002.

[35] Wu MS, Centea T, Nutt SR. Compression molding of reused in-process waste–effects of material and process factors. Advanced Manufacturing: Polymer and Composites Science 2018;4:1–12. https://doi.org/10.1080/20550340.2017.1411873.

[36] LeBlanc D, Landry B, Levy A, Hubert P, Roy S, Yousefpour A, et al. Study of processing conditions on the forming of ribbed features using randomly oriented strands thermoplastic composites. Journal of the American Helicopter Society 2015;60:011005. https://doi.org/10.4050/JAHS.60.011005.

[37] LeBlanc D, Landry B, Levy A. Randomly-Oriented Strands Thermoplastic Composites 2014.

[38] Visweswaraiah SB, Selezneva M, Lessard L, Hubert P. Mechanical characterisation and modelling of randomly oriented strand architecture and their hybrids – A general review. Journal of Reinforced Plastics and Composites 2018;37:548–80. https://doi.org/10.1177/0731684418754360.

[39] van de Velde K, Kiekens P. Thermoplastic polymers: Overview of several properties and their consequences in flax fibre reinforced composites. Polym Test 2001;20:885–93. https://doi.org/10.1016/S0142-9418(01)00017-4.

[40] Muzzy JD, Kays AO. Thermoplastic vs. thermosetting structural composites. Polym Compos 1984;5:169–72. https://doi.org/10.1002/pc.750050302.

[41] Pavlacky D, Vetter C, Gelling VJ. Thermosetting Polymers. Environmental Degradation of Advanced and Traditional Engineering Materials 2013:379–96. https://doi.org/10.1201/b15568-32.

[42] Liang G, Chandrashekhara K. Cure Kinetics and Rheology Characterization of Soy-Based Epoxy Resin System 2006. https://doi.org/10.1002/app.24369.

[43] Kumar S, Prasad NE, Joshi YM. Cross-Linking Reaction under a Stress and Temperature Field : E ff ect on Time-Dependent Rheological Behavior during Thermosetting Polymer Processing 2019. https://doi.org/10.1021/acsapm.9b00432.

[44] Halley PJ, Mackay ME, Halley PJ, Mackay ME. Chemorheology of Thermosets-An Overview a n n.d.;3.

[45] Hsissou R, Hilali M, Dagdag O, Adder F, Elbachiri A, Rafik M. Rheological behavior models of polymers. Biointerface Res Appl Chem 2022;12:1263–72. https://doi.org/10.33263/BRIAC121.12631272.

[46] Wicaksana A. 済無No Title No Title No Title. 2016.

[47] Kotsikos G, Gibson AG. Investigation of the squeeze flow behaviour of Sheet Moulding Compounds (SMC). Compos Part A Appl Sci Manuf 1998;29:1569–77. https://doi.org/10.1016/S1359-835X(98)00094-3.

[48] J. M. Castro, C. W. Macosko. Studies of mold filling and curing in the reaction injection molding process. AIChE Journal 1982;28:250–60.

[49] Tran NT, Gehde M. Creating material data for thermoset injection molding simulation process. Polym Test 2019;73:284–92. https://doi.org/10.1016/j.polymertesting.2018.11.042.

[50] Caron PA, Larreteguy AE, Portaffi PF. Cure kinetics of Butyl rubber cured by Phenol Formaldehyde Resin. Latin American Applied Research 2017;47:59–64. https://doi.org/10.52292/j.laar.2017.302.

[51] Chan TW, Baird DG. An evaluation of a squeeze flow rheometer for the rheological characterization of a filled polymer with a yield stress. Rheol Acta 2002;41:245–56. https://doi.org/10.1007/s00397-001-0214-y.

[52] Rienesl K, Stelzer PS, Major Z. Squeeze flow rheometry and data analysis of carbon fiber sheet molding compounds. Mater Today Proc 2022;62:2433–5. https://doi.org/10.1016/j.matpr.2022.02.583.

[53] Lawal, Adeniyi, and Kalyon DM. Squeezing Flow. Polym Eng Sci 1998;38:1793–804.

[54] Hohberg M. Experimental investigation and process simulation of the compression molding process of Sheet Molding Compound (SMC) with local reinforcements 2018:148.

[55] Pham HT, Meinecke EA. Squeeze film rheology of polymer melts: Determination of the characteristic flow curve. J Appl Polym Sci 1994;53:257–64. https://doi.org/10.1002/app.1994.070530301.

[56] Rienesl K, Stelzer PS, Major Z. Squeeze flow rheometry and data analysis of carbon fiber sheet molding compounds. Mater Today Proc 2022. https://doi.org/10.1016/j.matpr.2022.02.583.

[57] Majhi A, Pardhi TK, Deshpande AP. Analysis of squeeze flow of fluids between solid and porous surfaces. International Journal of Multiphase Flow 2015;68:93–9. https://doi.org/10.1016/j.ijmultiphaseflow.2014.10.007.

[58] R. Byron Bird, Robert C. Armstrong OH. Dynamics of Polymeric Liquids. Polymer Science & Technology General 1987;1.

[59] Salla JM, Cadenato A, Ramis X, Morancho JM. Thermoset Cure Kinetics by Isoconversional Methods. J Therm Anal Calorim 1999;56:771–81. https://doi.org/10.1023/A:1010158223347.

[60] Hohne G.W.H., Hemminger W.F. H-JF. Differential Scanning Calorimetry. Springer 2003.

[61] Murphy KP. Noncovalent forces important to the conformational stability of protein structures. vol. 40. 1995. https://doi.org/10.1385/0-89603-301-5:1.

[62] di Vizio F, Santillo F, Squeo EA, Mirante N, di Cosmo A, Lillo F, et al. Curing kinetics analysis of carbon/epoxy prepreg for solid rocket motor casings application 2015. https://doi.org/10.13009/EUCASS2017-310.

[63] Hagert L. Reverse analysis of the epoxy kinetic model A search for kamal model parameters to fit measured data 2021.

[64] Costa ML, Botelho EC, de Paiva JMF, Rezende MC. Characterization of cure of carbon/epoxy prepreg used in aerospace field. Materials Research 2005;8:317–22. https://doi.org/10.1590/S1516-14392005000300016.

[65] Li Q, Li X, Meng Y. Curing of DGEBA epoxy using a phenol-terminated hyperbranched curing agent: Cure kinetics, gelation, and the TTT cure diagram. Thermochim Acta 2012;549:69–80. https://doi.org/10.1016/j.tca.2012.09.012.

[66] Kenny JM, Trivisano A. Isothermal and dynamic reaction kinetics of high performance epoxy matrices. Polym Eng Sci 1991;31:1426–33. https://doi.org/10.1002/pen.760311909.

[67] Stark W, Jaunich M, McHugh J. Cure state detection for pre-cured carbon-fibre epoxy prepreg (CFC) using Temperature-Modulated Differential Scanning Calorimetry (TMDSC). Polym Test 2013;32:1261–72. https://doi.org/10.1016/j.polymertesting.2013.07.007.

[68] Roşu D, Caşcaval CN, Musta F, Ciobanu C. Cure kinetics of epoxy resins studied by non-isothermal DSC data. Thermochim Acta 2002;383:119–27. https://doi.org/10.1016/S0040-6031(01)00672-4.

[69] Rabearison N, Jochum C, Grandidier JC. A cure kinetics, diffusion controlled and temperature dependent, identification of the Araldite LY556 epoxy. J Mater Sci 2011;46:787–96. https://doi.org/10.1007/s10853-010-4815-7.

[70] Sourour S, Kamal MR. Differential scanning calorimetry of epoxy cure: isothermal cure kinetics. Thermochim Acta 1976;14:41–59. https://doi.org/10.1016/0040-6031(76)80056-1.

[71] Raponi E, Fiumarella D, Boria S, Scattina A, Belingardi G. Methodology for parameter identification on a thermoplastic composite crash absorber by the Sequential Response Surface Method and Efficient Global Optimization. Compos Struct 2021;278:114646. https://doi.org/10.1016/j.compstruct.2021.114646.

[72] Asim M, Jawaid M, Saba N, Ramengmawii, Nasir M, Sultan MTH. Processing of hybrid polymer composites-a review. Elsevier Ltd; 2017. https://doi.org/10.1016/B978-0-08-100789-1.00001-0.

[73] Spasojevic PM. Thermal and rheological properties of unsaturated polyester resins-based composites. Elsevier Inc.; 2019. https://doi.org/10.1016/B978-0-12-816129-6.00015-6.

[74] Park CH, Lee WI. Compression molding in polymer matrix composites. Woodhead Publishing Limited; 2012. https://doi.org/10.1533/9780857096258.1.47.

[75] Trauth A. Characterisation and Modelling of Continuous-Discontinuous Sheet Moulding Compound Composites for Structural Applications. 2018.

[76] Martulli LM, Kerschbaum M, Lomov S v., Swolfs Y. Weld lines in tow-based sheet moulding compounds tensile properties: Morphological

detrimental factors. Compos Part A Appl Sci Manuf 2020;139:106109. https://doi.org/10.1016/j.compositesa.2020.106109.

[77] Sarfraz MS, Hong H, Kim SS. Recent developments in the manufacturing technologies of composite components and their cost-effectiveness in the automotive industry: A review study. Compos Struct 2021;266:113864. https://doi.org/10.1016/j.compstruct.2021.113864.

[78] Lee LJ, Marker LF, Griffith RM. The rheology and mold flow of polyester sheet molding compound. Polym Compos 1981;2:209–18. https://doi.org/10.1002/pc.750020412.

[79] Castro M, Griffith RM. Sheet Molding Compound Compression-Molding Flow* 1989;29:632–8.

[80] Abrams LM. Compound (SMC) Compression Molding . 2003;24.

[81] Lee CC, Tucker CL. Flow and heat transfer in compression mold filling. J Nonnewton Fluid Mech 1987;24:245–64. https://doi.org/10.1016/0377-0257(87)80040-X.

[82] Abdul Rasheed MI. Compression molding of chopped woven thermoplastic composite flakes: a study on processing and performance. 2016.

[83] Lin CM, Weng CI, Ho C ter. Anisotropy in sheet molding compounds during compression molding. Polym Compos 1997;18:613–22. https://doi.org/10.1002/pc.10312.

[84] Feraboli P, Peitso E, Deleo F, Cleveland T, Stickler PB. Characterization of prepreg-based discontinuous carbon fiber/epoxy systems. Journal of Reinforced Plastics and Composites 2009;28:1191–214. https://doi.org/10.1177/0731684408088883.

[85] Starbuck JM, Jacob GC, Simunovic S. Energy absorption in chopped carbon fiber compression molded composites. Proceedings of the 16th ASC Technical Conference 2001:1–13.

[86] Kravchenko SG, Volle C, Kravchenko OG. An experimental investigation on low-velocity impact response and compression after impact of a stochastic, discontinuous prepreg tape composite. Compos Part A Appl Sci

Manuf 2021;149:106524. https://doi.org/10.1016/j.compositesa.2021.106524.

[87] Wan Y, Straumit I, Takahashi J, Lomov S v. Micro-CT analysis of the orientation unevenness in randomly chopped strand composites in relation to the strand length. Compos Struct 2018;206:865–75. https://doi.org/10.1016/j.compstruct.2018.09.002.

[88] Li Y, Pimenta S, Singgih J, Nothdurfter S, Schuffenhauer K. Experimental investigation of randomly-oriented tow-based discontinuous composites and their equivalent laminates. Compos Part A Appl Sci Manuf 2017;102:64–75. https://doi.org/10.1016/j.compositesa.2017.06.031.

[89] Selezneva M, Lessard L. Characterization of mechanical properties of randomly oriented strand thermoplastic composites. J Compos Mater 2016;50:2833–51. https://doi.org/10.1177/0021998315613129.

[90] Kravchenko SG, Sommer DE, Denos BR, Favaloro AJ, Tow CM, Avery WB, et al. Tensile properties of a stochastic prepreg platelet molded composite. Compos Part A Appl Sci Manuf 2019;124:105507. https://doi.org/10.1016/j.compositesa.2019.105507.

[91] Ko S, Yang J, Tuttle ME, Salviato M. Effect of the platelet size on the fracturing behavior and size effect of discontinuous fiber composite structures. Compos Struct 2019;227:111245. https://doi.org/10.1016/j.compstruct.2019.111245.

[92] Ko S, Chan K, Hawkins R, Jayaram R, Lynch C, Mamoune R el, et al. Experimental and numerical characterization of the intra-laminar fracturing behavior in discontinuous fiber composite structures. 33rd Technical Conference of the American Society for Composites 2018 2018;4:2170–83. https://doi.org/10.12783/asc33/26079.

[93] Visweswaraiah SB, Selezneva M, Lessard L, Hubert P. Mechanical characterisation and modelling of randomly oriented strand architecture and their hybrids – A general review. Journal of Reinforced Plastics and Composites 2018;37:548–80. https://doi.org/10.1177/0731684418754360.

[94] Belingardi G, Boria S, Scattina A. Delaminazione Sperimentale E Numerica in Laminati. Sperimentale 2011:7–10.

[95] Davidson BD, Sundararaman V. A single leg bending test for interfacial fracture toughness determination. Int J Fract 1996;78:193–210. https://doi.org/10.1007/BF00034525.

[96] Xu H, Li Y, Brinson C, Chen W. A descriptor-based design methodology for developing heterogeneous microstructural materials system. Journal of Mechanical Design, Transactions of the ASME 2014;136:1–12. https://doi.org/10.1115/1.4026649.

[97] Steven Greene M, Liu Y, Chen W, Liu WK. Computational uncertainty analysis in multiresolution materials via stochastic constitutive theory. Comput Methods Appl Mech Eng 2011;200:309–25. https://doi.org/10.1016/j.cma.2010.08.013.

[98] Harris WM, Chiu WKS. Determining the representative volume element size for three-dimensional microstructural material characterization. Part 1: Predictive models. J Power Sources 2015;282:552–61. https://doi.org/10.1016/j.jpowsour.2015.02.035.

[99] Hill R. Elastic properties of reinforced solids: Some theoretical principles. J Mech Phys Solids 1963;11:357–72. https://doi.org/10.1016/0022-5096(63)90036-X.

[100] Feraboli P, Cleveland T, Stickler P, Halpin J. Stochastic laminate analogy for simulating the variability in modulus of discontinuous composite materials. Compos Part A Appl Sci Manuf 2010;41:557–70. https://doi.org/10.1016/j.compositesa.2010.01.003.

[101] Kravchenko SG, Sommer DE, Denos BR, Avery WB, Pipes RB. Structure-property relationship for a prepreg platelet molded composite with engineered meso-morphology. Compos Struct 2019;210:430–45. https://doi.org/10.1016/j.compstruct.2018.11.058.

[102] Nachtane M, Meraghni F, Chatzigeorgiou G, Harper LT, Pelascini F. Multiscale viscoplastic modeling of recycled glass fiber-reinforced thermoplastic composites: Experimental and numerical investigations. Compos B Eng 2022;242:110087. https://doi.org/10.1016/j.compositesb.2022.110087.

[103] Selezneva M, Roy S, Meldrum S, Lessard L, Yousefpour A. Modelling of mechanical properties of randomly oriented strand thermoplastic composites. J Compos Mater 2017;51:831–45. https://doi.org/10.1177/0021998316654748.

[104] Cutting RA, Favaloro AJ, Goodsell JE. Simulating Prepreg Platelet Molding Compound Flexure Coupons in. 16th International LS-DYNA Users Conference 2020:1–10.

[105] Lim HJ, Choi H, Yun GJ. Multiscale failure and damage analysis of sheet molding compound (SMC) composites using Micro-CT image-based reconstruction model. Compos B Eng 2022;231:109593. https://doi.org/10.1016/j.compositesb.2021.109593.

[106] Li Y, Chen Z, Xu H, Dahl J, Zeng D, Mirdamadi M, et al. Modeling and Simulation of Compression Molding Process for Sheet Molding Compound (SMC) of Chopped Carbon Fiber Composites. SAE International Journal of Materials and Manufacturing 2017;10:130–7. https://doi.org/10.4271/2017-01-0228.

[107] Song Y, Gandhi U, Sekito T, Vaidya U, Hsu J, Yang A, et al. A Novel CAE Method for Compression Molding Simulation of Carbon Fiber-Reinforced Thermoplastic Composite Sheet Materials. Journal of Composites Science 2018;2:33. https://doi.org/10.3390/jcs2020033.

[108] Song Y, Gandhi U, Pérez C, Osswald T, Vallury S, Yang A. Method to account for the fiber orientation of the initial charge on the fiber orientation of finished part in compression molding simulation. Compos Part A Appl Sci Manuf 2017;100:244–54. https://doi.org/10.1016/j.compositesa.2017.05.021.

[109] Moldex3D Manual n.d. http://support.moldex3d.com/r17/en/usermanual.html (accessed December 12, 2022).

[110] Jeffery GB, A PRSL. The motion of ellipsoidal particles immersed in a viscous fluid. Proceedings of the Royal Society of London Series A, Containing Papers of a Mathematical and Physical Character 1922;102:161–79. https://doi.org/10.1098/rspa.1922.0078.

[111] Advani SG, Tucker CL. The Use of Tensors to Describe and Predict Fiber Orientation in Short Fiber Composites. J Rheol (N Y N Y) 1987;31:751–84. https://doi.org/10.1122/1.549945.

[112] Favaloro AJ, Tucker CL. Analysis of anisotropic rotary diffusion models for fiber orientation. Compos Part A Appl Sci Manuf 2019;126. https://doi.org/10.1016/j.compositesa.2019.105605.

[113] Moldex 3D R16 Help n.d. http://support.moldex3d.com/r16/en/standardinjectionmolding_material_materialmodels_pvtmodel.html (accessed January 12, 2023).

[114] Digimat 2021.4 Online Help 2022;Mapping Me.

[115] SAE international's university programs n.d. https://www.sae.org/attend/student-events/.